































CLASSY VIII: Exploring the Source of Ionization with UV ISM diagnostics in local High- z Analogs*

MATILDE MINGOZZI ^{1,2} BETHAN L. JAMES ² DANIELLE A. BERG ³ KARLA Z. ARELLANO-CÓRDOVA ⁴ ADELE PLAT ⁵
CLAUDIA SCARLATA ⁶ ALESSANDRA ALOISI ¹ RICARDO O. AMORÍN ^{7,8} JARLE BRINCHMANN ⁹
STÉPHANE CHARLOT ¹⁰ JOHN CHISHOLM ³ ANNA FELTRE ¹¹ SIMON GAZAGNES ³ MATTHEW HAYES ¹²
TIMOTHY HECKMAN ¹³ SVEA HERNANDEZ ² LISA J. KEWLEY ¹⁴ NIMISHA KUMARI ² CLAUS LEITHERER ¹
CRYSTAL L. MARTIN ¹⁵ MICHAEL MASEDA ¹⁶ THEMIYA NANAYAKKARA ¹⁷ SWARA RAVINDRANATH ¹⁸
JANE R. RIGBY ¹⁸ PETER SENCHYNA ¹⁹ EVAN D. SKILLMAN ⁶ YUMA SUGAHARA ^{20,21,22} STEPHEN M. WILKINS ²³
AIDA WOFFORD ²⁴ AND XINFENG XU ¹³

¹Space Telescope Science Institute, 3700 San Martin Drive, Baltimore, MD 21218, USA

²AURA for ESA, Space Telescope Science Institute, 3700 San Martin Drive, Baltimore, MD 21218, USA

³Department of Astronomy, The University of Texas at Austin, 2515 Speedway, Stop C1400, Austin, TX 78712, USA

⁴Institute for Astronomy, University of Edinburgh, Royal Observatory, Edinburgh, EH9 3HJ, UK

⁵Institute for Physics, Laboratory for Galaxy Evolution, EPFL, Observatoire de Sauverny, Chemin Pegasi 51, 1290 Versoix, Switzerland

⁶Minnesota Institute for Astrophysics, University of Minnesota, 116 Church Street SE, Minneapolis, MN 55455, USA

⁷ARAID Foundation. Centro de Estudios de Física del Cosmos de Aragón (CEFCA), Unidad Asociada al CSIC, Plaza San Juan 1, E-44001 Teruel, Spain

⁸Departamento de Astronomía, Universidad de La Serena, Av. Juan Cisternas 1200 Norte, La Serena 1720236, Chile

⁹Instituto de Astrofísica e Ciências do Espaço, Universidade do Porto, CAUP, Rua das Estrelas, PT4150-762 Porto, Portugal

¹⁰Sorbonne Université, CNRS, UMR7095, Institut d'Astrophysique de Paris, F-75014, Paris, France

¹¹INAF - Osservatorio di Astrofisica e Scienza dello Spazio di Bologna, Via P. Gobetti 93/3, 40129 Bologna, Italy

¹²Stockholm University, Department of Astronomy and Oskar Klein Centre for Cosmoparticle Physics, AlbaNova University Centre, SE-10691, Stockholm, Sweden

¹³Center for Astrophysical Sciences, Department of Physics & Astronomy, Johns Hopkins University, Baltimore, MD 21218, USA

¹⁴Research School of Astronomy and Astrophysics, Australian National University, Cotter Road, Weston Creek, ACT 2611, Australia; ARC Centre of Excellence for All Sky Astrophysics in 3 Dimensions (ASTRO 3D), Canberra, ACT 2611, Australia

¹⁵Department of Physics, University of California, Santa Barbara, Santa Barbara, CA 93106, USA

¹⁶Department of Astronomy, University of Wisconsin-Madison, 475 N Charter Street, Madison, WI 53706 USA

¹⁷Swinburne University of Technology, Melbourne, Victoria, AU

¹⁸Observational Cosmology Lab, Code 665, NASA Goddard Space Flight Center, 8800 Greenbelt Rd, Greenbelt, MD 20771, USA

¹⁹Carnegie Observatories, 813 Santa Barbara Street, Pasadena, CA 91101, USA

²⁰Institute for Cosmic Ray Research, The University of Tokyo, Kashiwa-no-ha, Kashiwa 277-8582, Japan

²¹National Astronomical Observatory of Japan, 2-21-1 Osawa, Mitaka, Tokyo 181-8588, Japan

²²Waseda Research Institute for Science and Engineering, Faculty of Science and Engineering, Waseda University, 3-4-1, Okubo, Shinjuku, Tokyo 169-8555, Japan

²³Astronomy Centre, University of Sussex, Falmer, Brighton BN1 9QH, UK

²⁴Instituto de Astronomía, Universidad Nacional Autónoma de México, Unidad Académica en Ensenada, Km 103 Carr. Tijuana-Ensenada, Ensenada 22860, México

(Accepted for publication in ApJ)

ABSTRACT

In the current JWST era, rest-frame UV spectra play a crucial role in enhancing our understanding of the interstellar medium (ISM) and stellar properties of the first galaxies in the epoch of reionization (EoR, $z > 6$). Here, we compare well-known and reliable optical diagrams sensitive to the main ionization source (i.e., star formation, SF; active galactic nuclei, AGN; shocks) to UV counterparts proposed in the literature - the so-called “UV-BPT diagrams” - using the HST COS Legacy Archive Spectroscopic SurveY (CLASSY), the largest high-

Corresponding author: Matilde MingoZZi
mmingoZZi@stsci.edu

* Based on observations made with the NASA/ESA Hubble Space Telescope, obtained from the Data Archive at the Space Telescope Science Institute, which is operated by the Association of Universities for Research in Astronomy, Inc., under NASA contract NAS 5-26555.

quality, high-resolution and broad-wavelength range atlas of far-UV spectra for 45 local star-forming galaxies. In particular, we explore where CLASSY UV line ratios are located in the different UV diagnostic plots, taking into account state-of-the-art photoionization and shock models and, for the first time, the measured ISM and stellar properties (e.g., gas-phase metallicity, ionization parameter, carbon abundance, stellar age). We find that the combination of C III] $\lambda\lambda 1907,9$ He II $\lambda 1640$ and O III] $\lambda 1666$ can be a powerful tool to separate between SF, shocks and AGN at sub-solar metallicities. We also confirm that alternative diagrams without O III] $\lambda 1666$ still allow us to define a SF-locus with some caveats. Diagrams including C IV $\lambda\lambda 1548,51$ should be taken with caution given the complexity of this doublet profile. Finally, we present a discussion detailing the ISM conditions required to detect UV emission lines, visible only in low gas-phase metallicity ($12+\log(\text{O}/\text{H}) \lesssim 8.3$) and high ionization parameter ($\log(U) \gtrsim -2.5$) environments. Overall, CLASSY and our UV toolkit will be crucial in interpreting the spectra of the earliest galaxies that JWST is currently revealing.

Keywords: Dwarf galaxies (416), Ultraviolet astronomy (1736), Galaxy chemical evolution (580), Galaxy spectroscopy (2171), High-redshift galaxies (734), Emission line galaxies (459)

1. INTRODUCTION

Emission lines provide precious information about the conditions and ionizing sources of the interstellar medium (ISM) in galaxies across cosmic time. Several classification methods have been proposed to identify the main ionization sources: hot and young massive stars, tracing recent star formation (SF); post-asymptotic giant branch (post-AGB) stars, tracing older stellar populations; Active Galactic Nuclei (AGN), and thus the energy of the accretion disc surrounding a central supermassive black hole; low-ionization (nuclear) emission-line regions (LI(N)ERs); shocks, due to supernovae and stellar winds, outflows from starbursts/AGN activity and mergers, or from random motions of interstellar clouds; accretion on compact objects (e.g., High-Mass X-ray Binaries, HMXB); or a mixture of them (e.g., Heckman 1980; Izotov & Thuan 1999; Nagao et al. 2006; Kewley et al. 2006; Allen et al. 2008; Stasińska et al. 2015; Belfiore et al. 2016).

Historically, the main diagnostics to discriminate between different ISM ionization mechanisms are the classical optical diagnostic diagrams, first presented in Baldwin et al. (1981) (and usually referred as BPT diagrams) and then progressively updated by Keel (1983); Veilleux & Osterbrock (1987); Kauffmann et al. (2003); Kewley et al. (2006). These diagrams are constructed on intensity ratios of strong emission lines close in wavelength, namely [N II] $\lambda 6584/\text{H}\alpha$, [S II] $\lambda\lambda 6717,31/\text{H}\alpha$ and [O I] $\lambda 6300/\text{H}\alpha$ versus [O III] $\lambda 5007/\text{H}\beta$ (i.e., [N II], [S II] and [O I] BPT diagrams), minimizing the effects of differential reddening by dust and flux calibration issues. They have been found useful to discriminate between H II-like sources and objects photoionised by a harder radiation field (e.g., power-law continuum by an AGN or shock excitation). However, existing BPT diagrams can be less effective in discriminating mechanisms other than SF in metal-poor galaxies (e.g., Groves et al. 2006; Reines et al. 2020; Polimera et al. 2022), since,

on the one hand, the involved line ratios can be dependent on metallicity and, on the other, the hot metal-poor stellar populations have a hard spectrum to irradiate the gas (e.g., Feltre et al. 2016; Byler et al. 2018; Xiao et al. 2018; Wofford et al. 2021). Also, these diagnostics are not optimal in discriminating shocks from other ionization sources.

Exploiting the large statistics of the SDSS DR7 (Abazajian et al. 2009), Shirazi & Brinchmann (2012) proposed a less metallicity-dependent diagnostic diagram to discriminate the ionization source: [N II]/ $\text{H}\alpha$ versus He II $\lambda 4686/\text{H}\beta$. He II $\lambda 4686$ is produced via recombination and thus indicates the existence of sources of hard ionizing radiation capable of ionizing the helium (ionization potential of 54.4 eV). Such a high radiation field can be produced by young stellar populations (massive and very massive stars), including O-type stars (e.g., Sixtos et al. 2023) and some types of Wolf-Rayet (WR) stars (e.g., WC, WO, and WNE, Schaerer & Vacca 1998; see also Schmutz et al. 1992), but also other mechanisms such as AGN (Shirazi & Brinchmann 2012), X-ray binaries (Garnett et al. 1991; Mayya et al. 2023) or shocks (Thuan & Izotov 2005; Dopita & Sutherland 1996; Stasińska et al. 2015; Alarie & Morisset 2019) can play a role. Recently, Tozzi et al. 2023 investigated the Shirazi & Brinchmann (2012) diagnostic diagram with integral field spectroscopy (IFS) observations from the SDSS-IV MaNGA (Mapping Nearby Galaxies at APO; Bundy et al. 2015) survey, confirming its power in revealing AGN activity undetected from the classical BPT diagrams. Finally, to better disentangle the presence of shocks, Kewley et al. (2019) presented an overview of alternative optical diagrams, including [O III] $\lambda 5007$, [O II] $\lambda 3727$ and [O I] $\lambda 6300$ emission lines (see also Heckman 1980; Allen et al. 2008) as well as the importance of correlations between line ratios and the velocity dispersion of the gas. Overall, the combination of (some of) these optical criteria provides a reliable powerful tool to investigate the ISM ionization sources in galaxies.

However, the well-studied optical emission lines (from [O II] $\lambda\lambda 3727$ to [S III] $\lambda\lambda 9069, 9532$) on which the diagnostics described in the previous paragraphs rely are not easily accessible to investigate the early phases of galaxy evolution in the epoch of reionization (EoR, $z > 6$) in the current JWST and future extremely large ground-based telescopes (ELTs) era. For example, JWST/NIRSpec does not cover anymore H α at $z \gtrsim 6.5$ and [O III] $\lambda\lambda 4959, 5007$ at $z \gtrsim 10$, while JWST/MIRI is less sensitive and does not have multi-object slit capabilities. Hence, rest-frame UV emission lines have started to play a critical role in understanding EoR objects, thus making a reliable UV toolkit of ISM diagnostics essential. EoR galaxies are expected to be increasingly compact, metal-poor, with low-masses and large specific star formation rates (e.g., Wise et al. 2014; Madau & Haardt 2015; Robertson et al. 2015; Stanway et al. 2016; Stark 2016) and characterized by prominent high-ionization nebular UV emission lines (e.g., He II $\lambda 1640$, O III] $\lambda\lambda 1661, 6$, C III] $\lambda\lambda 1907, 9$, C IV] $\lambda\lambda 1548, 51$; Stark et al. 2015; Mainali et al. 2017; 2018). The spectra of some of these objects have already started to be revealed with JWST/NIRSpec (e.g., Curti et al. 2022; Arellano-Córdova et al. 2022a; Curtis-Lake et al. 2023; Matthee et al. 2022; Trump et al. 2023; Arrabal Haro et al. 2023), with one of the furthest ($z \sim 10.603$) galaxies ever spectroscopically observed characterized by plenty of UV (from Ly α to Mg II] $\lambda\lambda 2795, 2802$) and optical (from [O II] $\lambda\lambda 3727$ to [O III] $\lambda\lambda 4363$) emission lines (Bunker et al. 2023a). In the foreseeable future, further JWST observations including large surveys such as GLASS (e.g., Treu et al. 2022; Roberts-Borsani et al. 2022; Castellano et al. 2022), CEERS (e.g., Finkelstein et al. 2022; Arrabal Haro et al. 2023) and JADES (e.g., Curtis-Lake et al. 2023; Bunker et al. 2023a) will provide more and more rest-frame UV spectra of $z > 6$ systems, exploring in depth the EoR.

Several recent works proposed UV alternatives to the optical diagnostics, either using photoionization models from SF and AGN (Feltre et al. 2016; Jaskot & Ravindranath 2016; Nakajima et al. 2018; Dors et al. 2018; Byler et al. 2020) and shock models (Jaskot & Ravindranath 2016), or from the comparison of either models and simulations (Hirschmann et al. 2019; 2022). For instance, F16 proposed various UV diagnostic plots, including the C III] $\lambda\lambda 1907, 9$ /He II] $\lambda 1640$ versus C IV] $\lambda\lambda 1548, 51$ /He II] $\lambda 1640$ to discriminate between SF and AGN models (see also Dors et al. 2018). Jaskot & Ravindranath (2016) used the same diagnostic diagram to separate SF from shocks models, while Nakajima et al. (2018) proposed alternative models and diagrams based on C IV] $\lambda\lambda 1548, 51$ /C III] $\lambda\lambda 1907, 9$ and their equivalent widths (EWs). Finally, Hirschmann et al. (2019; 2022) coupled models and cosmological zoom-in simulations, exploring synthetic optical and UV emission-line diagnostic diagrams, listing the most promising in Table 1 of Hirschmann et al.

(2022). However, UV diagnostics have yet to be compared against the optical ones in a systematic way, because it is not trivial to observe a full suite of optical and UV lines capable of probing the different ISM properties (e.g., density, temperature, metallicity, ionization parameter), which is fundamental for interpreting the results.

The analysis of local galaxies can provide the tools to interpret high- z galaxies, given the high signal-to-noise (S/N) of their spectra and the possibility of getting multi-wavelength coverage, which can help in the data interpretation. In Mingozi et al. (2022) (Paper IV hereafter) we have started to create such a UV toolkit using the Cosmic Origins Spectrograph (COS) Legacy Spectroscopic Survey (CLASSY¹; Berg et al. 2022; James et al. 2022, Paper I and Paper II hereafter). CLASSY represents the first high-quality, high-resolution far-UV (FUV, 1150–2000 Å) Treasury of 45 nearby ($0.002 < z < 0.182$) star-forming galaxies, with properties that make them representative at all redshifts (see Paper I Fig. 8), but generally characterized by more extreme ionization fields, lower stellar masses, and higher star formation rates (SFRs) than $z \sim 0$ objects, as typically observed in the EoR (e.g., Wise et al. 2014; Madau & Haardt 2015; Robertson et al. 2015; Stanway et al. 2016; Stark 2016). Specifically, in Paper IV we provided detailed measurements of dust attenuation ($E(B - V)$), electron density (n_e), electron temperature (T_e), gas-phase metallicity ($12 + \log(O/H)$) and ionization parameter ($\log(U)$), using both UV and optical direct diagnostics, taking into account the different ionization zones of the ISM. Then, from the comparison of the derived properties, we provided a set of equations to estimate ISM properties only from UV emission lines. This paper presents the second part of the UV-based toolkit introduced in Paper IV and aims at exploring the well-known optical emission-line diagnostics tracing the different ionization sources and the recently proposed UV-based counterparts, to check their consistency and reliability to discriminate SF from AGN and shock ionization.

In Sec. 2 we describe the CLASSY sample, summarizing the characteristics of the UV and optical data, the main steps of the data analysis performed in Paper IV, while in Sec. 3, we give an overview of the models used in this work to interpret the optical and UV diagnostics. In Sec. 4 we present the main optical diagnostic diagrams sensitive to the ionization source to demonstrate that CLASSY galaxies are indeed dominated by SF. CLASSY represents the local reference sample of metal-poor star-forming galaxies that we can use to explore the boundaries of the star formation locus in UV diagnostic diagrams, as we show in Sec. 5, interpreting the results taking into account ISM properties and

¹ <https://archive.stsci.edu/hlsp/classy>

state-of-the-art photoionization and shock models. Then, in Sec. 6 we discuss the conditions needed to observe UV emission lines, possible caveats in using them as diagnostics and which of them are currently observed with JWST at high- z . Finally, in Sec. 7 we summarize our main findings. Throughout this work we assume a flat Λ CDM cosmology ($H_0 = 70$ km/s/Mpc, $\Omega = 0.3$) and $12+\log(\text{O}/\text{H})_{\odot} = 8.69$ (Asplund et al. 2009).

2. THE CLASSY SURVEY

The 45 local galaxies from the CLASSY survey span a wide range of stellar masses ($6.2 < \log(M_*/M_{\odot}) < 10.1$), SFRs ($-2 < \log(\text{SFR}/M_{\odot}\text{yr}^{-1}) < +1.6$), oxygen abundances ($7 < 12+\log(\text{O}/\text{H}) < 8.8$), electron densities ($10 < n_e([\text{S II}]\lambda\lambda 6717,31)/\text{cm}^{-3} < 1120$), degree of ionization ($0.54 < O3O2 < 38.0$, with $O3O2 = [\text{O III}]\lambda\lambda 5007/[\text{O II}]\lambda\lambda 3727,9$), and reddening values ($0.02 < E(B-V) < 0.67$). In Paper I, we present our sample, explaining in detail the selection criteria along with an extensive overview of the HST/COS and archival optical spectra. Also, Paper I broadly compares the global properties of the CLASSY galaxies with local and high- z samples (see Paper I Sec. 5, Fig. 8), showing that these objects are characterized by similar low masses and metallicity to the dwarf galaxies of the local volume, but are characterized by higher SFRs and sSFRs, consistent with high- z systems. Also, CLASSY objects follow the same trend as other $z \sim 0$ star-forming galaxies in the mass-metallicity relation but with a larger scatter. Recent JWST studies are further confirming that such characteristics are typical of the high- z Universe (see e.g., Fig 4 and 5 of Curti et al. 2023; Atek et al. 2023; Simmonds et al. 2023). The data reduction is presented in Paper II, including spectra extraction, co-addition, wavelength calibration, and vignetting. In Paper IV, we explained in detail the data analysis, from the stellar continuum modeling to the emission line fitting, providing measurements for the UV redshifts (z_{UV}), the main UV and optical emission line fluxes and equivalent widths, and ISM properties. In the following subsections, we summarize the most important characteristics of the sample and the main steps of the data analysis performed in these previous works.

2.1. The sample

CLASSY spectra span from 1150 Å to 2100–2500 Å, combining the G130M, G160M, G185M, G225M and G140L HST/COS gratings, from 135 orbits of new COS data (PID: 15840, PI: Berg) and 177 orbits of archival COS data, for a total of 312 orbits. Both this paper and Paper IV focus on the analysis of all the emission lines (except for Ly α) in the range 1150–2000 Å, using the so-called *High Resolution* (HR: G130M+G160M; $R \sim 10000 - 24000$) and *Moderate Resolution* (MR: G130M+G160M+G185M/G225M;

$R \sim 10000 - 20000$) co-added spectra², presented in detail in Berg et al. (2022)³. We collected data for the entire CLASSY sample also in the optical wavelength regime, gathering SDSS spectra if available, integral field spectroscopy data (VLT/VIMOS, MUSE, Keck/KCWI), or long-slit spectra (MMT; LBT/MODS, see Arellano-Córdova et al. 2022b, CLASSY Paper V). A full description of the CLASSY optical dataset can be found in Paper IV⁴.

In Paper IV and throughout this work, we take into account the properties of the CLASSY galaxies in terms of redshift, stellar mass M_* , SFR, and $12+\log(\text{O}/\text{H})$, estimated and described in Paper I (see Sec. 4.5 and 4.7). Specifically, $12+\log(\text{O}/\text{H})$ measurements are based on the direct T_e method, using $[\text{S II}]\lambda 6717/\lambda 6731$ and $[\text{O III}]\lambda 4363/\lambda 5007$ as electron density and temperature tracers, respectively. We also take into account the ionization parameter $\log(U)$ from $[\text{O III}]\lambda 5007/[\text{O II}]\lambda\lambda 3727$ and the stellar age of our targets, determined from the analysis presented in Paper IV. For this paper, we also measured the carbon-to-oxygen abundance C/O, which we calculated following the prescriptions of Berg et al. (2016). Specifically, we calculated the ionic abundances of C⁺⁺ and O⁺⁺ from C III] $\lambda 1907,9/H\beta$ and [O III] $\lambda 1666/H\beta$ using PyNeb (Luridiana et al. 2015) and $T_e([\text{O III}])$. Then, we divided one by the other multiplying per the ionization correction factor (ICF), provided by Berg et al. (2016), taking into account $\log(U)$. We find $(\text{C}/\text{O})/(\text{C}/\text{O})_{\odot}$ to vary in the range 0.1–0.6, with $(\text{C}/\text{O})_{\odot} = 0.44$. A detailed discussion about CLASSY C/O will be given by Berg et al. (in preparation).

2.2. Data analysis

Here, we briefly summarize the main steps of the data analysis of UV and optical spectra performed in Paper IV (see their Sec. 3). In particular, we used a set of customized Python scripts in order to first fit and subtract the stellar component and then fit the main emission lines with multiple Gaussian components where needed.

As a preliminary step, both UV and optical CLASSY spectra were corrected for the total Galactic foreground reddening along the line of sight of their coordinates with the Cardelli et al. (1989) reddening law (see Paper I). Then, we fitted and subtracted the UV and optical stellar components, adopting the latest version of the Bruzual & Charlot (2003) models, assuming the Chabrier (2003) initial mass function (IMF), as

² The instrumental broadening at the wavelengths of the emission lines taken into account in the HR and MR spectra is, respectively, $\sigma_{\text{int}} \sim 15 - 30$ km/s.

³ Only for J1044+0353 and J1418+2102, we used the so-called *Low Resolution* (LR: G130M+G160M+G140L or G130M+G160M+G140L; $R \sim 1500 - 4000$, $\sigma_{\text{int}} \sim 80$ km/s) coadds because of the lack of higher resolution data.

⁴ The instrumental broadening of the optical data is in the range $\sigma_{\text{int}} \sim 35 - 120$ km/s.

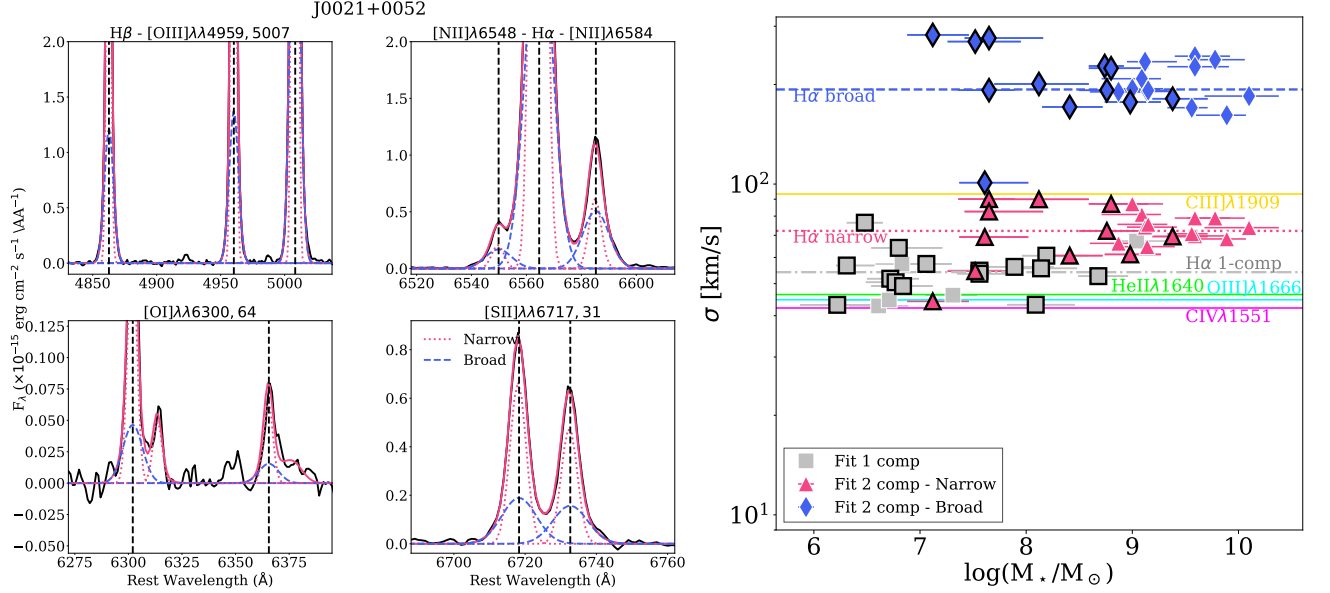


Figure 1. Left panel: optical emission lines best-fit with narrow and broad Gaussian components (dotted red and dashed blue lines, respectively; total fit shown by red solid line) for one of the CLASSY galaxies, J0021+0052. Here we show the lines needed to create the classical optical BPT diagrams ($H\beta$, $[O\ III]\ \lambda\lambda 4959, 5007$, $[N\ II]\ \lambda\lambda 6548, 84$, $H\alpha$, $[O\ I]\ \lambda\lambda 6300, 64$, $[S\ II]\ \lambda\lambda 6717, 31$) to discriminate among different ionization sources (see Sec. 4). The emission line next to $[O\ I]\ \lambda 6300$ is $[S\ III]\ \lambda 6312$, while the one next to $[O\ I]\ \lambda 6364$ is $Si\ II\ \lambda 6371$. Right panel: intrinsic velocity dispersion σ (y-axis in log scale) for the 1-component (grey squares) and, when needed, the 2-component best-fit (narrow and broad components shown as red triangles and blue diamonds, respectively) of optical emission lines, as a function of the stellar mass. The broad component σ (median value ~ 190 km/s, dashed blue line) is generally larger than the narrow (~ 70 km/s, dotted pink line) and single (~ 55 km/s, dash-dotted grey line) components. Galaxies with at least one $S/N > 3$ UV emission line (i.e., $C\ III]\ \lambda\lambda 1907, 9$; $12 + \log(O/H) \lesssim 8.3$) are highlighted by a black thick edge. The UV lines intrinsic σ median values are generally consistent with the optical, as shown by the solid horizontal lines: $C\ IV]\ \lambda\lambda 1548, 51$ (magenta), $He\ II]\ \lambda 1640$ (green), $O\ III]\ \lambda\lambda 1661, 6$ (cyan), $C\ III]\ \lambda\lambda 1907, 9$ (gold).

described in detail in Paper IV Sec. 3.1. Finally, we performed the fit of the main UV and optical emission lines separately. In particular, we simultaneously fitted each spectrum taking into account a set of UV (from $[N\ IV]\ \lambda 1483$, $N\ IV]\ \lambda 1487$, to $[C\ III]\ \lambda 1907$, $C\ III]\ \lambda 1909$) and optical emission lines (from $[O\ II]\ \lambda\lambda 3727$ to $[S\ III]\ \lambda 9069$) with a linear baseline centered on zero and a single Gaussian, making use of the code MPFIT (Markwardt 2009), which performs a robust non-linear least squares curve fitting (see Paper IV Sec. 3.2 for more details).

We noted that the $H\alpha$ line, in particular, shows a broad component in many CLASSY galaxies (as shown in the top panel of Fig. 1 for J0021+0052). Therefore, we performed 2-component Gaussian fits to the main optical emission lines (i.e., $[O\ II]\ \lambda\lambda 3727, 9$, $H\delta$, $H\gamma$, $H\beta$, $[O\ III]\ \lambda\lambda 4959, 5007$, $[O\ I]\ \lambda\lambda 6300, 74$, $[N\ II]\ \lambda\lambda 6548, 84$, $H\alpha$, $[S\ II]\ \lambda\lambda 6717, 31$). In particular, we used a narrow ($\sigma < 200$ km/s) and a broad ($\sigma < 1000$ km/s) Gaussian component, tying the velocity and velocity dispersion of each component to be the same for all the emission lines. We applied a reduced chi-square χ^2 selection in order to state if a fit with a second component better reproduces the observed spectral profiles (see Sec. 3.2.2 of Paper IV for more details). Overall, a second broad component is needed in 24 out of 45 galaxies of our sample. This

component tends to be slightly blue-shifted ($\sim 50\text{--}80$ km/s) at increasing M_* and accounts for $\lesssim 30\%$ of the total emission (Paper IV).

The right panel of Fig. 1 shows the intrinsic velocity dispersion σ that we calculate from the optical emission lines as a function of the galaxy stellar mass for our sample⁵. In particular, we show either the single Gaussian σ (grey squares) or the narrow (red triangles) and broad component (blue diamonds) σ , according to the best-fit selected for each galaxy. The median values of the single, narrow, and broad components are ~ 55 km/s, ~ 70 km/s and ~ 190 km/s, respectively, as indicated by the dash-dotted grey, dotted red and dashed blue horizontal lines. The single Gaussian σ for the objects that need a 2-component fit is not shown, but its median value would be ~ 100 km/s, and thus much higher than the value calculated for the narrow component. Overall, the broad emission component can trace gas at different velocities along the line of sight due to different mechanisms, including stellar winds, galactic outflows or turbulence, linked

⁵ The emission line velocity dispersion σ refers to the $H\alpha$ line for the optical and is corrected for the instrumental broadening σ_{int} of the different instruments taken into account, assuming $\sigma = \sqrt{\sigma_{obs}^2 - \sigma_{int}^2}$.

to different ionization sources (e.g., stellar or AGN photoionization and/or shocks; Izotov & Thuan 2007; James et al. 2009; Amorín et al. 2012; Bosch et al. 2019; Komarova et al. 2021; Hogarth et al. 2020). Hence, in Sec. 4 we use σ to explore whether correlations exist between gas kinematics and the optical diagnostics tracing the level of ionization of the gas (e.g., Kewley et al. 2019).

In Fig. 1, the CLASSY targets with at least one UV emission line (i.e., C III] $\lambda\lambda 1907,9$) are highlighted by a black thick edge: they all have generally low stellar masses and $12+\log(\text{O}/\text{H}) \lesssim 8.3$. C III] $\lambda\lambda 1907,9$ is the most common UV emission line in CLASSY galaxies (observed in 28 objects) without considering Ly α (see Hu et al. 2023 or Paper VII), as it is usually seen in low-mass SFGs (e.g., Rigby et al. 2015; Maseda et al. 2017; Du et al. 2017). Specifically, all the CLASSY galaxies showing either He II $\lambda 1640$ (19) or O III] $\lambda 1666$ (22) have also C III] emission (see Paper IV). Also, these three emission lines are all visible in the 9 CLASSY galaxies characterized by C IV $\lambda\lambda 1548,51$ in pure emission. The colored solid horizontal lines in Fig. 1 indicate their median intrinsic velocity dispersions, which we calculated, taking into account COS instrumental resolution as well as the extension of the sources derived from the COS NUV acquisition images (see Paper II Sec. 2 and Sec 3.2; James et al. 2014 Sec. 3.2). In general, He II $\lambda 1640$, O III] $\lambda 1661,6$ and C IV $\lambda\lambda 1548,51$ share very similar values ($\sigma \sim 50$ km/s), consistent with optical emission lines at similar stellar masses. We will further comment on this in Sec. 6. We emphasize that the UV emission-line S/N is typically not high enough to detect faint broad components in the emission lines, apart from a few exceptions that show broad emission in C IV $\lambda\lambda 1548,51$, He II $\lambda 1640$ and [O III] $\lambda\lambda 1661,6$ (but not in C III]) (Paper IV, Sec. 3.3.). Also, UV lines are not seen in the most massive targets in which the optical line broad components are particularly enhanced. However, the fact that $\sigma(\text{C III])}$ is systematically higher than other UV lines ($\sigma(\text{C III])} \sim 90$ km/s) could indicate the presence of a hidden undetected broad component. A further discussion of the optical and UV kinematical properties of the sample can be found in App. A.

3. DIAGNOSTIC MODELS USED WITHIN THIS WORK

This work aims to understand how state-of-the-art models from the literature compare to observed line ratios of the CLASSY survey, using well-studied optical diagnostics and less well-constrained UV diagnostics. This section provides an overview of each model considered for the main sources of ionization found within galaxies: photoionization, AGN,

and shocks. We provide a summary of the models taken into account in Tab. 1. In the next sections of the paper, we investigate and comment on optical and UV diagnostics to distinguish between these different ionizing mechanisms.

Concerning stellar photoionization grid models (referred to as SF models hereafter), we take into account emission from H II regions around young stars, using nebular-emission models of SFGs from Gutkin et al. (2016) (G16 hereafter) based on two limiting cases: one instantaneous burst (single stellar population; SSP models) or constant activity with time (CST models). In particular, single-burst models, in which the emission is strongest at young ages (i.e., from 3-4 Myr up to 5-7 Myr if stellar rotation is included) and disappears as the massive star population evolves, are generally used for young stellar populations and very recent starbursts, and thus more consistent with the CLASSY galaxies and EoR systems. G16 models do not take into account either stellar rotation or stellar multiplicity, which would imply a longer duration of ionizing photon production (e.g., MIST models from Byler et al. 2017 models) and, in the latter case, a harder radiation field (e.g., Binary Population and Spectral Synthesis, ‘BPASS’ models from Xiao et al. 2018). Other possible differences between G16 and other models in the literature concern the choice of stellar libraries, IMF or the way to scale gas-phase metallicity for elements such as nitrogen and carbon⁶. For the purpose of this study, we take into account G16 models (with constant and burst of SF), BPASS models from Xiao et al. (2018)⁷ (X18 hereafter) and Byler et al. (2017) (B17 hereafter) models. G16 model parameters (see Tab. 1) are well matched with the AGN and shock grids that we present below, allowing us to make a consistent comparison between optical and UV diagnostic diagrams. On the other hand, X18 and B17 models allow us to explore the differences caused by the inclusion of interacting binary stars in the stellar population and stellar rotation, respectively (and thus a harder radiation field), as we show in Sec. 5 and App. C.1.

As shown in Feltre et al. (2016) Fig. 1, the ionizing spectrum powered by a lower metallicity stellar population is harder with respect to a more metal-enriched one, producing a different spectral energy distribution at photon energies greater than ~ 20 eV. However, it generally cannot account for ionic species with ionization energies above ~ 50 eV. Hence, the presence of emission lines requiring such ionization energy could be a good indicator of the presence of an additional ionization mechanism than SF (e.g., AGN or shocks). In this work, we take into account the AGN models from Feltre et al. (2016) (F16 hereafter).

⁶ The former has secondary nucleosynthetic production at high metallicity, while part of the latter returns to the ISM through metallicity-dependent processes such as stellar winds (see e.g., Byler et al. 2018 for more details).

⁷ <http://www.bpass.auckland.ac.nz>

Table 1. Summary of the models used in this work: constant (CST) and single-burst (single stellar population; SSP) Gutkin et al. (2016) grids (G16) and Xiao et al. (2018) BPASS models (X18) for SF, Feltre et al. (2016) (F16) for AGN narrow-line region (NLR), Alarie & Morisset (2019) (AM19) for shocks. The parameters include the ionizing spectrum, gas-phase metallicity (Z_{ISM}), ionization parameter $\log(U_S)$, dust-to-gas ratio (ξ_d), carbon-to-oxygen abundance (C/O), and initial mass function (IMF). ξ_d accounts for the depletion of metals onto dust grains in the ionized gas. We refer to Sec. 4 of Plat et al. (2019) to see the impact of the variation of the parameters that we fix in this work.

| Model | Parameters | Sampled Values | Notes |
|-------|---|--|--|
| G16 | Ionizing spectrum | CST SF; age = 100 Myr | Bruzual & Charlot (2003) stellar pop. synthesis models + Cloudy (Ferland et al. 2013). The values of gas-phase metallicity correspond to $12+\log(\text{O}/\text{H}) = 6.64, 7.64, 8.55, 8.88$ and $\log(Z_{ISM}/Z_{\odot}) = -2.2-0.04$. We tested all values of n_H , ξ_d and (C/O), but here we show only $n_H = 100 \text{ cm}^{-3}$, $\xi_d = 0.3$ and $(\text{C}/\text{O})/(\text{C}/\text{O})_{\odot} = 0.1, 0.72$. Special prescriptions for C and N because scale non-linearly with O (G16 Sec. 2.3.1; see Henry et al. 2000; Berg et al. 2016). |
| | Z_{ISM} $\log(n_H/[\text{cm}^{-3}])$ $\log(U_S)$ ξ_d $(\text{C}/\text{O})/(\text{C}/\text{O})_{\odot}$ IMF | 0.0001, 0.001, 0.008, 0.017; $Z_{\odot} = 0.01524$ 1, 2, 3, 4 -3.5, -3, -2.5, -2, -1.5, -1, 0.1, 0.3, 0.5 0.10, 0.14, 0.20, 0.27, 0.38, 0.52, 0.72, 1.00, 1.40; $(\text{C}/\text{O})_{\odot} = 0.44$ Chabrier (2003) ($m_{min} = 0.1 M_{\odot}$; $m_{up} = 100, 300, M_{\odot}$) | |
| G16 | Ionizing spectrum | SSP; age = 1 – 10 Myr | Same as in CST G16 grids. Given the absence of stellar rotation and multiplicity, the ionizing radiation drops at older ages than 5 Myr. All the parameters are as in CST models. In this work, we show only grids with $t = 3, 5, 10$ Myr. |
| X18 | Ionizing spectrum | SSP; age = 1 – 100 Myr | BPASS V2.1 population models (Stanway et al. 2016; Eldridge et al. 2017) + Cloudy (Ferland et al. 2013). The gas nebula is assumed without dust and a constant n_H with $12+\log(\text{O}/\text{H}) = 6.6, 7.61, 8.52, 8.93$ (matched to Z_*). In this work, we show only grids with $n_H = 100 \text{ cm}^{-3}$ and $t = 3, 10$ Myr. C, N and other elements fractions are scaled according to the population metallicity Z (see Table 2, Xiao et al. 2018). |
| | Z_{ISM} $\log(n_H/[\text{cm}^{-3}])$ $\log(U_S)$ | 0.0001, 0.001, 0.008, 0.020; $Z_{\odot} = 0.020$ 0–3 in 0.5 dex intervals -3.5, -3, -2.5, -2, -1.5 | |
| B17 | Ionizing spectrum | Bursts of SF; age $t = 0.5, 1, 2, 3, 4, 5, 6, 7, 10$ Myr | MESA Isochrones&Stellar Tracks + Cloudy + Flexible Stellar Population Synthesis code (Byler 2018). Stellar rotation and nebular line and continuum emission included. Ionizing radiation is strong at young ages (up to 5-7 Myr) and disappears as massive stars evolve. Larger metallicity range than G16 ($12+\log(\text{O}/\text{H}) \sim 6.93 - 8.68$). In this work, we show only $t = 3, 5, 10$ Myr. |
| | $\log(Z_{ISM}/Z_{\odot})$ $n_H/[\text{cm}^{-3}]$ $\log(U_S)$ IMF Others | -1.5, -1.0, -0.6, -0.4, -0.3, -0.2, -0.1, 0.0, 0.1, 0.2; $Z_{\odot} = 0.0142$ 100. Same as G16 Kroupa (2001) ($m_{min} = 0.1 M_{\odot}$; $m_{up} = 120, M_{\odot}$) N and C treated with equations reported in Byler et al. (2017). | |
| F16 | Ionizing spectrum | AGN NLR; $\alpha = -1.2, -1.4, -1.7, -2.0$ | Cloudy models with open geometry, luminosity $L_{AGN} = 10^{45} \text{ erg/s}$, inner radius from the NLR of 300 pc. Ionizing spectrum parameterized with the power-law index α of the spectral energy distribution of the incident ionizing radiation from the AGN accretion disc at UV and optical wavelengths in AGN models. All heavy elements except for nitrogen (see F16 Eq. 6) are assumed to scale linearly with oxygen abundance. |
| | Z_{ISM} $n_H/[\text{cm}^{-3}]$ $\log(U_S)$ ξ_d | Same as G16 Same as G16 Same as G16 Same as G16 | |
| AM19 | Ionizing spectrum | Fast shocks ($v_s > 100 \text{ km/s}$) | Mappings-V (Sutherland & Dopita 2017) and a plane-parallel geometry. Models created using same prescriptions of the well-known Allen et al. (2008) shock models by AM19, but using the metallicity values of G16, to study variation with metallicity. We tested all values, but in this paper we show only grids with $n_H = 1 \text{ cm}^{-3}$, $(\text{C}/\text{O})/(\text{C}/\text{O})_{\odot} = 0.26$ for $Z_{ISM} = 0.0001, 0.001$ and $(\text{C}/\text{O})/(\text{C}/\text{O})_{\odot} = 1.00$ for $Z_{ISM} = 0.017$ (trans-solar metallicity grid). |
| | Z_{ISM} $n_H/[\text{cm}^{-3}]$ $v_s/[\text{km/s}]$ $(\text{C}/\text{O})/(\text{C}/\text{O})_{\odot}$ $B_{\text{O}}/[\mu\text{G}]$ | 0.0001, 0.001, 0.008, 0.08, 0.017 1, 10, 100, 1000, 10000. 100, 125, ..., 1000 0.26, 1.00 $10^{-4}, 0.5, 1.0, 2.0, 3.23, 4.0, 5.0, 10$ | |

The main parameters in F16 models are the slope α of the ionizing spectrum⁸, as well as the other quantities shown in detail in Tab. 1. Collisional excitation and photoionization from slow ($v \lesssim 150$ km/s) and fast shocks ($v \sim 150 - 1000$ km/s), respectively, can also produce a rich spectrum of UV and optical emission lines, since shocked regions have high electron temperature and ionization state (Dopita & Sutherland 2003). Here we take into account the shock models from the 3MdBs⁹ database (Alarie & Morisset 2019; AM19). These model grids span a broad range of metallicity, matched with G16 grid values (see Tab. 1), with respect to the well-known MAPPINGS models from Allen et al. (2008)¹⁰, and thus are the best suited for the CLASSY sample. The emission line spectra primarily depend on the shock velocity v_s and the magnetic field parameter B_0 , which regulate the shock ionization spectrum and the effective ionization parameter. An increase in the density of the material preceding the shock ionization front (preshock density n_H) can play a role as well because it enforces the collisional de-excitation of forbidden lines. Generally, two sets of models are taken into account: shocks and shocks+precursor. The precursor emission becomes important at increasing velocities of the shock front ($v \gtrsim 170$ km/s), where the ionization front velocity exceeds v_s . Indeed, the high velocity causes the photoionization front to detach from the shock and form a “precursor”, which can contribute to or even dominate the shock emission. In general, we noticed that an increase in density from $n_H \sim 1 \text{ cm}^{-3}$ to $n_H \sim 1000 \text{ cm}^{-3}$ does not lead to dramatic changes in the optical and UV line ratios discussed in the following sections unless noted in the text. Hence, in this work, we show only grids with $n_H = 1 \text{ cm}^{-3}$ (consistently with shock grids usually shown in other works; e.g., Allen et al. 2008). Also, at sub-solar metallicities, we show the grids with $(C/O)/(C/O)_\odot = 0.26$, which are also more consistent with the properties of the CLASSY galaxies.

4. RESULTS: OPTICAL DIAGNOSTICS SENSITIVE TO THE IONIZATION SOURCE

In this Section we present the most frequently used classification methods in the optical, showing and discussing where the CLASSY galaxies are located in different diagnostic diagrams. In particular, we compared different criteria to discriminate between ionization processes, sometimes finding that there is not a one-to-one agreement in classification, especially for low-mass and low-metallicity galaxies

(e.g., Groves et al. 2006; Shirazi & Brinchmann 2012; Sartori et al. 2015; Polimera et al. 2022; Nakajima & Maiolino 2022). In Table 2, we summarize the explored optical diagnostics and the corresponding classifications for each galaxy. Overall, a combination of criteria represents the best way to provide a robust determination of the main ionization source.

Before going into the details listed in this Section, here we disclose our main results about optical diagnostics. In this work, we find that CLASSY galaxies are characterized by [O III]/H β narrow and broad components typical of star-forming galaxies. Furthermore, their broad components — if present — have enhanced [N II]/H α (and slightly enhanced [S II]/H α and [O I]/H α) and [O I]/[O III] (possible shock evidence), but lower [O III]/[O II] (i.e., lower level of ionization) and do not show a trend with He II λ 4686 (that could be enhanced by shocks/AGN). We do not preclude that a few of them can have shocks (and possibly hidden AGN activity in the trans-solar galaxy J0808+3948), but, in general, the main ionizing mechanism is clearly star formation. This conclusion is not surprising since the sample was selected excluding targets with a classification other than star-forming, but here we further confirmed it by exploring different diagnostic diagrams.

Performing this optical-diagnostic test is important since in Sec. 5 we test how UV diagnostic diagrams compare to the well-known and reliable optical ones presented here. In the following plots, we highlight with a black thick edge the objects with at least one UV line detection (i.e., $S/N(\text{C III}) \lambda\lambda 1907,9 > 3$), since only a sub-sample of low-metallicity objects shows UV emission lines.

4.1. The classical optical BPT diagrams

The three panels of Fig. 2 illustrate the [N II], [S II] and [O I]-BPT diagrams for the single (grey squares), narrow (red triangles) and broad (blue diamonds) components of the CLASSY galaxies. The SF models are not shown for clarity reasons but can completely cover the classical SF locus, while the F16 models predict higher [O III]/H β , consistently with the classical AGN locus. According to these diagnostics, the majority of the CLASSY galaxies are dominated by SF, even though the classification is not always consistent among different diagnostics, with many objects at the edge of the SF locus (indicated by the black solid maximum starburst line). In particular, at these edges, we mainly find the CLASSY objects characterized by UV emission lines (highlighted by thick black edges), that have generally higher [O III]/H β than the others and low gas-phase metallicity ($12 + \log(\text{O}/\text{H}) \lesssim 8.3$, corresponding to $Z \lesssim 50\% Z_\odot$). However, as we discuss in the following paragraphs, two main factors can affect the definition of the SF locus and need to be taken into account: the metallicity and the hardness of the radiation field.

⁸ The luminosity per unit frequency S_ν of the AGN accretion disc is usually approximated by a broken power law, with $S_\nu \sim \nu^\alpha$ at wavelengths $0.001 \leq \lambda/\mu \leq 0.25$, as shown in Eq. 5 of F16

⁹ <http://3mdb.astro.unam.mx/>

¹⁰ AM19 models are made with MAPPINGS-V and agree with Allen et al. (2008) predictions at LMC metallicity (see AM19 for more details).

Table 2. CLASSY sample (name and alternative name shown in (1) and (2)) classification according to the optical diagnostic diagrams taken into account: [N II]-BPT (3), [S II]-BPT (4), [O I]-BPT (5), the [OI]-[OII]-[OIII] discussed in Sec. 4.2 (6), He II-diagram discussed in Sec. 4.3 (7). The dominant ionization mechanism is classified as star formation (SF), composite (Comp), Active Galactic Nuclei (AGN), or, if one or more of the involved lines have $S/N < 3$, not classified (NC). The ‘...’ indicates that some of the involved emission lines are out of the observed wavelength range. Columns (3), (4), and (5) report the classification using the standard separators shown in black in Fig. 2. According to the updated BPT separators from X18 (shaded green in Fig. 2) all the galaxies are classified as SF dominated. None of the CLASSY galaxies are classified as a low-ionization (nuclear) region or LI(N)ER. For the optical diagnostics, we specify the classification of both the narrow (N) and (B) components - if present. The 28 galaxies in bold are those which show a 3σ detection in C III] $\lambda\lambda 1907,9$ ($12+\log(O/H) \lesssim 8.3$, $Z \lesssim 50\%$ Z_{\odot}).

| Object | | [NII]-BPT N/B | [SII]-BPT N/B | [OI]-BPT N/B | [OI]-[OII]-[OIII] N/B | HeII N/B |
|-------------------|------------------|------------------|------------------|-----------------|--------------------------|-------------|
| J0021+0052 | | SF/SF | SF/SF | SF/SF | SF/SF | SF |
| J0036-3333 | Haro 11 knot C | SF/SF | SF/SF | SF/SF | SF/SF | SF |
| J0127-0619 | Mrk 996 | SF/SF | SF/NC | SF/NC | SF/NC | NC |
| J0144+0453 | UM 133 | SF/NC | AGN/NC | AGN/NC | SF/NC | SF |
| J0337-0502 | SBS 0335-052 E | SF/NC | SF/NC | SF/NC | SF/NC | SF/NC |
| J0405-3648 | | SF | SF | SF | SF | SF |
| J0808+3948 | | Comp/SF | SF/SF | SF/SF | AGN-shocks/NC | AGN |
| J0823+2806 | LARS9 | SF/Comp | SF/SF | SF/SF | SF/SF | SF |
| J0926+4427 | LARS14 | SF/Comp | AGN/SF | AGN/SF | SF/SF | NC |
| J0934+5514 | Izw 18 | ... | ... | ... | ... | SF |
| J0938+5428 | | SF/SF | SF/SF | SF/SF | SF/SF | SF |
| J0940+2935 | | SF | SF | SF | SF | NC |
| J0942+3547 | CG-274, SB 110 | SF | SF | SF | SF | SF |
| J0944+3442 | | SF | SF | SF | AGN-SF | NC |
| J0944-0038 | CGCG007-025 | SF | SF | SF | SF | SF |
| J1016+3754 | 1427-52996-221 | SF | SF | SF | SF | SF |
| J1024+0524 | SB 36 | SF | SF | SF | SF | SF |
| J1025+3622 | | SF/SF | SF/SF | AGN/SF | SF/SF | SF |
| J1044+0353 | | SF | SF | SF | SF | SF |
| J1105+4444 | 1363-53053-510 | SF/SF | SF/SF | SF/AGN | SF | SF |
| J1112+5503 | | Comp/SF | SF/SF | SF/SF | SF/SF | Comp |
| J1119+5130 | | SF | SF | SF | SF | SF |
| J1129+2034 | SB 179 | SF | SF | SF | SF | SF |
| J1132+1411 | SB 125 | SF | SF | SF | SF | SF |
| J1132+5722 | SBSG1129+576 | SF | SF | SF | SF | SF |
| J1144+4012 | | SF/SF | SF/SF | SF/SF | SF | NC |
| J1148+2546 | SB 182 | SF | SF | SF | SF | SF |
| J1150+1501 | SB 126, Mrk 0750 | SF | SF | SF | SF | SF |
| J1157+3220 | 1991-53446-584 | SF | SF | SF | SF | SF |
| J1200+1343 | | Comp/Comp | SF/SF | AGN/NC | SF/NC | SF |
| J1225+6109 | 0955-52409-608 | SF/NC | SF/NC | SF/NC | SF/NC | SF |
| J1253-0312 | SHOC391 | ... | ... | ... | SF/SF | NC |
| J1314+3452 | SB 153 | SF | SF | SF | SF | SF |
| J1323-0132 | | SF | SF | SF | SF | SF |
| J1359+5726 | Ly 52, Mrk 1486 | SF/SF | SF/SF | SF/SF | SF/SF | SF |
| J1416+1223 | | Comp/SF | SF/SF | SF/SF | SF/SF | NC |
| J1418+2102 | | SF | SF | SF | SF | SF |
| J1428+1653 | | SF/SF | SF/SF | SF/SF | SF/SF | NC |
| J1429+0643 | | SF/SF | AGN/SF | AGN/AGN | SF/SF | SF |
| J1444+4237 | HS1442+4250 | SF | SF | SF | SF | NC |
| J1448-0110 | SB 61 | SF | SF | SF | SF | SF |
| J1521+0759 | | SF/SF | SF/SF | AGN/SF | SF/SF | NC |
| J1525+0757 | | SF/SF | SF/SF | SF/SF | SF/SF | NC |
| J1545+0858 | 1725-54266-068 | SF/Comp | SF/SF | SF/AGN | SF/SF | SF |
| J1612+0817 | | Comp/Comp | SF/SF | SF/SF | SF/SF | SF |
| (1) | (2) | (3) | (4) | (5) | (6) | (7) |

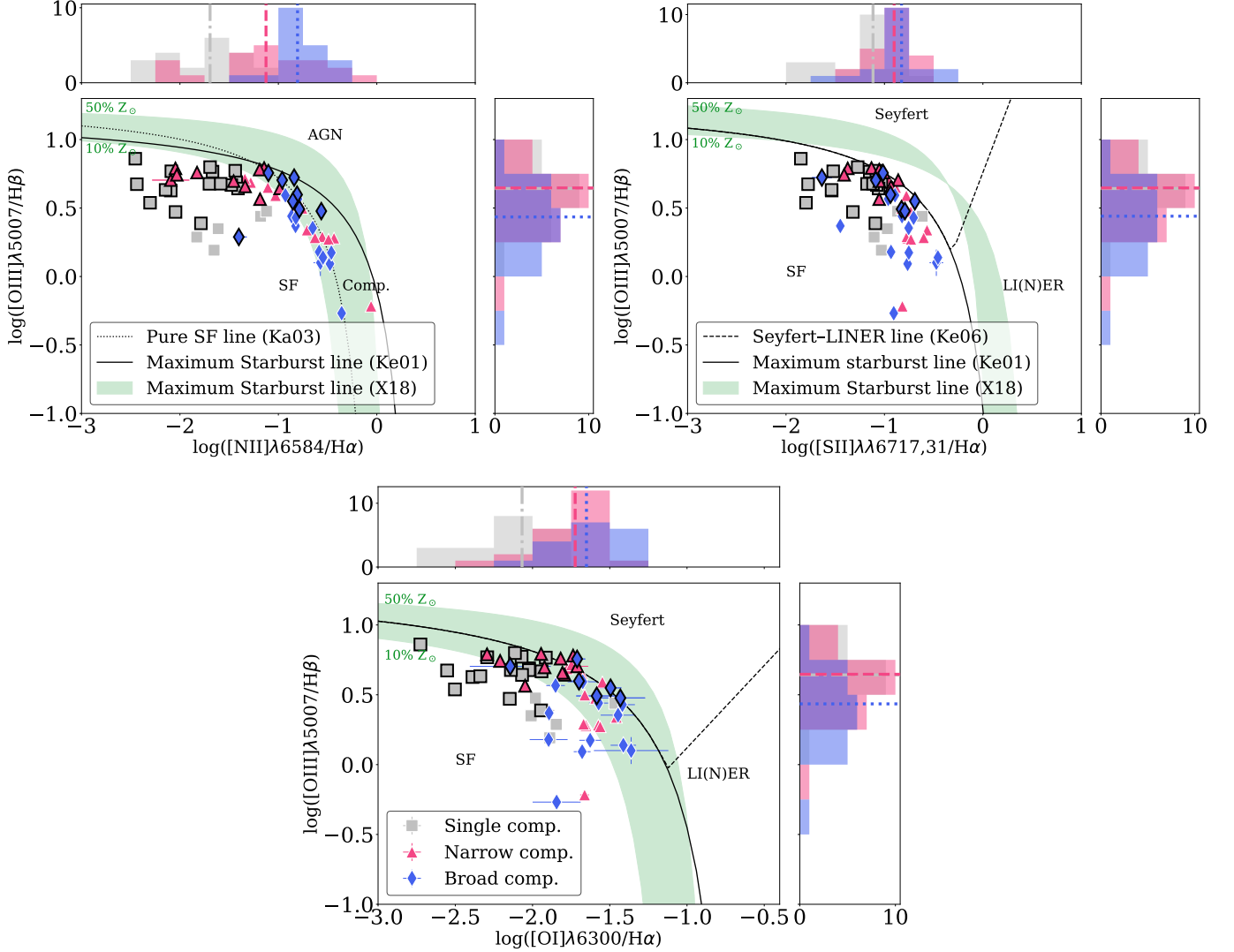


Figure 2. [N II] (top left), [S II] (top right), and [O I] (bottom) BPT diagrams for the single, narrow and broad components, shown as gray squares, red triangles and blue diamonds, respectively. All the measurements have $S/N > 3$ for all the lines involved. The black dotted curve is the empirical relation to divide pure star-forming from Seyfert–H II composite objects by [Kauffmann et al. \(2003\)](#), while the black solid curves are the maximum starburst line derived by [Kewley et al. \(2001\)](#). The black dashed lines are the [Kewley et al. \(2006\)](#) boundary between Seyferts and low-ionization (nuclear) emission-line regions (LI(N)ERs; see also [Heckman 1980](#); [Belfiore et al. 2016](#)). Histograms showing the distribution of [N II]/H α , [S II]/H α , [O I]/H α , and [O III]/H β line ratios in the single, narrow and broad components are shown in gray, red and blue, respectively, on each axis, with median values shown by the dash-dotted, dashed and dotted black lines. The broad component clearly shows higher x-axis line ratios. The green-shaded regions represent the maximal starburst predictions at metallicity between 10% Z_{\odot} and 50% Z_{\odot} values, using pure stellar photoionization including massive star binaries through the BPASS stellar evolution models ([Xiao et al. 2018](#)), to show the extent to which the maximal starburst line can change in the metallicity range in which we observe UV emission lines. According to the updated BPT separators from [X18](#), thus taking into account the gas-phase metallicity of each target, all the galaxies are classified as SF dominated. The galaxies with at least one UV emission line (i.e., C III] $\lambda\lambda 1907,9$) are highlighted by a black thick edge.

On the one hand, $[\text{N II}]/\text{H}\alpha$ is particularly sensitive to metallicity (Kewley & Dopita 2002; Denicoló et al. 2002; Pettini & Pagel 2004; Kewley & Ellison 2008), with lower $[\text{N II}]/\text{H}\alpha$ at decreasing metallicity (see e.g., the CLASSY galaxies J1323-0132 and J0808+3948 in Paper V Fig. 2). Since higher $[\text{N II}]/\text{H}\alpha$ line-ratios are required to classify galaxies as AGN, the $[\text{N II}]$ -BPT by itself is not sufficient for identifying AGN in typical low-metallicity star-forming $z \sim 0$ galaxies (e.g., Groves et al. 2006; Reines et al. 2020; Molina et al. 2021; Polimera et al. 2022). For instance, Polimera et al. (2022) showed that the $[\text{O I}]$ -BPT¹¹ can identify a theoretical dwarf AGN with a spectrum characterized by $\sim 90\%$ SF contribution and classified as star-forming according to the $[\text{N II}]$ -BPT (see also Hogarth et al. 2020). Indeed, $[\text{O I}]/\text{H}\alpha$ is highly sensitive to hard radiation fields, particularly shock emission in the neutral ISM (e.g., Osterbrock & Ferland 2006; Allen et al. 2008) and is not very dependent on metallicity. Hence, an $[\text{O I}]/\text{H}\alpha$ enhancement could suggest that there is an additional excitation mechanism other than stellar photoionization, missed by the $[\text{N II}]$ -BPT diagram. Looking at Table 2, some galaxies are classified as SF-dominated according to the $[\text{N II}]$ -BPT and as “AGN” according to the $[\text{O I}]$ -BPT, because they are located slightly beyond the Kewley et al. (2006) maximal starburst line. However, here we stress that the $[\text{O I}]\lambda 6300$ line is fainter than $[\text{N II}]$ and $[\text{S II}]$, and thus the $[\text{O I}]/\text{H}\alpha$ line ratio has larger error bars, as shown in Fig. 2.

On the other hand, low metallicity stellar populations produce harder radiation fields and thus higher $[\text{O III}]/\text{H}\beta$ (and lower low-ionization line ratios) without the need to invoke other mechanisms than SF (e.g., Feltre et al. 2016; Byler et al. 2018; Xiao et al. 2018). In this context, X18 explored the variation of the *maximal starburst line* (i.e., the highest line ratios reproduced with SF models) in BPT diagrams as a function of the metallicity, using pure stellar photoionisation including massive star binaries through the BPASS (Binary Population and Spectral Synthesis; Eldridge & Stanway 2009) stellar evolution models¹². The green shaded regions in Fig. 2 show the predictions of the X18 *maximal starburst lines* between $Z \sim 10\% Z_{\odot}$ and $Z \sim 50\% Z_{\odot}$ to underline how difficult the separation between different ionization mechanisms can be for galaxies that lie very close to the edges of the classical BPT diagrams in this range of metallicity (at which we observe also the UV emission lines we discuss in Sec. 5). Overall, we stress that taking into account the criteria of X18 and the gas-phase metallicity measured

for each object of our sample, all the galaxies are classified as SF dominated.

Another interesting implication from Fig. 2 is that the broad component of our galaxies is usually characterized by higher $[\text{N II}]/\text{H}\alpha$ and $[\text{O I}]/\text{H}\alpha$, slightly higher $[\text{S II}]/\text{H}\alpha$, and slightly lower $[\text{O III}]/\text{H}\beta$ line ratios. This difference is shown by the grey, red and blue histograms on each axis of Fig. 2, and is more enhanced when comparing results of the single-Gaussian fit with the broad component of the two-Gaussian fit (up to ~ 1 dex in $\log([\text{N II}]/\text{H}\alpha)$ and ~ 0.5 dex in $\log([\text{O I}]/\text{H}\alpha)$). In particular, strong low-ionization lines could be a signature of shocks (Osterbrock & Ferland 2006). Also, the broad component has (by definition) a much larger velocity dispersion than the narrow one, as shown in Fig. 1. This σ enhancement at increasing $[\text{N II}]/\text{H}\alpha$, $[\text{S II}]/\text{H}\alpha$, and $[\text{O I}]/\text{H}\alpha$ line ratios suggests that the kinematics and ionization state could be coupled, implying the same physical origin, which could be different from the one producing the narrow components. This correlation has been already found in normal star-forming galaxies and AGN (e.g., Ho et al. 2014; Mingozzi et al. 2019; Hogarth et al. 2020), and it was attributed to a shocked gas component, as stellar/AGN photoionization is not expected to cause such a trend (see e.g. Dopita & Sutherland 1995; Rich et al. 2010; McElroy et al. 2015; Kewley et al. 2019). We note that the σ enhancement is more evident in $[\text{N II}]/\text{H}\alpha$ and so could also be related to a nitrogen enhancement of the more perturbed gas (e.g., James et al. 2009). We will explore this further in Arellano-Córdova et al. 2023 in prep.

Finally, in Appendix B we also comment about an alternative optical BPT diagnostic diagram that exploits only line ratios in the blue part of the optical spectrum (i.e., $[\text{O II}]\lambda\lambda 3727/\text{H}\beta$ versus $[\text{O III}]\lambda 5007/\text{H}\beta$, Fig. 12; Lamareille et al. 2004; Lamareille 2010)¹³.

To summarize, since $[\text{O III}]/\text{H}\beta$ is in the star formation locus in the BPT diagrams (Fig 2) and is not enhanced in the broad component, we think that is unlikely that AGN are present in our sample. Here we acknowledge that recently Hatano et al. (2023) claimed that SBS 0335-052 E hosts an AGN on the basis of a recent NIR variability and the broad $\text{H}\alpha$ component. We also reveal a broad $\text{H}\alpha$ component ($\sigma \sim 1000\text{km/s}$) not visible in the other emission lines (this could be due to low S/N and low metallicity), but the narrow component line ratios analyzed in this work are all classified as SF-dominated. Finally, the $[\text{O I}]$ -excess that we observe in some galaxies of the sample, as well as the increase of $[\text{N II}]/\text{H}\alpha$, $[\text{S II}]/\text{H}\alpha$, and $[\text{O I}]/\text{H}\alpha$ line ratios with

¹¹ Polimera et al. (2022) also tested the $[\text{S II}]$ -BPT diagram, which resulted in being less sensitive to SF dilution compared to the $[\text{O I}]$ -BPT.

¹² Binary-star evolution pathways produce harder radiation up to older ages than single stars mainly because of the gas accretion onto compact objects (e.g., HMXBs).

¹³ This diagram is useful to check two galaxies of our sample, the famous blue compact dwarf I Zw 18 (J0934+5514) and J1253-0312, which are not shown in Fig. 2 because we do not have $\text{H}\alpha$ coverage (see Paper IV Sec. 3). These two objects are classified as star-forming in Fig. 12.

velocity dispersion, indicate the possible presence of additional mechanisms such as shocks, which we further discuss in the following section.

4.2. [OI] $\lambda 6300$ as a shock indicator

Fig. 3 shows the [O III] $\lambda 5007$ /[O II] $\lambda\lambda 3727$ versus [O I] $\lambda 6300$ /[O III] $\lambda 5007$ diagram ([OI]-[OII]-[OIII] diagram) for the CLASSY galaxies (single, narrow and broad components shown as in Fig. 2), presented as a diagnostic plot for the first time in Heckman (1980) to separate Seyferts from LINERs (see also Stasińska et al. 2015). This diagram is not very dependent on gas-phase metallicity (Stasińska et al. 2015), avoiding the drawbacks discussed for the classical [N II]-BPT diagram. Clearly, Fig. 3 represents a good tool to discriminate between SF, AGN, and shocks for our sample, as also shown by the good separation of the SF, AGN, and shock model grids, with just a slight overlap between the grids at the highest [O I]/[O III] line ratios¹⁴. We highlight that increasing the preshock density n_H from $n_H \sim 1 \text{ cm}^{-3}$ to $n_H \sim 1000 \text{ cm}^{-3}$ would lead to higher $\log([\text{O III}]/[\text{O II}])$, that can increase up to $\sim 0.5 - 1.5$ for shock+precursor and pure-shock grids, respectively. Still, shock models are generally characterized by higher $\log([\text{O I}]/[\text{O III}])$ than AGN models, reaching values up to ~ 1 . The dashed blue line

$$y = -0.84x - 1.0 \quad (1)$$

qualitatively separates the SF from AGN/shock models, while the dash-dotted black line indicates the AGN locus:

$$\begin{aligned} y &= -0.15 \quad \text{and} \quad -0.96 < x < -0.3 \\ y &= -1.75x - 0.70 \quad \text{and} \quad -3.5 < x < -0.3 \end{aligned} \quad (2)$$

with $y = \log([\text{O III}] \lambda 5007 / [\text{O II}] \lambda\lambda 3727)$ and $x = \log([\text{O I}] \lambda 6300 / [\text{O III}] \lambda 5007)$.

Overall, Fig. 3 shows that the vast majority of the CLASSY galaxies can be reproduced by SF models, further confirming the classification obtained with the classical BPT diagrams (Fig. 2). In particular, the optical line broad velocity components show a significant enhancement in terms of the [O I]/[O III] line ratio (with the broad showing a larger median value by ~ 0.5 dex and ~ 1 dex than the narrow and single components, respectively; except for J0926+4427, J1148+2546 and J1253-0312) and a lower [O III]/[O II] (in all galaxies except for J1148+2546). Shocks can naturally explain high [O I]/[O III] line ratio with high [O III]/[O II], while photoionization models that produce high [O I]/[O III] show, in turn, low [O III]/[O II] (e.g., Stasińska et al. 2015; Plat et al.

2019). This suggests that also the more turbulent ionized gas has a stellar source of ionization. The narrow components of only two CLASSY galaxies are at the edge of the SF locus defined by our Eq. 1 in this diagram: J0944+3442 and J0808+3948, which could be both consistent with AGN and shock models. J0944+3442 is classified as star-forming according to the optical BPT diagrams, while only the narrow component of J0808+3948 is classified as composite according to the [N II]-BPT diagram. J0808+3948 has also an extremely high nitrogen enhancement and high N/O (Arellano-Córdova et al. 2023 in prep.; see also Stephenson et al. 2023). We stress that these galaxies have no detections of UV lines, so are not shown in the UV diagnostic diagrams discussed in Sec. 5 (J0808+3948 is the only trans-solar metallicity galaxy of the sample ($12+\log(\text{O}/\text{H}) \sim 8.77$); J0944+3442 has instead low-metallicity ($12+\log(\text{O}/\text{H}) 7.83$).

Even though the [O III]/[O II] versus [O I]/[O III] diagram can be a very good tool to understand the role of shocks and separate SF from harder mechanisms, it can also have drawbacks. [O I] $\lambda 6300$ is produced in the warm transition region between the fully ionized gas and neutral gas (Osterbrock & Ferland 2006; Draine 2011). As such, it traces the external parts of H II regions, close to the ionization front, where shocks and non-equilibrium heating are important (Dopita & Sutherland 2003; Dopita et al. 2013), which makes it difficult to predict [O I] $\lambda 6300$ in photoionization models (Dopita et al. 2013). Furthermore, [O I] $\lambda 6300$ is generally a faint emission line (this makes it even more tricky to disentangle a broad second component). Nevertheless, an observed [O I] $\lambda 6300$ enhancement could still represent a sign of ionizing mechanisms other than SF. Overall, the values of the discussed oxygen line ratios are mostly consistent with SF models, further confirming the lack of strong ionizing shocks and/or AGN activity in the CLASSY galaxies.

4.3. The Shirazi-Brinchmann diagram

To further confirm the SF classification of CLASSY galaxies we also consider high-ionization lines such as He II $\lambda 4686$. Indeed, as introduced in Sec. 1, Shirazi & Brinchmann (2012) proposed to use He II $\lambda 4686/\text{H}\beta$ versus [N II]/ $\text{H}\alpha$ to better constrain the ionization source. The two major advantages of this diagram (HeII diagram) are that (i) it is more sensitive to the hardness of the ionizing source than [O III]/ $\text{H}\beta$, thus allowing a cleaner separation between star-forming and composite galaxies; and (ii) it is not particularly sensitive to the metallicity (Shirazi & Brinchmann 2012). The HeII diagram for the CLASSY sample is shown in Fig. 4 and is color-coded as a function of $12+\log(\text{O}/\text{H})$ (the broad component fit of He II $\lambda 4686$ line is not detected because of the low S/N). Similarly to the standard BPT diagrams described in Sec. 4.1, SFGs are expected to lie below the maximum starburst (black solid) line, while AGN

¹⁴ Kewley et al. (2019) present different shock diagnostics (see their Fig. 11), including one comparing [O III]/[O II] versus [O I]/ $\text{H}\alpha$, that we tested but excluded because the AGN and SF grids of models could not be separated as well as in Fig. 3.

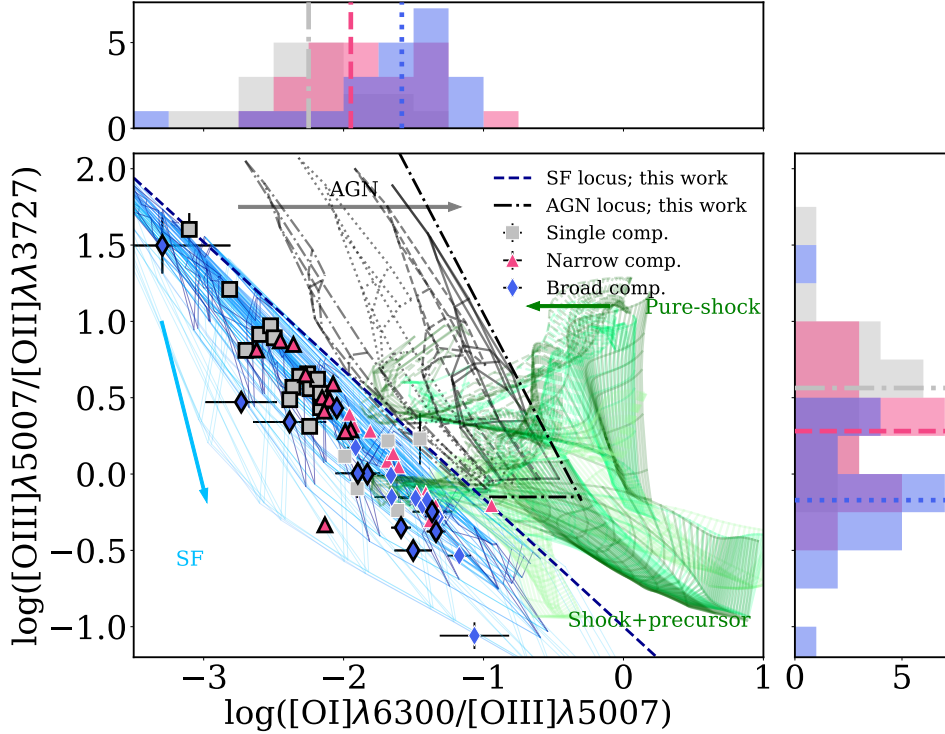


Figure 3. Location of the CLASSY galaxies in the $\log([\text{O III}]/[\text{O II}])$ versus $\log([\text{O I}]/[\text{O III}])$ diagnostic diagram from Kewley et al. (2019) (see also Stasińska et al. 2015). The single, narrow and broad components are shown as grey squares, red triangles, and blue diamonds and the histograms on the axes show their distributions and median value as in Fig. 2. The blue grids show the G16 single-burst SF models, with ages of 3 Myr (darker blue) and 5 Myr (lighter blue). The G16 SF grids indicatively follow the blue arrow at increasing ages. The G16 constant SF models are not shown for clarity, because they completely overlap the single-burst grids. The black grids show the F16 AGN models, with the parameter α increasing from -2 (dashed-dotted grid) to -1.2 (solid grid) - and thus harder AGN ionizing radiation - in the direction of the black arrow. AM19 pure-shock (dashed) and shock+precursor (solid) model grids at varying velocities and magnetic fields are shown at different metallicities, with increasing values from lighter to darker green (following the green arrow). Shock models are more sensitive to the metallicity and have $\log([\text{O III}]/[\text{O II}]) \gtrsim 0$, but lower $\log([\text{O I}]/[\text{O III}]) (\lesssim 0)$ than shock+precursor ones, that can reach $\log([\text{O I}]/[\text{O III}]) \lesssim 1$. The dashed blue line qualitatively separates the SF from AGN/shock models, while the dash-dotted black line indicates the AGN locus. This plot represents a good tool to separate SF, AGN and shock models for our sample, which includes sub-solar to solar metallicity targets, underlining the importance of $[\text{O I}] \lambda 6300$ as a good shock diagnostic at optical wavelengths. Only two CLASSY galaxies are at the edge of the star-forming locus. The galaxies with at least one UV emission line (i.e., $\text{C III}] \lambda \lambda 1907,9$; $12+\log(\text{O}/\text{H}) \lesssim 8.3$) are highlighted by a black thick edge.

are located above. The G16 models are not shown for clarity reasons but can completely cover the star formation locus. Almost all the CLASSY galaxies shown in the HeII diagram are classified as star-forming. The only targets with a different classification are J0808+3948 (classified as AGN) and J1112+5503 (at the edge between the SF and composite locii). However, we emphasize that their He II lines are particularly faint ($S/N \sim 3-5$), hence this classification is not reliable by itself. Given that J0808+3948 is not located in the SF locus also in Fig. 3 and in the $[\text{N II}]-\text{BPT}$ (Fig. 2), we conclude that it is possible that this galaxy has a further ionizing mechanism than pure SF. In Sec. 4.1 and 4.2 we could not exclude the presence of shocks in our targets, but, if present, shocks should easily enhance the He II $\lambda 4686$ flux (e.g., Shirazi & Brinchmann 2012; Stasińska et al. 2015). However, here we stress that we do not see a particular enhancement of He II at increasing $[\text{O I}]/[\text{O III}]$, which we con-

sider a good shock diagnostic (Fig. 3) or in galaxies where we identify a second broader component characterized by higher $[\text{N II}]/\text{H}\alpha$, $[\text{S II}]/\text{H}\alpha$, and/or $[\text{O I}]/\text{H}\alpha$, as shown and discussed in Fig. 2. This is a further confirmation of the SF classification of our systems.

Finally, we highlight that almost all the $\text{C III}] \lambda \lambda 1907,9$ -emitters are shown in Fig. 4. Those missing are: Izw 18 and J1253-0312, because without $\text{H}\alpha$ measurement in our sample, but with $\log(\text{He II } \lambda 4686/\text{H}\beta) \sim -1.35, -1.86$ and $12+\log(\text{O}/\text{H}) \sim 6.98, 8.06$, respectively, and thus still lying in the SF locus; Mrk 996 (J0127-0619) with an unreliable He II $\lambda 4686$ flux measurement, due to the contamination from the WR red clump, but still classified as star-forming (see James et al. 2009 for further details); J1444+4237, which does not show He II $\lambda 4686$ emission (upper limit of $\log(\text{He II } \lambda 4686/\text{H}\beta) \lesssim -1.8$), even though it has bright UV emission lines. Overall, all the galaxies that we will show in

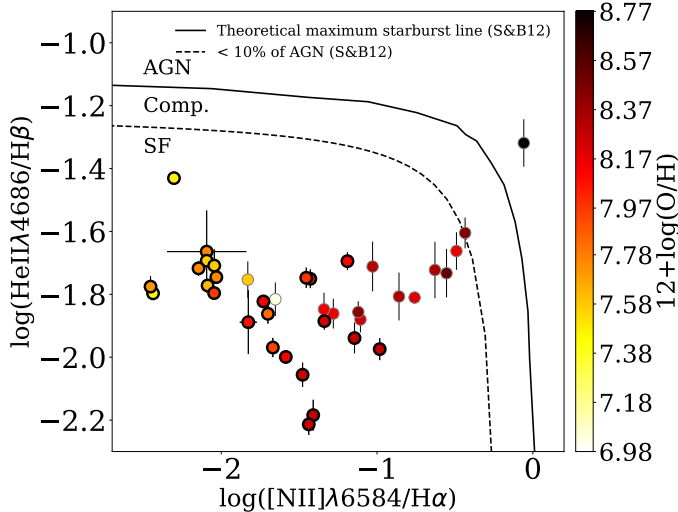


Figure 4. He II $\lambda 4686/H\beta$ versus [N II] $\lambda 6584/H\alpha$ diagnostic diagram for the CLASSY galaxies, shown as dots, color-coded as a function of the gas-phase metallicity. Only the measurements with $S/N > 3$ for all the lines involved are reported. The dotted and solid black lines represent the locus where $\sim 10\%$ of He II $\lambda 4686$ comes from an AGN and the theoretical maximum starburst line, respectively, as defined by Shirazi & Brinchmann (2012). Only two CLASSY galaxies are outside the star-forming locus, but we note that their He II $\lambda 4686$ lines are particularly faint ($S/N \lesssim 5$), hence this classification is not reliable by itself. The galaxies with at least one UV emission line (i.e., C III] $\lambda\lambda 1907,9$; $12+\log(O/H) \lesssim 8.3$) are highlighted by a black thick edge.

Sec. 5 are classified as SF-dominated also according to the Shirazi & Brinchmann (2012) criterion.

4.4. The importance of optical coronal lines

As a concluding note on optical diagnostics, we discuss the so-called coronal lines as proof of the presence of AGN activity. These are high-ionization (≥ 70 eV) forbidden transitions excited by collisions similarly to [O III] $\lambda 5007$ and are usually considered undeniable evidence of AGN ionization (e.g., Korista & Ferland 1989). Their presence in low-massive metal-poor galaxies optical (and IR) spectra is a current intensively discussed issue in the hunt to reveal intermediate-mass black holes (e.g., Cann et al. 2020; 2021; Molina et al. 2021).

After a careful analysis of our spectra, we exclude the presence of these lines (i.e., [Fe VI] $\lambda 5146$, [Fe XIV] $\lambda 5303$, [Fe VII] $\lambda 5721$, [Fe VII] $\lambda 6087$, [Fe X] $\lambda 6374$) in the optical spectra we analyzed¹⁵. In the upper panel of Fig. 1, next to [O I] $\lambda 6364$ there is a “bump” that could be in-

terpreted as a tentative [Fe X] $\lambda 6374$. However, this feature is more consistent with the Si II $\lambda 6371$ (actually a multiplet, Si II $\lambda\lambda 6348,71$), previously identified in some CLASSY galaxies in high-resolution optical spectra (e.g., VLT/GIRAFFE SBS 0335-052 E spectrum, Izotov et al. 2006). These permitted Si II lines may have a fluorescent origin and be produced by absorption of the intense UV radiation (Grandi 1976; Izotov et al. 2001). The detection of very high-ionization emission lines could be an alternative channel to identify hidden AGN activity in dwarf galaxies, especially in the JWST era with rest-frame IR coverage (e.g., Cann et al. 2018). However, here we want to highlight that it can be easy to misidentify [Fe X] $\lambda 6374$ and Si II $\lambda 6371$ (see also Herenz et al. 2023).

In conclusion, we stress that none of our galaxies are uniformly classified as non-SF dominated by *all* the optical diagnostics considered here. According to the classical BPT diagrams with the standard separators, few galaxies are classified as Comp/AGN as shown in Tab. 2, but never consistently, while they are all classified as SF dominated using the separators from X18, thus taking into account the gas-phase metallicity of each object (Sec. 4.1 and Fig. 2). Only two objects (J0944+3442, classified as SF by all the other diagrams, and again J0808+3948; both without UV lines) fall in the non-SF locus according to the oxygen line ratios used as shock diagnostics (Sec. 4.2 and Fig. 3), ruling out shock dominated emission. Finally, the absence or very weak He II $\lambda 4686$ lines is another strong indication of the lack of a harder mechanism than SF, with all the galaxies but J0808+3948 (with trans-solar metallicity and no UV lines) classified as SF dominated according to the Shirazi&Brinchmann diagram (Sec. 4.3 and Fig. 4).

5. UV DIAGNOSTIC DIAGRAMS

In the previous section, we showed how all the CLASSY galaxies characterized by UV emission lines are dominated by star formation, using different optical criteria, highlighting all their caveats. Further confirmation of their SF-dominated nature lies in the lack of N V $\lambda\lambda 1239,1243$ doublet in emission. Indeed in the UV, an unequivocal signature of AGN activity is generally represented by this very high-ionization emission doublet ($E > 77.5$ eV; Feltre et al. 2016). We do not observe the ISM N V doublet in emission in any of the CLASSY galaxies, but only in P-Cygni shape - strongly indicating the presence of massive stars (e.g., Chisholm et al. 2019). Having said that, here we want to explore if UV diagnostic diagram classification can be consistent with the optical and thus identify the best-observed UV diagnostics to discriminate SF from AGN and shock ionization. Of course, without AGN within the sample, we are unable to assess the ability of UV diagnostics to correctly classify AGN, but we

¹⁵ J0944-0038 MUSE data recently presented in del Valle-Espinosa et al. (2022) reveal [Fe VI] $\lambda 5146$ line in the brightest star-formation knot, only partly covered by the SDSS and LBT data that we took into account.

are able to test whether SF galaxies are incorrectly classified as AGN. We do this by comparing our sample of CLASSY galaxies with G16 constant and X18 BPASS bursty SF models, AM19 shock models and F16 AGN models presented in Sec. 3 and Tab. 1. Furthermore, in App. C.1, we show and discuss G16 single-bursts and B17 models, also introduced in Sec. 3 and Tab. 1. As we introduced in Sec. 1, UV diagnostics can be crucial to investigate ISM properties with JWST observations in objects above $z \sim 6$, and thus it is important to understand in detail their strengths and drawbacks.

Specifically, in the following subsections, we show the UV diagnostic plots that we found more promising among those proposed in the literature on the basis of models and simulations (Jaskot & Ravindranath 2016; Feltre et al. 2016; Nakajima et al. 2018; Hirschmann et al. 2019; 2022):

- C3He2-C4He2 (Fig. 5): C III] $\lambda\lambda 1907,9$ /He II $\lambda 1640$ vs C IV $\lambda\lambda 1548,51$ /He II $\lambda 1640$;
- C3He2-O3He2 (Fig. 6): C III] $\lambda\lambda 1907,9$ /He II $\lambda 1640$ versus O III] $\lambda 1666$ /He II $\lambda 1640$;
- C4C3He2-C4C3 (Fig. 7): C IV $\lambda\lambda 1548,51$ /C III] $\lambda\lambda 1907,9$ versus (C IV+C III])/He II $\lambda 1640$;
- EWC4 and EWC3 (Fig. 8): EW(C IV) and EW(C III]) versus C III]/He II $\lambda 1640$.

We also report in App. C.2 the diagnostics diagrams C III]/He II $\lambda 1640$ versus O III] $\lambda 1666$ /C III] $\lambda\lambda 1907,9$ (C3He2-O3C3) and C III]/He II $\lambda 1640$ versus C IV $\lambda\lambda 1548,51$ /C III] $\lambda\lambda 1907,9$ (C3He2-C4C3). Here we highlight that C IV and He II lines are broadly used in these diagrams, but they can have both a nebular and stellar contribution. We discuss this caveat in detail in Sec. 6.2.

As a general note about the AM19 shock grids, in all the following plots they are often completely overlapped in terms of velocity and magnetic field and gas-phase metallicity, but we decided to show the entire range of the v and B parameter space at three representative values of metallicity ($Z = 0.05, 0.5, 1 Z_{\odot}$) for completeness. These grids also cover very narrow regions in C4He2 space that correspond to the lowest velocities in the parameter space ($v < 200$ km/s, seen as spike-shaped features in grid coverage).

5.1. C3He2-C4He2

Fig. 5 shows the C III] $\lambda\lambda 1907,9$ /He II $\lambda 1640$ versus the C IV $\lambda\lambda 1548,51$ /He II $\lambda 1640$ diagnostic diagram (C3He2-C4He2) with previously described SF, shock and AGN grid models overlaid (see caption for details). This diagnostic diagram was first proposed as a good AGN and star-forming galaxies separator in F16. Jaskot & Ravindranath (2016) further supported this as a good diagnostic plot to discriminate between shocks and pure SF, where their

pure photoionization models lie above the shaded gray region in Fig. 5, while most of their models with a shock contribution of $\geq 10\%$ and $\geq 50\%$ to the shown line ratios fall within and below the gray shaded region, respectively. Indeed, the He II $\lambda 1640$ line can be enhanced by hard ionizing radiation with high-energy photons (> 54.4 eV), which can be produced by either AGN or shocks, causing a decrement of C III] $\lambda\lambda 1907,9$ /He II $\lambda 1640$ and C IV $\lambda\lambda 1548,51$ /He II $\lambda 1640$. This also implies that the C3He2-C4He2 diagram cannot clearly distinguish between AGN and shocks. Indeed, looking at the bottom panels of Fig. 5, shock and AGN grids cover a similar C III]/He II vs C IV/He II parameter space, with the most metal-poor shock grids reaching C III]/He II and C IV/He II down to ~ -1.75 and ~ -2.5 , respectively, as the $\alpha = -1.2$ AGN models (hardest AGN radiation) at the lowest values of metallicity and ionization parameter. Indeed, the strength of C III] and C IV is known to drop at decreasing metallicity ($12+\log(\text{O}/\text{H}) \lesssim 7.5$; e.g., Jaskot & Ravindranath 2016; see also Paper IV) and decreasing C/O. We also notice that the AM19 shock models shown in Fig. 5 can reach higher values than F16 AGN models in terms of C III]/He II line ratios, going beyond the gray shaded SF-shock separator region at low values of velocities ($v < 200$ km/s, spike-shaped feature in the shown grids; see also Jaskot & Ravindranath 2016 Sec. 4.4).

The scatter plots in Fig. 5, color-coded as reported in the color bar labels, show the 9 galaxies of our sample with C IV $\lambda\lambda 1548,51$ in pure emission (the other galaxies show pure absorption or P-Cygni profiles). In particular, SBS 0335-052 E (J0337-0502) and IZw 18 (J0934+5514) are located in the gray shaded region that separates the pure-SF and shock locii according to Jaskot & Ravindranath (2016). Moreover, the two objects partially overlap with the F16 AGN models. However, from the optical diagnostics, we know that these galaxies are SF-dominated (Sec. 4). Interestingly, these objects are the two lowest metallicity galaxies of the sample showing UV emission lines ($12+\log(\text{O}/\text{H}) \sim 7.46$ and ~ 6.98 , respectively) with also the lowest C/O abundances ($(\text{C}/\text{O})/(\text{C}/\text{O})_{\odot} \sim 0.26$ and ~ 0.12 , respectively). This means that the Jaskot & Ravindranath (2016) criterion can fail in classifying extremely metal-poor star-forming objects possibly characterized by very hard ionization and low C/O, which could mimic AGN or shock ionization (see also Maseda et al. 2017). In agreement with this, G16 SF models (both CST and SSP) can fall beyond the Jaskot & Ravindranath (2016) pure-SF line when considering low C/O (cyan grids have $(\text{C}/\text{O})/(\text{C}/\text{O})_{\odot}=0.1$), which would reduce C III] and C IV emission. Another factor that pushes the G16 SF models below the Jaskot & Ravindranath (2016) pure-SF locus is a higher IMF upper-cut ($M_{up} = 300 M_{\odot}$ instead of $M_{up} = 100 M_{\odot}$, dashed and solid lines, respectively), which would imply more massive stars, hence a harder ionization

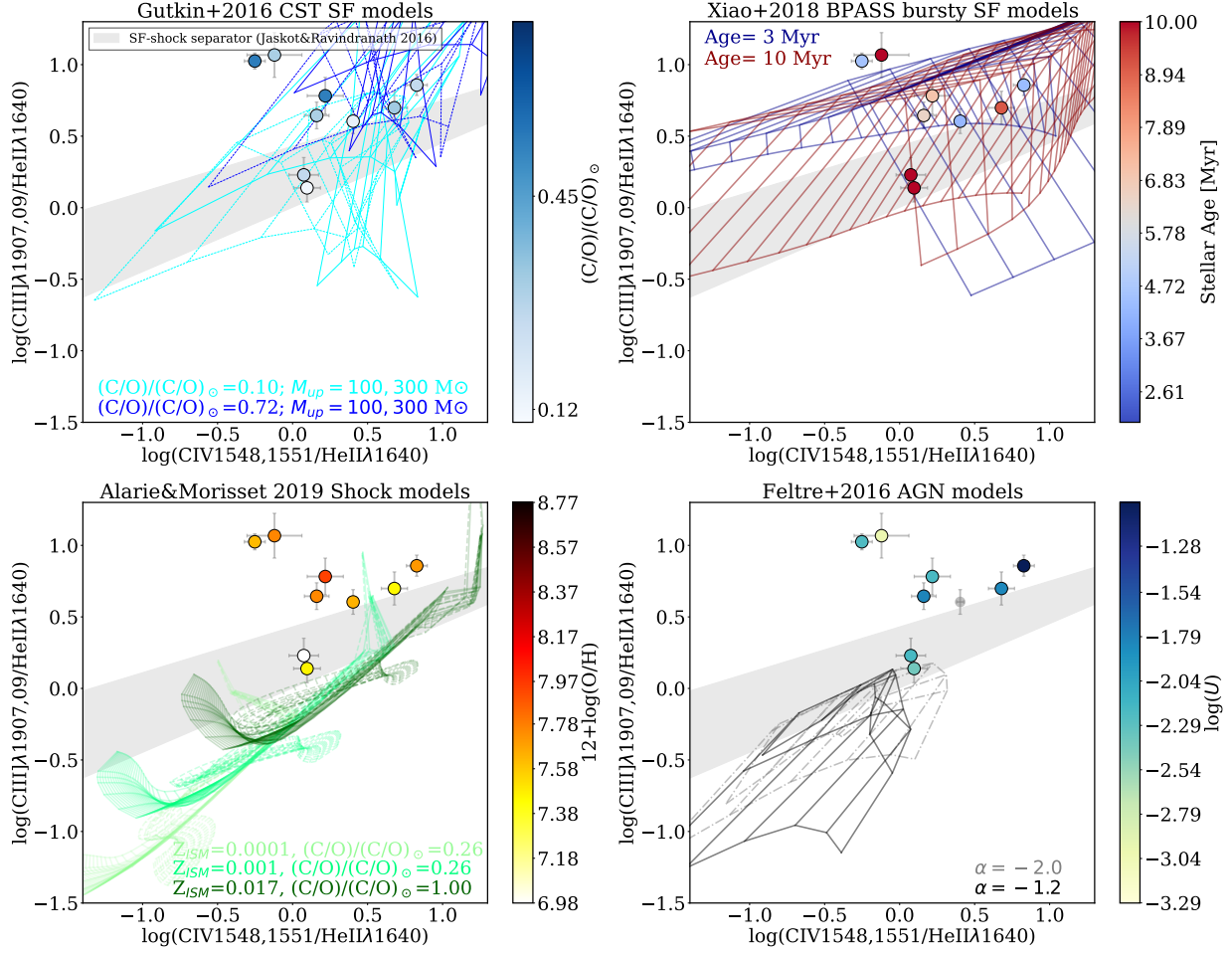


Figure 5. C3He2-C4He2 diagram: C III] $\lambda\lambda 1907,9/\text{He II } \lambda 1640$ vs C IV $\lambda\lambda 1549,51/\text{He II } \lambda 1640$ diagnostic plot (F16, Jaskot & Ravindranath 2016) to separate SF and AGN activities. Here we show only the CLASSY galaxies with C IV detected in pure emission. The gray shaded region represents the separator proposed by Jaskot & Ravindranath (2016) between pure-SF models (located above) and models with $\geq 50\%$ shock contribution (located below). Upper left panel: G16 models with continuous SF are shown in light ((C/O)/(C/O) $_{\odot}$ =0.1) and dark blue ((C/O)/(C/O) $_{\odot}$ =0.72), with the scatter plot color-coded as a function of the (C/O)/(C/O) $_{\odot}$ measured for the sample. The solid and dashed grids refer to different IMF cut ($M_{up} = 100 M_{\odot}$ and $M_{up} = 300 M_{\odot}$, respectively). Upper right panel: X18 models with burst of SF at 3 Myr and 10 Myr are shown in blue and red, respectively, with the scatter plot color-coded as a function of the stellar age derived from the UV stellar component fitting. Lower left panel: AM19 shock models with increasing metallicities from light to dark green, as shown in the legend, and (C/O)/(C/O) $_{\odot} = 0.26$ are shown on a scatter plot color-coded as a function of the gas-phase metallicity $12+\log(\text{O}/\text{H})$ (darker green means higher metallicity, up to the trans-solar value of $Z_{ISM} = 0.017$). Lower right panel: F16 AGN models with $\alpha = -2$ (solid - softer ionization) and $\alpha = -1.2$ (dash-dotted - harder ionization) overplotted on a scatter plot color-coded as a function of the ionization parameter $\log(U)$. The two galaxies located in the gray-shaded region are IZw 18 and SBS 0335-052 E, which have the lowest $12+\log(\text{O}/\text{H})$ and C/O abundance in the sample. Overall, the C3He2-C4He2 diagram can be used to discriminate SF from AGN and shocks, with some caveats. Shocks and AGN are harder to discriminate, but still the former are expected to have higher carbon-to-helium line-ratios, especially at increasing metallicity.

field (i.e., higher He II emission). Concerning G16 single-burst SF grids (that we do not show for clarity reasons but see Fig. 13), only ages younger than ~ 4 Myr can reproduce the line ratios observed for the CLASSY galaxies. Since the G16 models do not take into account either stellar rotation or binary interactions (which would amplify the galaxies ionizing fluxes for several Myr after a SF burst), the ionizing photons drop at older ages than 4 Myr, with subsequent reduction of He II (but also C III] and C IV), inducing a shift of the grids

to higher C III]/He II and C IV/He II than the range shown in Fig. 5 (see App. C.1 and e.g., Jaskot & Ravindranath 2016 Sec. 3.1 for a detailed comparison between different model prescriptions). In BPASS models instead the stellar multiplicity impacts the duration of the ionizing photon production (as well as in B17 models that take into account stellar rotation; see Fig. 13). Indeed, both the BPASS 3 Myr and 10 Myr star-forming grids of X18 can fully cover the CLASSY data

and the SF locus in Fig. 5, only slightly overlapping with the AM19 shock models.

Overall, to explain the locations of galaxies such as SBS 0335-052 E and IZw 18, lying in the region separating SF from harder mechanisms, the most likely explanation is their low O/H and C/O abundances (see also Wofford et al. 2021 for SBS 0335-052 E). Hence, before using the C3He2-C4He2 diagram the user should be mindful of the metallicity and C/O abundance of the targets, in that ionization sources in low-metallicity objects are less easily distinguishable for this diagnostic.

5.2. C3He2-O3He2

In Fig. 6 we show the C III] $\lambda\lambda 1907,9$ /He II $\lambda 1640$ versus O III] $\lambda 1666$ /He II $\lambda 1640$ diagnostic diagram, proposed by F16 and further explored by Hirschmann et al. (2022). In contrast to the C3He2-C4He2 diagram shown in Fig. 5, C3He2-O3He2 in Fig. 6 can separate all of the three contributions of SF, AGN, and shocks quite well. This is with the exception of the G16 SF models with either low C/O or high M_{up} (both with constant and bursty SF) which, again, cover the entirety of the parameter space (see Sec. 5.1), as we further comment below. Most importantly, AGN and shock grids are only slightly overlapped, considering sub-solar metallicities (considering $(C/O)/(C/O)_{\odot} = 0.26$), with shock models showing higher O III]/He II line ratios than AGN grids. Instead, the dark-green grid at trans-solar metallicity ($Z_{ISM} = 0.017$; $(C/O)/(C/O)_{\odot} = 1$) shifts to higher C III]/He II, overlapping more with the AGN and SF grids. In particular, He II emission is expected to increase in both AGN and shock models, as already discussed in Sec. 5.1, explaining the shift of AGN and shocks to lower C III]/He II and O III]/He II than SF grids (but $v < 200$ km/s shock models - spike-shaped in the shown grids - can reach C III]/He II comparable to SF grids as in Fig. 5). However, shocks are expected also to have an increase of C III], which generally tightly correlates with temperature-sensitive lines such as O III] $\lambda 1666$ (see e.g., Jaskot & Ravindranath 2016 Fig. 12 and 9). This could explain the higher [O III]/He II for shocks than AGN models. As a reference, in Fig. 6 we added a dashed green line to separate shock models from the SF locus

$$y = 0.8x + 0.2 \quad (3)$$

and a horizontal dash-dotted line to separate AGN models from the SF locus

$$y = 0.1 \quad \text{and} \quad -1.8 < x < -0.15 \quad (4)$$

with $x = \log(\text{O III] } \lambda 1666/\text{He II } \lambda 1640)$ and $y = \log(\text{C III] } \lambda\lambda 1907,9/\text{He II } \lambda 1640)$. The AGN grids again extend beyond the shown x- and y-ranges, with $\log(\text{O III]/He II})$ and $\log(\text{C III]/He II})$ down to ~ -1.5 and

~ -2.5 , respectively, at the highest values of metallicity and lowest of ionization parameter.

The scatter plot in Fig. 6 shows the 19 CLASSY galaxies with all the involved UV emission lines with $S/N > 3$. Interestingly, the parameter space covered by the CLASSY galaxies in this diagnostic diagram is very similar to that of the $z \sim 2-4$ galaxies of Nanayakkara et al. (2019), which further supports the classification of these systems as analogues to high- z SF-galaxies. As in Fig. 5, G16 SF models cover the majority of the C3He2-O3He2 plane. We notice that grids with low C/O abundances (solid and dashed cyan G16 grids in the upper left panel) are shifted to lower C III]/He II and higher O III]/He II (trend in agreement with the C/O color-coding shown in Fig. 6 upper left-hand panel). This is probably due to the fact that carbon is a key coolant in the nebula, and thus a lower C/O ratio raises the electron temperature – as commented in Jaskot & Ravindranath (2016), and demonstrated by the decrease in metallicity (which is color-coded in the bottom left-hand panel) as O3He2 increases. Hence, the increased collisional excitation rate partially compensates for the reduced C abundance, preventing an extreme drop of the C III]/He II ratio, and possibly enhancing [O III] $\lambda 1666$. As a result, the low C/O G16 grids (solid and dashed cyan, according to the different IMF cut) manage to cover the lowest C III]/He II and O III]/He II SBS 0335-052 E and IZw 18. X18 BPASS models instead are more confined in the SF locus, with the lowest metallicity and ionization parameter points of the grid slightly covering the region that we define as the AGN locus (below the black dash-dot line and above the dashed black line in Fig. 6).

Also Hirschmann et al. (2019) proposed line separators to classify the main ionization mechanisms for the C3He2-O3He2 diagnostic plot, obtained from synthetic emission line ratios computed by coupling G16 and F16 models with high-resolution cosmological zoom-in simulations of massive galaxies. However, according to Hirschmann et al. (2019) AGN-Composite and Composite-SF separators (that we do not report in Fig. 6 for clarity reasons), all the CLASSY galaxies would be classified as composite. Hirschmann et al. (2019) also compared their simulated galaxies with observations of AGN and star-forming galaxies, finding generally good agreement with their classification. However, the local and high- z low-metallicity galaxies that they overplotted to their diagnostic diagrams ended up in the composite region as well. Hence, we conclude that the Hirschmann et al. (2019) composite region also hosts star-forming galaxies with more “extreme” high- z characteristics that are typical of our sample.

Overall, we conclude that C3He2-O3He2 represents a better diagnostic diagram than C3He2-C4He2, since it is able to clearly separate (up to solar metallicities) the different mechanisms, with AGN showing lower O III]/He II than shocks,

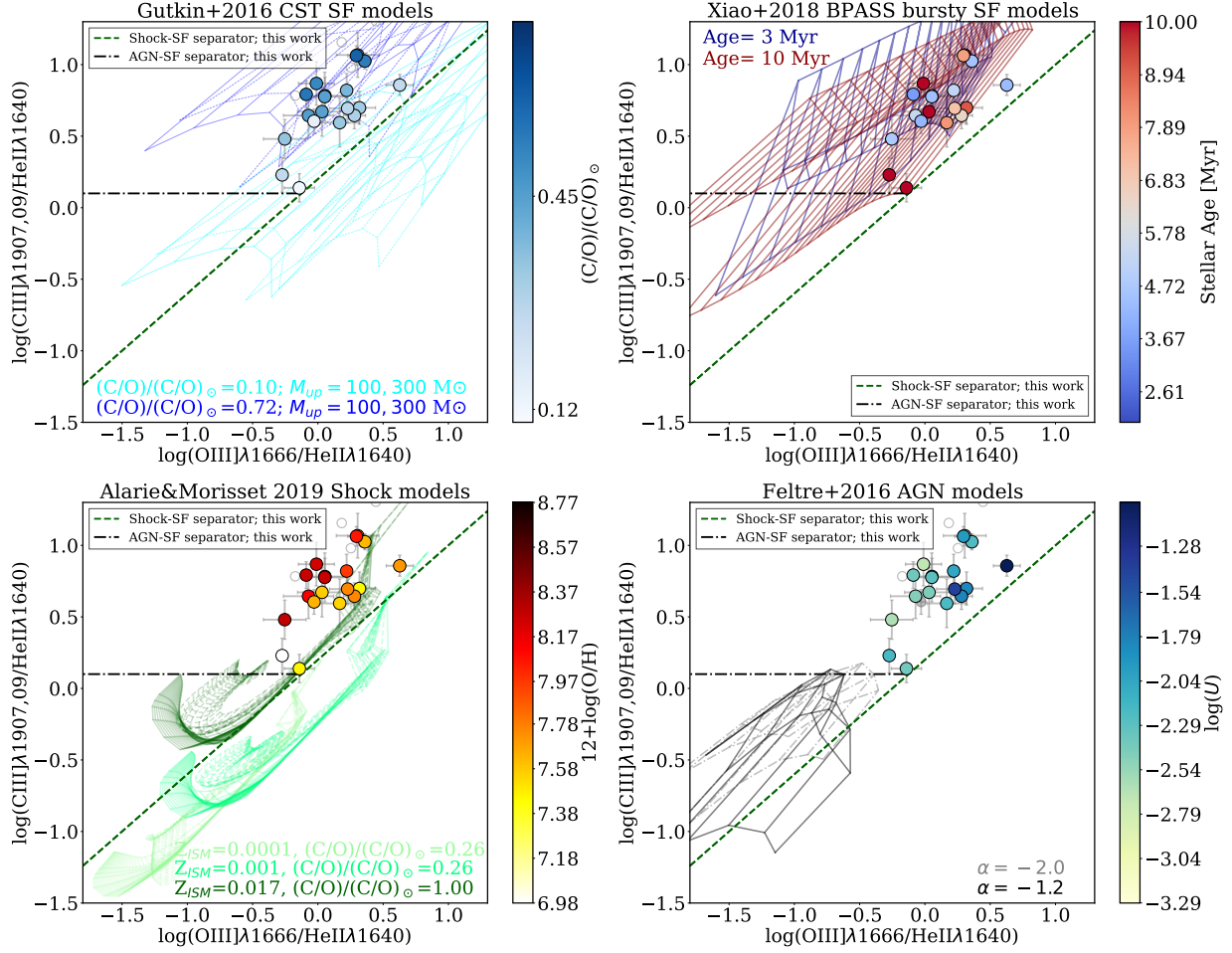


Figure 6. C3He2-O3He2 diagram: C III] $\lambda 1907,9/\text{He II } \lambda 1640$ versus O III] $\lambda 1666/\text{He II } \lambda 1640$ diagnostic diagram, proposed by F16. The filled and open dots show $S/N > 3$ and $S/N < 3$ fluxes for all the emission lines taken into account, respectively. The models superimposed are as explained in Fig. 5. Overall, this represents the best diagram to discriminate SF, AGN and shocks at sub-solar metallicities (i.e., excluding the dark-green shock grid), due to the minimal overlap between each set of grids and the fact that all CLASSY galaxies are correctly classified as star-forming, as shown by the dashed green and dash-dotted lines to separate shock and AGN models from the SF locus (Eq. 3 and Eq. 4), respectively.

while SF dominated emission shows higher C III]/He II. Moreover, all the CLASSY galaxies, even the most metal-poor SBS 0335-052 E and IZw 18, are covered by the SF grids and do not overlap with the AGN or shock grids.

5.3. C4C3He2-C4C3, EWC4, and EWC3

Fig. 7 shows the $(\text{C IV} + \text{C III})/\text{He II}$ vs $\text{C IV}/\text{C III}]$ diagnostic plot proposed by Nakajima et al. (2018), with their proposed AGN locus shown in shaded gray. As in Fig. 5, SBS 0335-052 E and IZw 18 end up in the AGN locus, overlapping slightly with the F16 AGN models. Analogously to what we commented in Sec. 5.1, their shift can be explained in terms of their low $12 + \log(\text{O}/\text{H})$ and low C/O abundance. In this figure, it is even clearer that only the G16 SF models (both CST and SSP) with low C/O (cyan grids) can cover this sub-set of CLASSY galaxies, excluding two outliers. A higher C/O abundance grid with a high-cut in

the IMF (dashed blue grids) lies close but does not cover the lowest $(\text{C IV} + \text{C III})/\text{He II}$ line ratios, while the higher C/O abundance grid with $M_{up} = 100 M_{\odot}$ (solid blue grids) does not cover the CLASSY galaxies. Overall, an increase of C/O quickly pushes the G16 grids (also the bursty SF grids at ages below 4 Myr; see Fig. 13) toward values of $(\text{C IV} + \text{C III})/\text{He II}$ higher than what we typically observe in our sample. X18 BPASS models (as well as B17; see Fig. 13) can well reproduce the observed CLASSY line ratios, with the 3 Myr grids confined in the Nakajima et al. (2018) SF locus and the 10 Myr grids slightly shifted on the grey shaded area of Fig. 7, reaching the lowest values of $(\text{C IV} + \text{C III})/\text{He II}$ at decreasing metallicity and ionization parameter. Moreover, AGN and shock grids are almost entirely overlapped (apart from the most metal-poor shock models, characterized by the lowest $(\text{C IV} + \text{C III})/\text{He II}$).

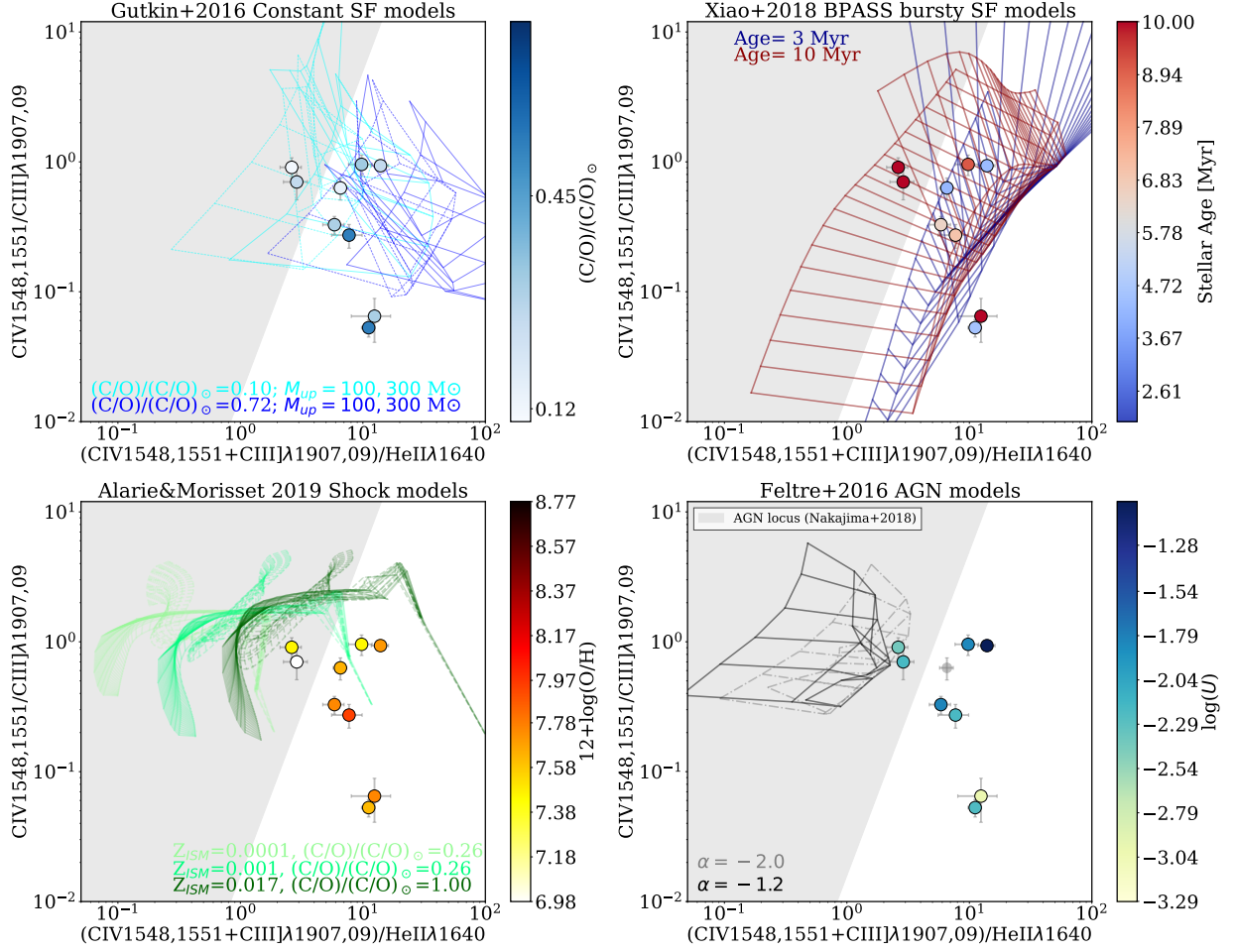


Figure 7. C4C3He2-C4C3 diagram: $(\text{C IV } \lambda\lambda 1548,51 + \text{C III] } \lambda\lambda 1907,9) / \text{He II } \lambda 1640$ vs $\text{C IV} / \text{C III]}$ diagnostic plot proposed by Nakajima et al. (2018) to separate SF and AGN activities, with their proposed AGN-dominated region highlighted in shaded gray. The models superimposed are as explained in Fig. 5. Similarly to Fig. 5, this plot can be used to separate SF from AGN with some caveat. Indeed, the two galaxies which end up in the AGN locus are again I Zw 18 and SBS 0335-052 E, the two lowest $12 + \log(\text{O}/\text{H})$ and C/O abundance galaxies of the CLASSY sample, and can be reproduced by the low C/O SF grids (in cyan).

Nakajima et al. (2018) proposed other two additional diagnostic plots to separate SF and AGN activities, shown in Fig. 8, with the CLASSY data color-coded as a function of the ionization parameter $\log(U)$. In particular, we notice that $\text{EW}(\text{C III]})$ and $\text{EW}(\text{C IV})$ increase at higher $\log(U)$, and also the C IV and C III] emissions are higher with respect to He II. This is clearer in the right panel since $\text{EW}(\text{C IV})$ provides a valid $\log(U)$ tracer as demonstrated in Paper IV. As in Fig. 7, the AGN regions according to Nakajima et al. (2018) criteria are shown in shaded gray. Nakajima et al. (2018) computed AGN photoionization models, assuming a continuum underneath the line emission dominated by the accretion disk, commenting that this is an overestimate since it does not take into account the effects of dust attenuation (i.e., presence of the torus). In general, evaluating the continuum emission to compute EWs in shock and AGN models implies many arbitrary assumptions, since the continuum can

have a composite nature, coming from both the stellar component and the additional ionizing sources as well as their intrinsic characteristics. For this reason F16 and AM19 do not provide EWs for their models. On the other hand, all the displayed CLASSY galaxies are in the SF-locus defined by Nakajima et al. (2018), with the exception of J0944-0038 in the left panel, characterized by $\text{EW}(\text{C III]}) \sim 33 \text{ \AA}$, which still lies in a region where both AGN and SF models could overlap. Also, X18 BPASS models can predict the observed range of C III] and C IV EWs only taking into account very young ages (1 Myr), which are shifted at higher C III]/He II and C IV/He II. Thus, it could be that the continuum to compute the EWs in these models is overestimated. Interestingly, the EW values predicted by G16 single-burst SF models with ages younger than 4 Myr cover the Nakajima et al. (2018) SF locus, and thus the $\text{EW}(\text{C III]})$ and $\text{EW}(\text{C IV})$ values observed for the CLASSY galaxies, while the constant

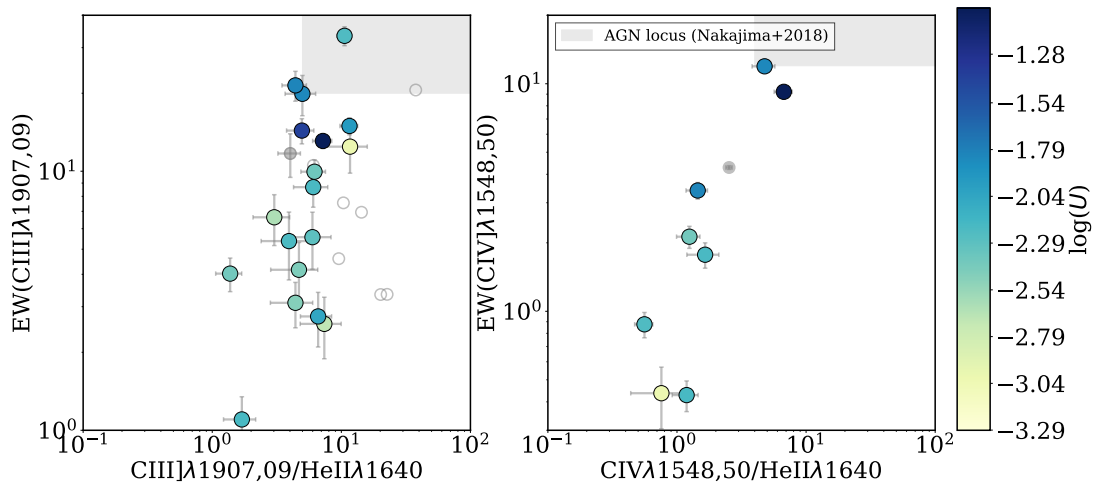


Figure 8. EW(C III)] and EW(C IV) diagnostic plots, where the gray shaded regions represent the Nakajima et al. (2018) AGN-locus, separated from the star formation locus. The filled and open dots show $S/N > 3$ and $S/N < 3$ fluxes for all the emission lines taken into account, respectively. Interestingly, this classification scheme works well for the CLASSY galaxies, even for the most metal-poor systems.

SF models hardly reproduce them. As commented also for Fig. 6, CLASSY galaxies fall entirely in the region defined as composite in Hirschmann et al. (2019), confirming that star-forming objects with the characteristics of the CLASSY sample (and thus high- z analogs) could risk being misclassified according to their criteria. Overall, these diagrams could be useful tools to classify even metal-poor star-forming galaxies, but since it is not trivial to evaluate the continuum to compute EWs in shock and AGN models, they cannot be used to separate AGN from shocks.

5.4. Summary

All the discussed UV diagnostic diagrams in the previous subsections, with some caveats, can distinguish SF from AGN and shocks, while it is possible to disentangle AGN from shocks only by taking into account C III], He II and O III] emission lines. Here we summarize our main findings:

- The C3He2-C4He2 diagram (Fig. 5) from Jaskot & Ravindranath (2016) can be used to discriminate SF from AGN and shocks. However, the users should be mindful of the metallicity and C/O abundance of the targets, in that ionization sources in low-metallicity objects are less easily distinguishable for this diagnostic. Shocks and AGN are harder to discriminate, but still the former are expected to have higher carbon-to-helium line-ratios than the latter, especially at increasing metallicity.
- C3He2-O3He2, proposed by F16, is the only diagram able to separate all the three ionization mechanisms at sub-solar metallicities (Fig. 6 and Eq. 3, 4). In this plot, all the CLASSY galaxies, even the objects characterized by the lowest $12+\log(O/H)$ and C/O (i.e.,

SBS 0335-052 E and IZw 18), are covered by the G16 SF models and do not overlap to the AGN or shock grids, that cover similar C III]/He II but different O III]/He II line ratios (lower for AGN, higher for shocks). Other diagnostic diagrams from F16 are C3He2-C3O3 and C3He2-C4C3 (App. B), with the former able to separate SF, AGN and shocks as C3He2-O3He2 (Eq. C1, C2), while the latter can only separate SF from AGN and shocks (Eq. C3, C4).

- The C4C3He2-C4C3 diagram (Fig. 7) from Nakajima et al. (2018) is a good diagnostic plot to separate SF and AGN, with the caveat of taking into account $12+\log(O/H)$ and C/O, similarly to C3He2-C4He2. However, it is not possible to distinguish between AGN and shocks, for which O3He2-C3He2 and C3He2-C3O3 would be better suited.
- Finally, EWC4-C3He2 and EWC3-C3He2 (Fig. 8) from Nakajima et al. (2018) provide as well good diagnostic plots to separate star-forming galaxies from objects characterized by non-photoionization mechanisms via the Nakajima et al. (2018) AGN-SF separator line. This diagnostic diagram holds true even at low metallicity, low C/O abundance and high $\log(U)$, but does not allow the user to discriminate shocks from AGN models, given the difficulties in estimating the corresponding EWs.

6. DISCUSSION

In Sections 4 and 5 we demonstrated that our galaxies are SF-dominated according to optical diagnostics, and then explored the most promising UV diagnostic diagrams, highlighting each of their strengths and weaknesses. In the fol-

lowing, we discuss the *practicality* of the UV diagnostic diagrams, in terms of the observability of UV emission lines shown in this work and possible caveats when using them as diagnostics, and conclude with a comment on UV emission lines currently observed with JWST at high- z . We do this for two reasons: (1) to provide guidance on whether or not these lines should be expected in proposed observations of certain targets and (2) to provide context on the properties of the target if the lines *are* detected in their observations. Indeed, UV emission lines are a powerful (and at increasing redshift also the only) tool to investigate ISM conditions in galaxies.

6.1. Conditions for UV emission in high- z analogues

In general, we confirmed that the main two conditions to have UV emission line detections in CLASSY (i.e., C IV $\lambda\lambda$ 1548,51, He II λ 1640, O III] $\lambda\lambda$ 1661,6, C III] $\lambda\lambda$ 1907,9) are low metallicity and high ionization parameter, traced by the [O III]/[O II] line ratio (but also [O III]/ $H\beta$). Indeed, we see no C III] $\lambda\lambda$ 1907,9 (and thus no other UV emission lines) in CLASSY galaxies with $12+\log(O/H) \gtrsim 8.3$. Specifically, we do not observe C III] in the eight CLASSY galaxies at metallicity higher than this threshold, where $EW(C\ III)] \lesssim 2 \text{ \AA}$ and $\log(U) \sim -2.9$. This is also the reason why C III]-emitting galaxies (highlighted by thick black edges in all the figures) are systematically shifted to lower $\log([N\ II]/H\alpha)$ ($\lesssim -1$) in Fig. 2 and Fig. 4), with the lowest metallicity targets ($12+\log(O/H) < 7.8$), having also higher $\log(He\ II\lambda 4686/H\beta)$ line ratios (~ -1.4 to -1.8). However, the trend between the EW of UV lines and metallicity is not linear because carbon lines in our galaxies can be suppressed at $12+\log(O/H) < 7.5$ (see e.g., Fig. 15 in Paper IV) and at decreasing C/O (Berg et al. in preparation). As such, low-metallicity is not a sufficient condition to ensure the presence of UV emission lines. In fact, there are nine CLASSY galaxies at $12+\log(O/H) < 8.3$ without UV emission lines. These objects also have median values of $EW(C\ III)] \lesssim 2 \text{ \AA}$ and $\log(U) \sim -2.8$. Indeed, the EW of UV lines slightly correlates with $\log(U)$ as well, with a significant decrease of detected UV lines at $\log(U) \lesssim -2.5$ for our sample. This is also visible from Fig. 2 and Fig. 3, in which C III]-emitters are clearly shifted to higher $\log([O\ III]/H\beta)$ ($\sim 0.5-1$) and higher $\log([O\ III]/[O\ II])$ ($\sim 0.5-1.5$). Overall, this finding is consistent to previous works in the nearby Universe (e.g., Heckman et al. 1998; Ravindranath et al. 2020), as well as at higher redshift (e.g., Shapley et al. 2003; Rigby et al. 2015; Du et al. 2017).

The physical reason why UV metal lines are mostly visible only at low metallicity is well-explained in Jaskot & Ravindranath (2016) (see their Sec. 3.2). In particular, a decrease in metallicity implies a harder stellar ionizing radiation and a higher temperature nebula, and thus a larger amount of ionizing photons and a larger collisional excita-

tion rate, respectively. Indeed, the UV metal lines are collisionally excited with energy levels above the ground state of $E/k \sim 6.5-8.3 \text{ eV} \sim 75,000-97,000 \text{ K}$, much higher than optical collisional lines that typically have $E/k \ll 70,000 \text{ K}$ (e.g., $\sim 7.5 \text{ eV} \sim 87,000 \text{ K}$ for O III] $\lambda\lambda$ 1661,6 versus $\sim 2.5 \text{ eV} \sim 30,000 \text{ K}$ for [O III] λ 5007 and $\sim 5.4 \text{ eV} \sim 62,000 \text{ K}$ for [O III] λ 4363; Osterbrock & Ferland 2006; Draine 2011). Specifically, C III] $\lambda\lambda$ 1907,9 (the brightest and most common) has the lowest $E/k \sim 75,000$, while the less common C IV $\lambda\lambda$ 1548,51 and N IV] $\lambda\lambda$ have the highest $E/k \sim 93,000-97,000 \text{ K}$. Hence, the UV lines are extremely temperature sensitive in photoionized gas that can reach $T \sim 2 \times 10^4 \text{ K}$ in our systems (see also Paper IV), compensating for the lower ionic relative abundances. As discussed in previous works (e.g., Jaskot & Ravindranath 2016), dust attenuation, density, SFR and stellar population characteristics (stellar age and metallicity) can also play a role in the presence or absence of these UV lines, but we find no clear correlations comparing the derived quantities for the CLASSY galaxies with their UV emission strengths.

6.2. Caveats in Using CIV and HeII

UV lines such as He II λ 1640 and C IV $\lambda\lambda$ 1548,51 can have both a stellar and nebular origin, with C IV being also a resonant line affected by radiation transfer effects (e.g., Steidel et al. 2016). For many CLASSY galaxies, we can confirm He II and C IV nebular origin thanks to the general consistency of their intrinsic velocity dispersion values with those of O III] $\lambda\lambda$ 1661,6 ($\sigma \sim 50 \text{ km/s}$; Fig. 1 bottom panel).

Concerning C IV, typical galaxies without an AGN show either C IV in absorption from the surrounding ISM or circumgalactic medium (CGM) gas or a P-Cygni profile from the stellar winds of massive stars (e.g., Leitherer et al. 2001). Nebular C IV emission is rarely observed in the literature, and comes uniquely from studies of systems with $12+\log(O/H) \lesssim 8$ and generally high ionization parameter $\log(U) \gtrsim -2.5$ (see Fig. 16 in Paper IV), probably tracing a rapid hardening of the ionizing spectrum at low metallicities (see also Senchyna et al. 2019; Berg et al. 2021; Senchyna et al. 2023a; Schaerer et al. 2022). From a visual inspection of C IV feature, we classified the CLASSY galaxies as being either C IV emitters (9 objects), P-Cygni (10), without C IV coverage (3), and defining the remaining others as ISM absorbers (23). Specifically, we applied the classification after normalizing for the stellar component, thus we are considering only the ISM contribution of C IV doublet. We then calculated the $EW(C\ IV)$ by integrating the C IV emission in a $\sim 10 \text{ \AA}$ window centered on the C IV lines, and the continuum in two featureless $\sim 5 \text{ \AA}$ windows on each side. We show the results of this exercise in Fig. 9, where we color-code the CLASSY mass-metallicity relation as a function of $EW(C\ IV)$. Also, galaxies with different C IV profiles are indicated using different

symbols, as listed in the legend. Hence, within the CLASSY sample, C IV emitters (but also P-Cygni) are found to be more metal-poor and low-mass ($12+\log(\text{O}/\text{H}) \lesssim 8, 8.25$ and $\log(M^*/M_\odot) \lesssim 8, 9$, respectively). It should be noted here, that the P-Cygni profiles here are very narrow and non-stellar (i.e., the stellar component has been subtracted) and should not be confused with the strong stellar P-Cygni profiles seen at high-metallicity. Also, C IV absorbers within the CLASSY sample have increasing EWs at larger stellar masses and metallicities. We do not find further particular correlations with other gas and stellar properties (e.g., SFR, E(B-V), density). Of course, these inferences are being drawn from our local sample of high- z analogues and may not hold true at all redshifts. Finally, we highlight that C IV is a resonant transition, meaning that high-ionization gas can scatter the photons. As discussed in Berg et al. (2019), resonantly scattered C IV emission appears broader than non-resonant emission lines (e.g., O III] $\lambda 1666$) and double-peaked, as it is usually found in Ly α studies (e.g., Hayes 2015; Verhamme et al. 2017; see also CLASSY Paper VII). In particular, Berg et al. (2019) confirmed this C IV resonant emission in two CLASSY galaxies, J1044+0353 and J1418+2102, which are the two objects that show the largest difference between C IV and O III] widths. The other CLASSY galaxies showing C IV in emission do not show the clearly double-peaked signatures (see Fig. 2 in Paper IV) and have consistent values of $\sigma(\text{C IV})$ and $\sigma(\text{O III])}$.

Overall, given the complex nature of the C IV nebular emission (see also Sec. 6.4.1. of Paper IV), diagnostic diagrams involving the C IV lines (i.e., C IV/He II and C IV/C III] line ratios, as well as EW(C IV)) should be used with caution. The complexity of this line is also evident in the velocity offset that we find for C IV lines, in that they are systematically redshifted by $\sim 25 - 100$ km/s with respect to the other UV lines (see Fig. 11 in App. A), also seen in Berg et al. (2019); Wofford et al. (2021); Senchyna et al. (2023a), which could be consistent with resonance lines in an outflowing medium. Indeed, we found that to properly fit the C IV lines, we have to employ a different value of their velocity¹⁶ (and thus line center) with respect to He II and O III]. However, in order to fully explore and compare in detail the different line kinematics, we would need integral-field spectroscopy data in the UV to see how the spectra change as a function of the location within the galaxy.

Moving to He II $\lambda 1640$ instead, its stellar contribution can be due to massive and very massive stars, including O-type stars and WRs, as commented in Sec. 1. A typical signature of stellar He II is a very broad width (e.g., Sixtos et al.

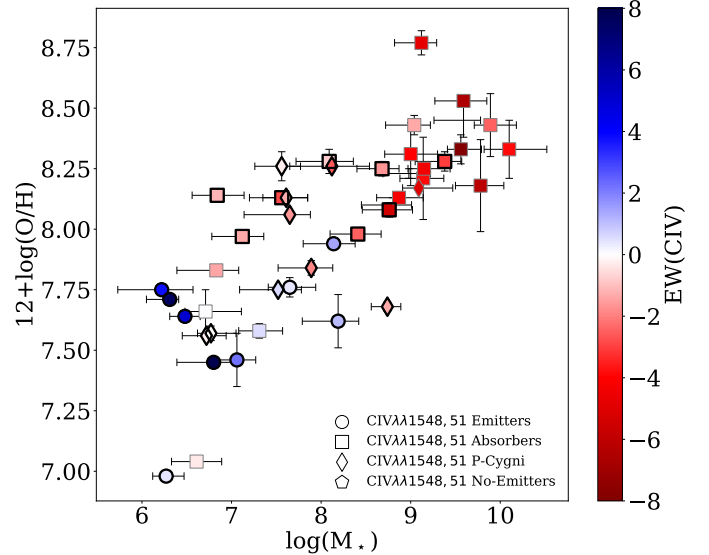


Figure 9. Mass-metallicity relation for CLASSY galaxies with C IV in emission (dots), absorption (squares) and P-Cygni (diamonds), color-coded by EW(C IV), with red and blue values indicating negative (lines in absorption) and positive (lines in emission) EWs, respectively. The galaxies with at least one UV emission line (i.e., C III] are highlighted by a black thick edge. These plots show that galaxies which are C IV emitters, or with narrow P-Cygni non-stellar profiles, tend to have lower metallicities ($12+\log(\text{O}/\text{H}) \lesssim 8, 8.2$) and lower stellar masses ($\log(M^*/M_\odot) \lesssim 8, 9$).

2023; Wofford et al. 2023; Smith et al. 2023), that can be distinguished from nebular emission via a comparison with close emission lines not affected by stellar contamination (i.e., O III] $\lambda \lambda 1661, 6$). The contribution of WR stars is more evident in optical spectra, where the He II $\lambda 4686$ line can be blended with several metal lines in the so-called “blue-bump” (Brinchmann et al. 2008). As discussed in Sec. 3.1.1 of Paper IV, our stellar component fitting accounts for different prescriptions for the evolution and atmospheres of massive stars, better accounting for He II stellar contribution than other modeling prescriptions (e.g., Senchyna et al. 2021). The best example is Mrk 996 (J0127-0619) shown in Fig. 10, which hosts a significant WR population (James et al. 2009) and a broad He II $\lambda 1640$ feature ($\sigma > 100$ km/s), that is completely stellar according to the C&B stellar component fit (blue dashed line), without signs of nebular emission. Only four CLASSY galaxies (i.e., J1129+2034, J1253-0312, J1200+1343, J1314+3452; see Fig. 22 of Paper IV) have $S/N(\text{He II}) > 3$ and $\sigma(\text{He II}) > 100$ km/s (up to 200 km/s and broader than $\sigma(\text{O III])1666$), indicating that a stellar contribution can still be present despite our subtraction of the stellar-component emission. After a visual inspection of their optical spectra, all these four galaxies show the presence of the WR blue-bump.

¹⁶ C IV lines were fit separately from the other UV lines, as explained in Paper IV Sec. 3.2.

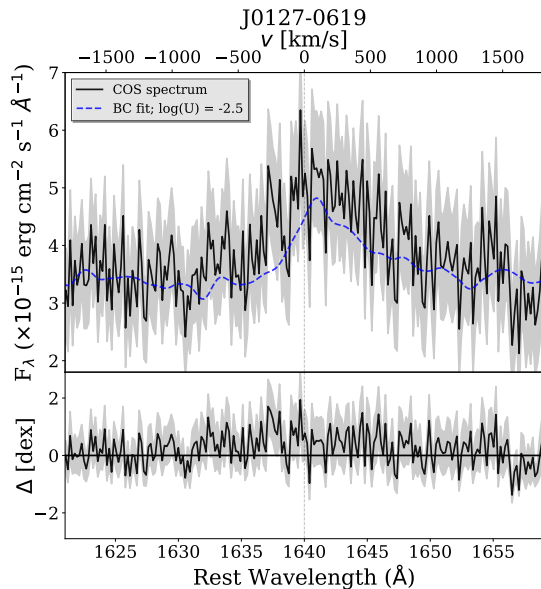


Figure 10. The He II $\lambda 1640$ feature of Mrk 996 (J0127-0619) superimposed with the stellar component best-fit made with C&B (blue dashed line) described in detail in Sec. 3.1.1 of Paper IV. The bottom panel shows the difference between the observed spectrum and the C&B model. The very broad He II component ($\sigma > 100$ km/s) has a stellar origin, in contrast to the nebular He II emission that we generally observe in other CLASSY galaxies ($\sigma \sim 50$ km/s; see Fig 1 of this paper and also Fig. 22 of Paper IV). This figure aims to illustrate the broad stellar He II profile and guide the user in its identification.

Overall, we acknowledge that He II $\lambda 1640$ (both for its stellar/nebular origin and high ionization potential) can be also problematic to reproduce by photoionization models (e.g., Gutkin et al. 2016; Steidel et al. 2016; Nanayakkara et al. 2019). This led some authors (e.g., Hirschmann et al. 2019; Feltre et al. 2016) to propose UV diagnostic diagrams without He II, comparing C IV $\lambda \lambda 1549, 51$ and C III] $\lambda \lambda 1907, 9$ with other UV lines, such as N V $\lambda \lambda 1239, 1243$, N IV] $\lambda \lambda 1483, 87$ and N III] $\lambda \lambda 1747-54$, or optical lines like [O III] $\lambda 5007$ and [O I] $\lambda 6300$ (that can be a good low metallicity AGN and shock diagnostic, Sec. 4.1, 4.2). However, as shown in Paper IV, these UV lines, as well as Si III] $\lambda \lambda 1893, 92$, are very faint and observable in a handful of objects, while it is difficult to have extended coverage from the UV up to the very faint [O I] $\lambda 6300$. This is the reason why we have not explored further UV diagnostic diagrams in this paper.

To conclude, we want to highlight the advantages of detecting O III] $\lambda \lambda 1661, 6$ in UV spectra. As discussed in Paper IV, O III] is an auroral line like [O III] $\lambda 4363$ and is thus sensitive to the gas temperature. It can be used to estimate C/O (see Sec. 2.1) and is more sensitive to shocks than carbon lines (Fig. 6). Finally, the proximity of O III] to C IV

and He II lines in UV spectra is useful for comparisons of the corresponding line widths, to understand if the C IV and He II emission is purely nebular, as discussed in this subsection.

6.3. Current Observations of UV Emission Lines at High- z

The UV diagnostics presented in this work and in CLASSY Paper IV can provide informative guidelines for interpreting high- z spectra. Such guidelines are especially important now that JWST has pushed the UV spectroscopic frontier to higher redshifts than ever before. Currently, large and deep JWST surveys, such as JADES, CEERS, and GLASS (e.g., Bagley et al. 2023; Bunker et al. 2023b; Treu et al. 2022), have started to provide statistically significant galaxy samples for studying galaxy evolution from $z \sim 1$ till the epoch of reionization (up to $z \sim 13$). Up to now, the furthest spectroscopically confirmed galaxy is among the four young, metal-poor (stellar metallicity $\log(Z/Z_{\odot}) \sim -1.91 - -0.18$), low-mass ($M \sim 10^7 - 10^8 M_{\odot}$) systems at $10.3 < z < 13.2$ presented in Curtis-Lake et al. (2023). Their redshifts were estimated using the Lyman-break as a reference, because of the complete lack of both UV and optical emission lines. Indeed, so far, there has been a deficit in the amount of UV emission lines measured in the epoch of reionization. Despite becoming visible when stacking NIRSpec/prism spectra (using 38 JADES targets at $5 < z < 8$, priv. comm.), UV lines are detected in $\lesssim 4\%$ objects in the latest JADES data release (Bunker et al. 2023b). This is puzzling given that pre-JWST ground-based rest-frame optical observations proved that galaxies at $z \sim 5 - 7$ show prominent high-ionization nebular emission UV lines due to their extreme radiation fields and low metallicity (e.g., Stark et al. 2015; Mainali et al. 2017; 2018). The lack of observed UV emission lines in the current JWST observations could be due to a combination of several factors, such as the low spectral resolution ($R \sim 100$) of the NIRSpec prism (the most commonly used mode so far for wide-field MSA observations currently published), the reduced sensitivity of NIRSpec detector at shorter wavelengths, the depth of the exposures, or the physical conditions of the galaxies themselves. With regards to the galaxy conditions, metallicity in particular may not be the issue - current observations are finding that high- z galaxies are generally metal-poor but not metal deficient, with metallicities of $Z \sim 0.03 - 0.6 Z_{\odot}$ (median $Z \sim 0.1 Z_{\odot}$ at $z \sim 3 - 10$; Curti et al. 2023), a range comparable to the CLASSY sample. This suggests that UV lines are being produced in these systems, but not observed due to observational limitations.

The current furthest ($z \sim 10.603$) galaxy spectrum with clear UV and optical emission lines (from Ly α to H γ) is GN-z11, the most luminous candidate $z > 10$ Lyman break galaxy in the GOODS-North field (Bunker et al. 2023a). Surprisingly, GN-z11 shows UV emission lines that we typically

do *not* observe in CLASSY. Indeed, its NIRSpec/prism spectrum clearly shows both N IV] $\lambda\lambda$ 1483,7 and N III] λ 1750 (Bunker et al. 2023a), very rarely observed in the local Universe (see Paper IV). This has opened an intense debate in the literature, with authors implying an extremely elevated nitrogen enrichment (at only 440 Myr from the Big Bang) and proposing different scenarios to explain it, including signatures of globular cluster precursors, massive star winds, runaway stellar collisions or tidal disruption events (Senchyna et al. 2023b; Cameron et al. 2023; Charbonnel et al. 2023). On the other hand, Maiolino et al. (2023) claimed that this object hosts AGN activity which would be the origin of the peculiar nitrogen emission lines, thus solving the issue of the presence of the nitrogen lines and the puzzling N enrichment.

In particular, N IV] $\lambda\lambda$ 1483,7 lines (ionization potential $E > 47.5$ eV) are rarely seen in emission in SFGs (Fosbury et al. 2003; Raiter et al. 2010; Vanzella et al. 2010; Mingozi et al. 2022; Harikane et al. 2023), trace very dense gas ($n_e > 10^4 - 10^5$ cm $^{-3}$) and, when present, they can also be - but not unambiguously - a signature of AGN ionization. N III] $\lambda\lambda$ 1750 instead is a multiplet that could have a nebular origin and be prominent in SFGs, but has been rarely observed (e.g., in the Sunburst Arc, a lensed $z \sim 2.4$ galaxy hosting a $\sim 3-4$ Myr super star cluster; Pascale et al. 2023) and is visible in only two galaxies of the CLASSY sample: Mrk 996 (i.e., J0127-0619) and J1253-0312 (Fig. 20 of Paper IV; $\log(\text{N III]}\lambda 1750/\text{He II}\lambda 1640) \sim 1.34, 0.05$, respectively), both also characterized by WR features in their optical spectra, as commented above. WR stars represent the best tracer of a young ongoing starburst in galaxies, since they are uniquely characterized by very fast and strong winds (especially at high-metallicity), and thus a short lifetime ($\sim 10^5$ yr; Crowther 2007), that can lead to the production of prominent nitrogen features both at optical and UV wavelengths (e.g., Crowther & Smith 1997). In WR-dominated spectra, it is expected also to observe N IV] λ 1719 resonance lines with a clear P-Cygni profile, which can help to discriminate between the nebular and stellar origin of the N III] and N IV] emission. The CLASSY galaxy Mrk 996 shows a N IV] λ 1719 P-Cygni feature, a broad He II λ 1640 (Fig. 10), clear WR features in the optical spectra (James et al. 2009) as well as the N III] λ 1750 multiplet, so a (partly) stellar origin of the UV N emission lines is plausible. In summary, the rare nature of nitrogen lines in UV spectra of nearby SFGs such as Mrk 996 could be due to the limited time frame of the starburst events that are causing them. To shed light on this and understand high- z galaxies such as GN-z11 we need further studies on local samples (including AGN galaxies) where we can broadly observe these UV nitrogen features to ultimately clarify their origin and diagnostic power. Taking into account all these considerations, at the moment we consider N lines not reliable diagnostics for the so-called *UV BPT diagrams*.

7. CONCLUSIONS

In this work, we investigated the optical and UV diagnostics tracing different ionization mechanisms (i.e., SF, AGN, shocks), using the CLASSY survey (Berg et al. 2022; James et al. 2022), that collects for the first time high-quality, high-resolution, and broad-wavelength-range FUV ($\sim 1200 - 2000$ Å) spectra for 45 nearby ($0.002 < z < 0.182$) star-forming galaxies, including analogs of the high- z universe thanks to the broad ISM properties parameter space covered. This paper builds on our results shown in CLASSY Paper IV in which we measured CLASSY UV (from N IV] $\lambda\lambda$ 1483,7 to C III] $\lambda\lambda$ 1907,9) and optical (from [O II] $\lambda\lambda$ 3727 to [S III] λ 9069) emission lines, and several ISM properties (i.e., n_e , T_e , $E(B-V)$, $12+\log(\text{O}/\text{H})$, $\log(U)$).

As a first result of this paper, we confirmed the star-forming nature of our systems using different well-known optical diagnostics sensitive to the dominant ionization source, also taking into account their limitations due to the low metallicity of some of our galaxies. Then, we explored the proposed UV counterparts of these diagnostic diagrams - the so-called “UV-BPT diagrams” - from previous works based on photoionization and shock models (Gutkin et al. 2016; Jaskot & Ravindranath 2016; Hirschmann et al. 2019; 2022). To do this, we compared our measured line ratios (and their corresponding ISM properties) with a set of state-of-the-art models taken from the literature: constant and single-burst SF models from G16; AGN models from F16; shock models from the 3MdBs¹⁷ database (AM19). Finally, we discussed which conditions favor the detection of UV emission lines. In the following, we summarise our findings:

1. In Sec. 4 we explored the classical BPT diagrams, as well as the use of [O I] λ 6300 as a shock diagnostic and the Shirazi & Brinchmann (2012) diagram, that takes into account the He II λ 4686 emission line. In particular, we showed that CLASSY galaxies have [O III]/H β and He II λ 4686/H β typical of SFGs. Also, their broad components - if present - are still generally classified as star-forming, and, even though have enhanced [N II]/H α , [S II]/H α , [O I]/H α and [O I]/[O III] and low [O III]/[O II] (possible evidence of shocks), do not correlate with He II λ 4686, that could be enhanced by shock ionization. Overall, it is not possible to completely exclude the presence of shocks (and possibly AGN activity for the only trans-solar metallicity CLASSY galaxy), but the main ionizing mechanism is clearly SF, especially for the CLASSY subsample showing UV emission lines.

¹⁷ <http://3mdb.astro.unam.mx/>

2. In Sec. 5, we presented our list of reliable UV diagnostic plots that we explored for the CLASSY galaxies showing UV emission lines. Many of the discussed UV diagnostic diagrams can separate SF from AGN and shocks, with the caveat that low $12+\log(\text{O}/\text{H})$ and carbon abundance C/O objects can fall in the AGN/shock-locus proposed by previous authors (e.g., C3He2-C4He2, Fig. 5; C4C3He2-C4C3, Fig. 7; C3He2-C4C3 in App.B), while they usually struggle in separating AGN from shocks. Diagnostics using carbon lines equivalent widths identify the star formation locus, even at low metallicity, low C/O abundance and high $\log(U)$ (e.g., EWC4-C3He2 and EWC3-C3He2; Fig. 8), but the modelled EWs are heavily dependent on the model assumptions of the continuum component. Also, the C IV doublet has a complex nature that still needs to be properly understood and is rarely observed to be purely nebular (see also Sec. 6), thus diagnostic diagrams to investigate the ionization source or ISM properties involving these lines should be used with caution.
3. In Sec. 5, we also concluded that the combination of C III] $\lambda\lambda 1907,9$, He II $\lambda 1640$ and O III] $\lambda 1666$ (C3He2-O3He2, Fig. 6, see Eq. 3, 4; C3He2-C3O3 in App.B, Eq. C1, C2) represents the best diagnostic diagram able to separate all the three ionization mechanisms at sub-solar metallicities. In particular, AGN models show lower O III]/He II and O III]/C III] than shocks, while SF grids are usually located at higher C III]/He II than AGN and shocks.
4. In Sec. 6, we confirmed that UV emission lines observed in CLASSY (with C III] $\lambda\lambda 1907,9$, the most common FUV line, excluding Ly α) are mainly favored in ISMs with low metallicity and high ionization parameters, with none of them visible in targets with $12+\log(\text{O}/\text{H}) \gtrsim 8.3$. In particular, C III]-emitters have systematically lower $\log([\text{N II}]/\text{H}\alpha)$ ($\lesssim -1$; see Fig. 2), can reach high values $\log(\text{He II}\lambda 4686/\text{H}\beta)$ ($\sim -1.4 - -1.8$; Fig. 4), and are clearly shifted to higher $\log([\text{O III}]/\text{H}\beta)$ ($\sim 0.5 - 1$) and higher $\log([\text{O III}]/[\text{O II}])$ ($\sim 0.5 - 1.5$; Fig. 2), and thus higher $\log(U)$. We also describe the caveats involved with using C IV $\lambda\lambda 1548,51$ and He II $\lambda 1640$ emission lines and showed that those measured in CLASSY are mainly nebular, given the consistency of their velocity dispersion with O III] $\lambda 1666$ ($\sigma \sim 50$ km/s; Fig. 1). Finally, while reflecting on the currently puzzling detection of UV emission in high- z systems with JWST, we underlined the almost total absence of nitrogen UV lines (i.e., N IV] $\lambda\lambda 1483,7$, N III] $\lambda 1750$) in the CLASSY survey. Hence, we need further studies of samples where

we can observe these features before attesting their reliability as diagnostics to investigate the main source of ionization.

Overall, this paper together with Paper IV uses the CLASSY survey to provide the tool-kit to investigate ISM properties using UV emission lines. This can be particularly important to explore the $z > 6$ rest-frame UV spectra in the JWST era, in which an unprecedented number of EoR galaxies have already been revealed (e.g., Curtis-Lake et al. 2023; Curti et al. 2022; Arellano-Córdova et al. 2022a; Bunker et al. 2023a; Cameron et al. 2023; Roberts-Borsani et al. 2022).

MM, DAB, KZA-C and XX are grateful for the support for this program, HST-GO-15840, that was provided by NASA through a grant from the Space Telescope Science Institute, which is operated by the Associations of Universities for Research in Astronomy, Incorporated, under NASA contract NAS5-26555. MM, BLJ, SH and NK are thankful for support from the European Space Agency (ESA). Also, MM is grateful to Carlo Cannarozzo, Giovanni Cresci and Alessandro Marconi for inspiring conversations and advice. AF acknowledges the support from grant PRIN MIUR2017-20173ML3WW_001. AW acknowledges the support of UNAM via grant agreement PAPIIT no. IN106922. RA acknowledges support from ANID Fondecyt Regular 1202007. JB acknowledges support by Fundação para a Ciência e a Tecnologia (FCT) through the research grants UID/FIS/04434/2019, UIDB/04434/2020, UIDP/04434/2020, national funds PTDC/FIS-AST/4862/2020 and work contract 2020.03379.CEECIND.

The CLASSY collaboration extends special gratitude to the Lorentz Center for useful discussions during the "Characterizing Galaxies with Spectroscopy with a view for JWST" 2017 workshop that led to the formation of the CLASSY collaboration and survey. The CLASSY collaboration thanks the COS team for all their assistance and advice in the reduction of the COS data.

Funding for SDSS-III has been provided by the Alfred P. Sloan Foundation, the Participating Institutions, the National Science Foundation, and the U.S. Department of Energy Office of Science. The SDSS-III web site is <http://www.sdss3.org/>. SDSS-III is managed by the Astrophysical Research Consortium for the Participating Institutions of the SDSS-III Collaboration including the University of Arizona, the Brazilian Participation Group, Brookhaven National Laboratory, Carnegie Mellon University, University of Florida, the French Participation Group, the German Participation Group, Harvard University, the Instituto de Astrofísica de Canarias, the Michigan State/Notre Dame/JINA Participation Group, Johns Hopkins University, Lawrence

Berkeley National Laboratory, Max Planck Institute for Astrophysics, Max Planck Institute for Extraterrestrial Physics, New Mexico State University, New York University, Ohio State University, Pennsylvania State University, University of Portsmouth, Princeton University, the Spanish Participation Group, University of Tokyo, University of Utah, Vanderbilt University, University of Virginia, University of Washington, and Yale University.

This work also uses the services of the ESO Science Archive Facility, observations collected at the European Southern Observatory under ESO programmes 096.B-0690, 0103.B-0531, 0103.D-0705, and 0104.D-0503, and observations obtained with the Large Binocular Telescope (LBT). The LBT is an international collaboration among institutions in the United States, Italy and Germany. LBT Corporation partners are: The University of Arizona on behalf of the Arizona Board of Regents; Istituto Nazionale di Astrofisica, Italy; LBT Beteiligungsgesellschaft, Germany, representing the Max-Planck Society, The Leibniz Institute for Astrophysics Potsdam, and Heidelberg University; The Ohio State University, University of Notre Dame, University of Minnesota, and University of Virginia.

This research has made use of the HSLA database, developed and maintained at STScI, Baltimore, USA.

All the *HST* data used in this paper can be found in MAST: [10.17909/m3fq-jj25](https://mast.stsci.org/m3fq-jj25).

Facilities: HST (COS), LBT (MODS), APO (SDSS), KECK (KCWI, ESI), VLT (MUSE, VIMOS)

Software: *astropy* (Astropy Collaboration et al. 2013; 2018; 2022) BEAGLE (Chevallard & Charlot 2016), CalCOS (STScI), dustmaps (Green 2018), jupyter (Kluyver et al. 2016), LINMIX (Kelly 2007), MPFIT (Markwardt 2009), MODS reduction Pipeline, Photutils (Bradley et al. 2021), PYNEB (Luridiana et al. 2012; 2015), python, pysynphot (STScI Development Team), RASCAS (Michel-Dansac et al. 2020), SALT (Scarlata & Panagia 2015), STARLIGHT (Fernandes et al. 2005), TLAC (Gronke & Dijkstra 2014), XIDL

REFERENCES

- Abazajian, K. N., Adelman-McCarthy, J. K., Agüeros, M. A., et al. 2009, *ApJS*, 182, 543, doi: [10.1088/0067-0049/182/2/543](https://doi.org/10.1088/0067-0049/182/2/543)
- Alarie, A., & Morisset, C. 2019, *RMxAA*, 55, 377, doi: [10.22201/ia.01851101p.2019.55.02.21](https://doi.org/10.22201/ia.01851101p.2019.55.02.21)
- Allen, M. G., Groves, B. A., Dopita, M. A., Sutherland, R. S., & Kewley, L. J. 2008, *ApJS*, 178, 20
- Amorín, R., Vílchez, J. M., Hägele, G. F., et al. 2012, *ApJL*, 754, L22, doi: [10.1088/2041-8205/754/2/L22](https://doi.org/10.1088/2041-8205/754/2/L22)
- Arellano-Córdova, K. Z., Berg, D. A., Chisholm, J., et al. 2022a, *ApJL*, 940, L23, doi: [10.3847/2041-8213/ac9ab2](https://doi.org/10.3847/2041-8213/ac9ab2)
- Arellano-Córdova, K. Z., Mingozi, M., Berg, D. A., et al. 2022b, *ApJ*, 935, 74, doi: [10.3847/1538-4357/ac7854](https://doi.org/10.3847/1538-4357/ac7854)
- Arrabal Haro, P., Dickinson, M., Finkelstein, S. L., et al. 2023, arXiv e-prints, arXiv:2304.05378, doi: [10.48550/arXiv.2304.05378](https://doi.org/10.48550/arXiv.2304.05378)
- Asplund, M., Grevesse, N., Sauval, A. J., & Scott, P. 2009, *ARA&A*, 47, 481
- Astropy Collaboration, Robitaille, T. P., Tollerud, E. J., et al. 2013, *A&A*, 558, A33, doi: [10.1051/0004-6361/201322068](https://doi.org/10.1051/0004-6361/201322068)

- Astropy Collaboration, Price-Whelan, A. M., Sipőcz, B. M., et al. 2018, *AJ*, 156, 123, doi: [10.3847/1538-3881/aabc4f](https://doi.org/10.3847/1538-3881/aabc4f)
- Astropy Collaboration, Price-Whelan, A. M., Lim, P. L., et al. 2022, *ApJ*, 935, 167, doi: [10.3847/1538-4357/ac7c74](https://doi.org/10.3847/1538-4357/ac7c74)
- Atek, H., Labbé, I., Furtak, L. J., et al. 2023, arXiv e-prints, arXiv:2308.08540, doi: [10.48550/arXiv.2308.08540](https://doi.org/10.48550/arXiv.2308.08540)
- Bagley, M. B., Finkelstein, S. L., Koekemoer, A. M., et al. 2023, *ApJL*, 946, L12, doi: [10.3847/2041-8213/acbb08](https://doi.org/10.3847/2041-8213/acbb08)
- Baldwin, J. A., Phillips, M. M., & Terlevich, R. 1981, *PASP*, 93, 5
- Belfiore, F., Maiolino, R., Maraston, C., et al. 2016, *MNRAS*, 461, 3111, doi: [10.1093/mnras/stw1234](https://doi.org/10.1093/mnras/stw1234)
- Berg, D. A., Chisholm, J., Erb, D. K., et al. 2019, *ApJL*, 878, L3, doi: [10.3847/2041-8213/ab21dc](https://doi.org/10.3847/2041-8213/ab21dc)
- . 2021, arXiv e-prints, arXiv:2105.12765. <https://arxiv.org/abs/2105.12765>
- Berg, D. A., Skillman, E. D., Henry, R. B. C., Erb, D. K., & Carigi, L. 2016, *ApJ*, 827, 126
- Berg, D. A., James, B. L., King, T., et al. 2022, *ApJS*, 261, 31, doi: [10.3847/1538-4365/ac6c03](https://doi.org/10.3847/1538-4365/ac6c03)
- Bosch, G., Hägele, G. F., Amorín, R., et al. 2019, *MNRAS*, 489, 1787, doi: [10.1093/mnras/stz2230](https://doi.org/10.1093/mnras/stz2230)
- Bradley, L., Sipőcz, B., Robitaille, T., et al. 2021, *astropy/photutils*: 1.1.0, 1.1.0, Zenodo, doi: [10.5281/zenodo.4624996](https://doi.org/10.5281/zenodo.4624996)
- Brinchmann, J., Kunth, D., & Durret, F. 2008, *A&A*, 485, 657. <https://arxiv.org/abs/0805.1073>
- Bruzual, G., & Charlot, S. 2003, *MNRAS*, 344, 1000, doi: [10.1046/j.1365-8711.2003.06897.x](https://doi.org/10.1046/j.1365-8711.2003.06897.x)
- Bundy, K., Bershady, M. A., Law, D. R., et al. 2015, *ApJ*, 798, 7, doi: [10.1088/0004-637X/798/1/7](https://doi.org/10.1088/0004-637X/798/1/7)
- Bunker, A. J., Saxena, A., Cameron, A. J., et al. 2023a, arXiv e-prints, arXiv:2302.07256, doi: [10.48550/arXiv.2302.07256](https://doi.org/10.48550/arXiv.2302.07256)
- Bunker, A. J., Cameron, A. J., Curtis-Lake, E., et al. 2023b, arXiv e-prints, arXiv:2306.02467, doi: [10.48550/arXiv.2306.02467](https://doi.org/10.48550/arXiv.2306.02467)
- Byler, N. 2018, *nell-byler/cloudyfps*: Initial release of cloudyFSPS, v1.0.0, Zenodo, doi: [10.5281/zenodo.1156412](https://doi.org/10.5281/zenodo.1156412)
- Byler, N., Dalcanton, J. J., Conroy, C., & Johnson, B. D. 2017, *ApJ*, 840, 44
- Byler, N., Dalcanton, J. J., Conroy, C., et al. 2018, *ApJ*, 863, 14, doi: [10.3847/1538-4357/aacd50](https://doi.org/10.3847/1538-4357/aacd50)
- Byler, N., Kewley, L. J., Rigby, J. R., et al. 2020, *ApJ*, 893, 1, doi: [10.3847/1538-4357/ab7ea9](https://doi.org/10.3847/1538-4357/ab7ea9)
- Cameron, A. J., Saxena, A., Bunker, A. J., et al. 2023, arXiv e-prints, arXiv:2302.04298, doi: [10.48550/arXiv.2302.04298](https://doi.org/10.48550/arXiv.2302.04298)
- Cann, J. M., Satyapal, S., Abel, N. P., et al. 2018, *ApJ*, 861, 142, doi: [10.3847/1538-4357/aac64a](https://doi.org/10.3847/1538-4357/aac64a)
- Cann, J. M., Satyapal, S., Bohn, T., et al. 2020, *ApJ*, 895, 147, doi: [10.3847/1538-4357/ab8b64](https://doi.org/10.3847/1538-4357/ab8b64)
- Cann, J. M., Satyapal, S., Rothberg, B., et al. 2021, *ApJL*, 912, L2, doi: [10.3847/2041-8213/abf56d](https://doi.org/10.3847/2041-8213/abf56d)
- Cardelli, J. A., Clayton, G. C., & Mathis, J. S. 1989, *ApJ*, 345, 245
- Castellano, M., Fontana, A., Treu, T., et al. 2022, arXiv e-prints, arXiv:2212.06666, doi: [10.48550/arXiv.2212.06666](https://doi.org/10.48550/arXiv.2212.06666)
- Chabrier, G. 2003, *PASP*, 115, 763, doi: [10.1086/376392](https://doi.org/10.1086/376392)
- Charbonnel, C., Schaerer, D., Prantzos, N., et al. 2023, arXiv e-prints, arXiv:2303.07955, doi: [10.48550/arXiv.2303.07955](https://doi.org/10.48550/arXiv.2303.07955)
- Chevallard, J., & Charlot, S. 2016, *MNRAS*, 462, 1415, doi: [10.1093/mnras/stw1756](https://doi.org/10.1093/mnras/stw1756)
- Chisholm, J., Rigby, J. R., Bayliss, M., et al. 2019, *ApJ*, 882, 182, doi: [10.3847/1538-4357/ab3104](https://doi.org/10.3847/1538-4357/ab3104)
- Concas, A., Maiolino, R., Curti, M., et al. 2022, *MNRAS*, 513, 2535, doi: [10.1093/mnras/stac1026](https://doi.org/10.1093/mnras/stac1026)
- Crowther, P. A. 2007, 45, 177
- Crowther, P. A., & Smith, L. J. 1997, *A&A*, 320, 500
- Curti, M., D'Eugenio, F., Carniani, S., et al. 2022, arXiv e-prints, arXiv:2207.12375. <https://arxiv.org/abs/2207.12375>
- Curti, M., Maiolino, R., Curtis-Lake, E., et al. 2023, arXiv e-prints, arXiv:2304.08516, doi: [10.48550/arXiv.2304.08516](https://doi.org/10.48550/arXiv.2304.08516)
- Curtis-Lake, E., Carniani, S., Cameron, A., et al. 2023, *Nature Astronomy*, 7, 622, doi: [10.1038/s41550-023-01918-w](https://doi.org/10.1038/s41550-023-01918-w)
- del Valle-Espinosa, M. G., Sanchez-Janssen, R., Amorin, R., et al. 2022, arXiv e-prints, arXiv:2212.10585, doi: [10.48550/arXiv.2212.10585](https://doi.org/10.48550/arXiv.2212.10585)
- Denicoló, G., Terlevich, R., & Terlevich, E. 2002, *MNRAS*, 330, 69, doi: [10.1046/j.1365-8711.2002.05041.x](https://doi.org/10.1046/j.1365-8711.2002.05041.x)
- Dopita, M. A., & Sutherland, R. S. 1995, *ApJ*, 455, 468, doi: [10.1086/176596](https://doi.org/10.1086/176596)
- . 1996, *ApJS*, 102, 161, doi: [10.1086/192255](https://doi.org/10.1086/192255)
- . 2003, *Astrophysics of the diffuse universe*
- Dopita, M. A., Sutherland, R. S., Nicholls, D. C., Kewley, L. J., & Vogt, F. P. A. 2013, *ApJS*, 208, 10
- Dors, O. L., Agarwal, B., Hägele, G. F., et al. 2018, *MNRAS*, 479, 2294, doi: [10.1093/mnras/sty1658](https://doi.org/10.1093/mnras/sty1658)
- Draine, B. T. 2011, *Physics of the Interstellar and Intergalactic Medium*
- Du, X., Shapley, A. E., Martin, C. L., & Coil, A. L. 2017, *ApJ*, 838, 63, doi: [10.3847/1538-4357/aa64cf](https://doi.org/10.3847/1538-4357/aa64cf)
- Eldridge, J. J., & Stanway, E. R. 2009, *MNRAS*, 400, 1019
- Eldridge, J. J., Stanway, E. R., Xiao, L., McClelland, L. A. S., & others. 2017, *PASA*, 34, e058, doi: [10.1017/pasa.2017.51](https://doi.org/10.1017/pasa.2017.51)
- Feltre, A., Charlot, S., & Gutkin, J. 2016, *MNRAS*, 456, 3354
- Ferland, G. J., Porter, R. L., van Hoof, P. A. M., & others. 2013, *RMxAA*, 49, 137
- Fernandes, I. F., Gruenwald, R., & Viegas, S. M. 2005, *MNRAS*, 364, 674
- Finkelstein, S. L., Bagley, M. B., Arrabal Haro, P., et al. 2022, *ApJL*, 940, L55, doi: [10.3847/2041-8213/ac966e](https://doi.org/10.3847/2041-8213/ac966e)
- Fosbury, R. A. E., Villar-Martín, M., & others. 2003, *ApJ*, 596, 797
- Garnett, D. R., Kennicutt, Jr., R. C., Chu, Y.-H., & Skillman, E. D. 1991, *ApJ*, 373, 458
- Grandi, S. A. 1976, *ApJ*, 206, 658, doi: [10.1086/154424](https://doi.org/10.1086/154424)

- Green, G. 2018, *The Journal of Open Source Software*, 3, 695, doi: [10.21105/joss.00695](https://doi.org/10.21105/joss.00695)
- Gronke, M., & Dijkstra, M. 2014, *MNRAS*, 444, 1095, doi: [10.1093/mnras/stu1513](https://doi.org/10.1093/mnras/stu1513)
- Groves, B. A., Heckman, T. M., & Kauffmann, G. 2006, *MNRAS*, 371, 1559, doi: [10.1111/j.1365-2966.2006.10812.x](https://doi.org/10.1111/j.1365-2966.2006.10812.x)
- Gutkin, J., Charlot, S., & Bruzual, G. 2016, *MNRAS*, 462, 1757
- Harikane, Y., Nakajima, K., Ouchi, M., et al. 2023, arXiv e-prints, arXiv:2304.06658, doi: [10.48550/arXiv.2304.06658](https://doi.org/10.48550/arXiv.2304.06658)
- Hatano, S., Ouchi, M., Nakajima, K., et al. 2023, arXiv e-prints, arXiv:2304.03726, doi: [10.48550/arXiv.2304.03726](https://doi.org/10.48550/arXiv.2304.03726)
- Hayes, M. 2015, *PASA*, 32, e027, doi: [10.1017/pasa.2015.25](https://doi.org/10.1017/pasa.2015.25)
- Heckman, T. M. 1980, *A&A*, 87, 152
- Heckman, T. M., Robert, C., Leitherer, C., Garnett, D. R., & van der Rydt, F. 1998, *ApJ*, 503, 646, doi: [10.1086/306035](https://doi.org/10.1086/306035)
- Henry, R. B. C., Edmunds, M. G., & Köppen, J. 2000, *ApJ*, 541, 660
- Herenz, E. C., Micheva, G., Weilbacher, P. M., et al. 2023, *Research Notes of the AAS*, 7, 99, doi: [10.3847/2515-5172/acd69e](https://doi.org/10.3847/2515-5172/acd69e)
- Hirschmann, M., Charlot, S., Feltre, A., et al. 2019, *MNRAS*, 487, 333, doi: [10.1093/mnras/stz1256](https://doi.org/10.1093/mnras/stz1256)
- . 2022, arXiv e-prints, arXiv:2212.02522, <https://arxiv.org/abs/2212.02522>
- Ho, I. T., Kewley, L. J., Dopita, M. A., et al. 2014, *MNRAS*, 444, 3894, doi: [10.1093/mnras/stu1653](https://doi.org/10.1093/mnras/stu1653)
- Hogarth, L., Amorín, R., Vílchez, J. M., et al. 2020, *MNRAS*, 494, 3541, doi: [10.1093/mnras/staa851](https://doi.org/10.1093/mnras/staa851)
- Hu, W., Martin, C. L., Gronke, M., et al. 2023, *ApJ*, 956, 39, doi: [10.3847/1538-4357/aceefd](https://doi.org/10.3847/1538-4357/aceefd)
- Izotov, Y. I., Chaffee, F. H., & Schaerer, D. 2001, *A&A*, 378, L45, doi: [10.1051/0004-6361:20011265](https://doi.org/10.1051/0004-6361:20011265)
- Izotov, Y. I., Schaerer, D., Blecha, A., et al. 2006, *A&A*, 459, 71, doi: [10.1051/0004-6361:20065622](https://doi.org/10.1051/0004-6361:20065622)
- Izotov, Y. I., & Thuan, T. X. 1999, *ApJ*, 511, 639
- . 2007, *ApJ*, 665, 1115
- James, B. L., Pettini, M., Christensen, L., et al. 2014, *MNRAS*, 440, 1794
- James, B. L., Tsamis, Y. G., Barlow, M. J., et al. 2009, *MNRAS*, 398, 2, doi: [10.1111/j.1365-2966.2009.15172.x](https://doi.org/10.1111/j.1365-2966.2009.15172.x)
- James, B. L., Berg, D. A., King, T., et al. 2022, arXiv e-prints, arXiv:2206.01224, <https://arxiv.org/abs/2206.01224>
- Jaskot, A. E., & Ravindranath, S. 2016, *ApJ*, 833, 136
- Kauffmann, G., Heckman, T. M., Tremonti, C., et al. 2003, *MNRAS*, 346, 1055, doi: [10.1111/j.1365-2966.2003.07154.x](https://doi.org/10.1111/j.1365-2966.2003.07154.x)
- Keel, W. C. 1983, *ApJ*, 269, 466, doi: [10.1086/161057](https://doi.org/10.1086/161057)
- Kelly, B. C. 2007, *ApJ*, 665, 1489
- Kewley, L. J., & Dopita, M. A. 2002, *ApJS*, 142, 35
- Kewley, L. J., Dopita, M. A., Sutherland, R. S., Heisler, C. A., & Trevena, J. 2001, *ApJ*, 556, 121
- Kewley, L. J., & Ellison, S. L. 2008, *ApJ*, 681, 1183
- Kewley, L. J., Groves, B., Kauffmann, G., & Heckman, T. 2006, *MNRAS*, 372, 961, doi: [10.1111/j.1365-2966.2006.10859.x](https://doi.org/10.1111/j.1365-2966.2006.10859.x)
- Kewley, L. J., Nicholls, D. C., & Sutherland, R. S. 2019, *ARA&A*, 57, 511, doi: [10.1146/annurev-astro-081817-051832](https://doi.org/10.1146/annurev-astro-081817-051832)
- Kluyver, T., Ragan-Kelley, B., Pérez, F., et al. 2016, in *Positioning and Power in Academic Publishing: Players, Agents and Agendas*, ed. F. Loizides & B. Schmidt, IOS Press, 87 – 90
- Komarova, L., Oey, M. S., Krumholz, M. R., et al. 2021, *ApJL*, 920, L46, doi: [10.3847/2041-8213/ac2c09](https://doi.org/10.3847/2041-8213/ac2c09)
- Korista, K. T., & Ferland, G. J. 1989, *ApJ*, 343, 678, doi: [10.1086/167739](https://doi.org/10.1086/167739)
- Kroupa, P. 2001, *MNRAS*, 322, 231, doi: [10.1046/j.1365-8711.2001.04022.x](https://doi.org/10.1046/j.1365-8711.2001.04022.x)
- Lamareille, F. 2010, *A&A*, 509, A53, doi: [10.1051/0004-6361/200913168](https://doi.org/10.1051/0004-6361/200913168)
- Lamareille, F., Mouhcine, M., Contini, T., Lewis, I., & Maddox, S. 2004, *MNRAS*, 350, 396, doi: [10.1111/j.1365-2966.2004.07697.x](https://doi.org/10.1111/j.1365-2966.2004.07697.x)
- Leitherer, C., Leão, J. R. S., Heckman, T. M., & others. 2001, *ApJ*, 550, 724
- Luridiana, V., Morisset, C., & Shaw, R. A. 2012, in *IAU Symposium*, Vol. 283, IAU Symposium, 422–423
- Luridiana, V., Morisset, C., & Shaw, R. A. 2015, *A&A*, 573, A42
- Madau, P., & Haardt, F. 2015, *ApJL*, 813, L8
- Mainali, R., Kollmeier, J. A., Stark, D. P., & others. 2017, *ApJL*, 836, L14
- Mainali, R., Zitrin, A., Stark, D. P., et al. 2018, *MNRAS*, 479, 1180
- Maiolino, R., Scholtz, J., Witstok, J., et al. 2023, arXiv e-prints, arXiv:2305.12492, doi: [10.48550/arXiv.2305.12492](https://doi.org/10.48550/arXiv.2305.12492)
- Marasco, A., Belfiore, F., Cresci, G., et al. 2023, *A&A*, 670, A92, doi: [10.1051/0004-6361/202244895](https://doi.org/10.1051/0004-6361/202244895)
- Markwardt, C. B. 2009, in *Astronomical Society of the Pacific Conference Series*, Vol. 411, *Astronomical Data Analysis Software and Systems XVIII*, ed. D. A. Bohlender, D. Durand, & P. Dowler, 251
- Maseda, M. V., Brinchmann, J., Franx, M., et al. 2017, *A&A*, 608, A4, doi: [10.1051/0004-6361/201730985](https://doi.org/10.1051/0004-6361/201730985)
- Mathee, J., Mackenzie, R., Simcoe, R. A., et al. 2022, arXiv e-prints, arXiv:2211.08255, doi: [10.48550/arXiv.2211.08255](https://doi.org/10.48550/arXiv.2211.08255)
- Mayya, Y. D., Plat, A., Gómez-González, V. M. A., et al. 2023, *MNRAS*, 519, 5492, doi: [10.1093/mnras/stad017](https://doi.org/10.1093/mnras/stad017)
- McElroy, R., Croom, S. M., Pracy, M., et al. 2015, *MNRAS*, 446, 2186, doi: [10.1093/mnras/stu2224](https://doi.org/10.1093/mnras/stu2224)
- Michel-Dansac, L., Blaizot, J., Garel, T., et al. 2020, *A&A*, 635, A154, doi: [10.1051/0004-6361/201834961](https://doi.org/10.1051/0004-6361/201834961)
- Mingozzi, M., Cresci, G., Venturi, G., et al. 2019, *A&A*, 622, A146, doi: [10.1051/0004-6361/201834372](https://doi.org/10.1051/0004-6361/201834372)
- Mingozzi, M., James, B. L., Arellano-Córdova, K. Z., et al. 2022, *ApJ*, 939, 110, doi: [10.3847/1538-4357/ac952c](https://doi.org/10.3847/1538-4357/ac952c)

- Molina, M., Reines, A. E., Latimer, L. J., Baldassare, V., & Salehirad, S. 2021, *ApJ*, 922, 155, doi: [10.3847/1538-4357/ac1ffa](https://doi.org/10.3847/1538-4357/ac1ffa)
- Nagao, T., Maiolino, R., & Marconi, A. 2006, *A&A*, 447, 863, doi: [10.1051/0004-6361/20054127](https://doi.org/10.1051/0004-6361/20054127)
- Nakajima, K., & Maiolino, R. 2022, *MNRAS*, 513, 5134, doi: [10.1093/mnras/stac1242](https://doi.org/10.1093/mnras/stac1242)
- Nakajima, K., Schaerer, D., Le Fèvre, O., et al. 2018, *A&A*, 612, A94, doi: [10.1051/0004-6361/201731935](https://doi.org/10.1051/0004-6361/201731935)
- Nanayakkara, T., Brinchmann, J., Boogaard, L., et al. 2019, *A&A*, 624, A89, doi: [10.1051/0004-6361/201834565](https://doi.org/10.1051/0004-6361/201834565)
- Osterbrock, D. E., & Ferland, G. J. 2006, *Astrophysics of gaseous nebulae and active galactic nuclei*
- Pascale, M., Dai, L., McKee, C. F., & Tsang, B. T. H. 2023, arXiv e-prints, arXiv:2301.10790, doi: [10.48550/arXiv.2301.10790](https://doi.org/10.48550/arXiv.2301.10790)
- Pettini, M., & Pagel, B. E. J. 2004, *MNRAS*, 348, L59
- Plat, A., Charlot, S., Bruzual, G., et al. 2019, *MNRAS*, 490, 978, doi: [10.1093/mnras/stz2616](https://doi.org/10.1093/mnras/stz2616)
- Polimera, M. S., Kannappan, S. J., Richardson, C. T., et al. 2022, *ApJ*, 931, 44, doi: [10.3847/1538-4357/ac6595](https://doi.org/10.3847/1538-4357/ac6595)
- Raiter, A., Fosbury, R. A. E., & Teimoorinia, H. 2010, *A&A*, 510, A109, doi: [10.1051/0004-6361/200912429](https://doi.org/10.1051/0004-6361/200912429)
- Ravindranath, S., Monroe, T., Jaskot, A., Ferguson, H. C., & Tumlinson, J. 2020, *ApJ*, 896, 170, doi: [10.3847/1538-4357/ab91a5](https://doi.org/10.3847/1538-4357/ab91a5)
- Reines, A. E., Condon, J. J., Darling, J., & Greene, J. E. 2020, *ApJ*, 888, 36, doi: [10.3847/1538-4357/ab4999](https://doi.org/10.3847/1538-4357/ab4999)
- Rich, J. A., Dopita, M. A., Kewley, L. J., & Rupke, D. S. N. 2010, *ApJ*, 721, 505, doi: [10.1088/0004-637X/721/1/505](https://doi.org/10.1088/0004-637X/721/1/505)
- Rigby, J. R., Bayliss, M. B., Gladders, M. D., & others. 2015, *ApJL*, 814, L6
- Rigby, J. R., Bayliss, M. B., Sharon, K., et al. 2018, *AJ*, 155, 104, doi: [10.3847/1538-3881/aaa2ff](https://doi.org/10.3847/1538-3881/aaa2ff)
- Roberts-Borsani, G., Morishita, T., Treu, T., et al. 2022, *ApJL*, 938, L13, doi: [10.3847/2041-8213/ac8e6e](https://doi.org/10.3847/2041-8213/ac8e6e)
- Robertson, B. E., Ellis, R. S., Furlanetto, S. R., & Dunlop, J. S. 2015, *ApJL*, 802, L19
- Sartori, L. F., Schawinski, K., Treister, E., et al. 2015, *MNRAS*, 454, 3722, doi: [10.1093/mnras/stv2238](https://doi.org/10.1093/mnras/stv2238)
- Scarlata, C., & Panagia, N. 2015, *ApJ*, 801, 43
- Schaerer, D., & Vacca, W. D. 1998, *ApJ*, 497, 618
- Schaerer, D., Izotov, Y. I., Worseck, G., et al. 2022, arXiv e-prints, arXiv:2202.07768. <https://arxiv.org/abs/2202.07768>
- Schmutz, W., Leitherer, C., & Gruenwald, R. 1992, *PASP*, 104, 1164, doi: [10.1086/133104](https://doi.org/10.1086/133104)
- Senchyna, P., Chisholm, J., Berg, D. A., James, B. L., & others (in preparation). 2023a, *ApJ*
- Senchyna, P., Plat, A., Stark, D. P., & Rudie, G. C. 2023b, arXiv e-prints, arXiv:2303.04179, doi: [10.48550/arXiv.2303.04179](https://doi.org/10.48550/arXiv.2303.04179)
- Senchyna, P., Stark, D. P., Chevillard, J., et al. 2019, *MNRAS*, 488, 3492, doi: [10.1093/mnras/stz1907](https://doi.org/10.1093/mnras/stz1907)
- Senchyna, P., Stark, D. P., Charlot, S., et al. 2021, arXiv e-prints, arXiv:2111.11508. <https://arxiv.org/abs/2111.11508>
- Shapley, A. E., Steidel, C. C., Pettini, M., & Adelberger, K. L. 2003, *ApJ*, 588, 65
- Shirazi, M., & Brinchmann, J. 2012, *MNRAS*, 421, 1043
- Simmonds, C., Tacchella, S., Hainline, K., et al. 2023, arXiv e-prints, arXiv:2310.01112, doi: [10.48550/arXiv.2310.01112](https://doi.org/10.48550/arXiv.2310.01112)
- Sixtos, A., Wofford, A., Sander, A. A. C., & Peimbert, A. 2023, *MNRAS*, 519, 5656, doi: [10.1093/mnras/stac3732](https://doi.org/10.1093/mnras/stac3732)
- Smith, L. J., Oey, M. S., Hernandez, S., et al. 2023, arXiv e-prints, arXiv:2310.03413, doi: [10.48550/arXiv.2310.03413](https://doi.org/10.48550/arXiv.2310.03413)
- Stanway, E. R., Eldridge, J. J., & Becker, G. D. 2016, *MNRAS*, 456, 485
- Stark, D. P. 2016, *ARA&A*, 54, 761
- Stark, D. P., Richard, J., Charlot, S., & others. 2015, *MNRAS*, 450, 1846
- Stasińska, G., Izotov, Y., Morisset, C., & Guseva, N. 2015, *A&A*, 576, A83, doi: [10.1051/0004-6361/201425389](https://doi.org/10.1051/0004-6361/201425389)
- Steidel, C. C., Strom, A. L., Pettini, M., et al. 2016, *ApJ*, 826, 159
- Stephenson, M. G., Arellano-Córdova, K. Z., Berg, D. A., Mingozi, M., & James, B. L. 2023, *Research Notes of the American Astronomical Society*, 7, 31, doi: [10.3847/2515-5172/acbc12](https://doi.org/10.3847/2515-5172/acbc12)
- Sutherland, R. S., & Dopita, M. A. 2017, *ApJS*, 229, 34, doi: [10.3847/1538-4365/aa6541](https://doi.org/10.3847/1538-4365/aa6541)
- Thuan, T. X., & Izotov, Y. I. 2005, *ApJ*, 161, 240
- Tozzi, G., Maiolino, R., Cresci, G., et al. 2023, arXiv e-prints, arXiv:2302.04282, doi: [10.48550/arXiv.2302.04282](https://doi.org/10.48550/arXiv.2302.04282)
- Treu, T., Roberts-Borsani, G., Bradac, M., et al. 2022, *ApJ*, 935, 110, doi: [10.3847/1538-4357/ac8158](https://doi.org/10.3847/1538-4357/ac8158)
- Trump, J. R., Arrabal Haro, P., Simons, R. C., et al. 2023, *ApJ*, 945, 35, doi: [10.3847/1538-4357/acba8a](https://doi.org/10.3847/1538-4357/acba8a)
- Vanzella, E., Grazian, A., Hayes, M., et al. 2010, *A&A*, 513, A20, doi: [10.1051/0004-6361/200913042](https://doi.org/10.1051/0004-6361/200913042)
- Veilleux, S., & Osterbrock, D. E. 1987, *ApJS*, 63, 295, doi: [10.1086/191166](https://doi.org/10.1086/191166)
- Verhamme, A., Orlitová, I., Schaerer, D., et al. 2017, *A&A*, 597, A13
- Wise, J. H., Demchenko, V. G., Halicek, M. T., et al. 2014, *MNRAS*, 442, 2560
- Wofford, A., Vidal-García, A., Feltre, A., Chevillard, J., et al. 2021, *MNRAS*, 500, 2908, doi: [10.1093/mnras/staa3365](https://doi.org/10.1093/mnras/staa3365)
- Wofford, A., Sixtos, A., Charlot, S., et al. 2023, *MNRAS*, 523, 3949, doi: [10.1093/mnras/stad1622](https://doi.org/10.1093/mnras/stad1622)
- Xiao, L., Stanway, E. R., & Eldridge, J. J. 2018, *MNRAS*, 477, 904, doi: [10.1093/mnras/sty646](https://doi.org/10.1093/mnras/sty646)
- Xu, X., Heckman, T., Henry, A., et al. 2022, *ApJ*, 933, 222, doi: [10.3847/1538-4357/ac6d56](https://doi.org/10.3847/1538-4357/ac6d56)

—, 2023, arXiv e-prints, arXiv:2301.11498,
doi: [10.48550/arXiv.2301.11498](https://doi.org/10.48550/arXiv.2301.11498)

APPENDIX

A. COMPARING UV AND OPTICAL KINEMATICS

Here we want to further discuss the emission line kinematics, also comparing optical and UV results. The left and right panels of Fig. 11 show the velocity offset of the UV stellar (left panel) and gas kinematics (right panel) with respect to the systemic velocity v_{sys} (derived from z_{fit}), consistent with the ionized gas velocity measured from optical emission lines, as a function of the galaxy stellar mass. In general, we find no systematic offsets between the ionizing stellar component velocity explored by fitting the UV spectra (magenta squares) and v_{sys} , with Δv mainly within $\pm \sim 50$ km/s and median value $\langle \Delta v \rangle \sim 7$ km/s (dash-dotted magenta line). One implication is that the narrow components of the optical emission lines are really tracing non-outflowing gas (Rigby et al. 2018). The right panel of Fig. 11 instead shows the O III] $\lambda\lambda 1661,6$, C III] $\lambda\lambda 1907,9$, and C IV $\lambda\lambda 1548,51$ velocities as red dots, blue triangles and yellow stars. There is a scatter between the UV and systemic velocities mainly within $\pm \sim 50$ km/s, and more enhanced for some C III] measurements, with three galaxies (J1359+5726, J0926+4427 and J0942+3547) showing a clear redshifted offset ($\Delta v \sim +100-200$ km/s) and three (IZw 18, Mrk 996 and J1025+3622) showing a clear blueshifted offset ($\delta v \sim -150-200$ km/s). However, we do not see either any systematic offsets, as shown by the dashed red and dotted blue lines indicating the corresponding median values with respect to v_{sys} . Hence, we conclude it is unlikely that they are due to issues in the G185M grating calibration, covering the C III], discussed in detail in James et al. (2022).

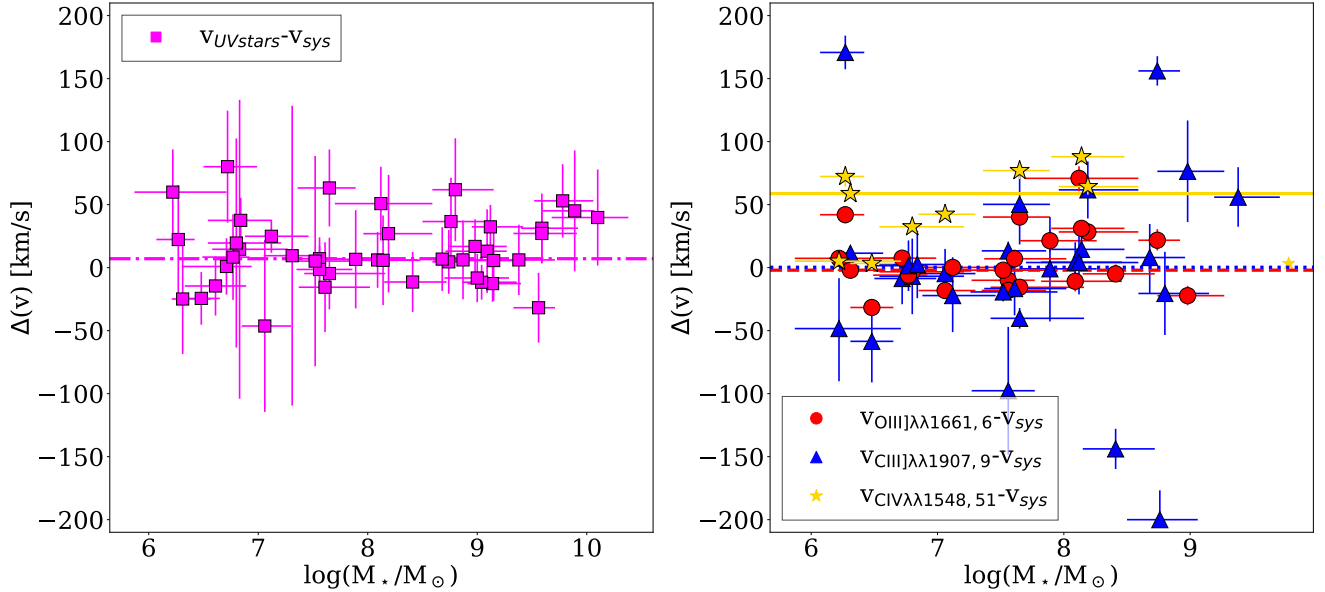


Figure 11. Velocity offset of the UV stellar (left panel, magenta squares) and gas kinematics (right panel) with respect to the systemic velocity v_{sys} , consistent with the ionized gas velocity measured from optical spectra, and as a function of the galaxy stellar mass. In the right panel, we indicate the O III] $\lambda\lambda 1661,6$, C III] $\lambda\lambda 1907,9$, and C IV $\lambda\lambda 1548,51$ velocities as red dots, blue triangles and yellow stars, as reported in the legend.

Interestingly, we find a systematic offset between the v_{CIV} and v_{sys} with a median value of $\langle \Delta v \rangle \sim +60$ km/s (solid gold line), implying that C IV emission is systematically redshifted with respect to the systemic velocity, consistently with resonant scattering/absorption (see also Berg et al. 2019; Wofford et al. 2021). For seven out of the nine galaxies for which we measure C IV nebular emission, this blueshifted offset increases with the stellar mass, going from ~ 0 km/s to ~ 90 km/s in the range $\log(M_*/M_\odot)$ 6–8. The two exceptions are IZw 18 and J1323-0132, with stellar masses of $\log(M_*/M_\odot) \sim 6.3$, showing $\delta v \sim 65$ km/s.

As discussed in Sec. 2.2 and in Fig. 1, optical emission lines of half of the CLASSY sample needed a narrow and a broad Gaussian component to be accurately reproduced. Looking at the single and narrow component σ values shown in the right panel of Fig. 1, we see that σ (and also its scatter) increases at larger stellar masses, with only objects with $M_* \gtrsim 10^7 M_\odot$ needing

a 2-component fit. We highlight here that all the galaxies characterized by a broad component in optical emission lines (apart Mrk 996 and SBS 0335-052 E) were found to have an outflowing component in rest-UV absorption lines analyzed by Xu et al. (2022; 2023) (CLASSY Paper III, Paper VI). Recent studies have shown that low-mass systems ($M_* < 10^9 M_\odot$) such as those of the CLASSY survey can have irregular velocity fields in the ionized gas studied through optical emission lines, indicating the presence of non-circular motions (e.g., Marasco et al. 2023). However, galactic winds, defined as gas at velocities larger than the galaxy escape speed, have found to be able to account only for a few percent of their observed fluxes both in the local universe (Marasco et al. 2023) and at $z \sim 1.2-2.6$ (Concas et al. 2022). Here we highlight that the lack of galactic wind detection in small systems could be also an issue of S/N, but in this work we do not explore this topic any further, leaving it to a future study using optical integral-field spectroscopy data, that can provide both a spatial and kinematical information of our galaxies, and thus a more complete picture that the integrated optical spectra analyzed here cannot provide.

B. ALTERNATIVE DIAGNOSTIC DIAGRAMS

Fig. 12 shows an alternative optical diagnostic diagram to discriminate the excitation properties, using $[\text{O II}] \lambda\lambda 3727/\text{H}\beta$ versus $[\text{O III}] \lambda 5007/\text{H}\beta$ line ratios (Lamareille et al. 2004; Lamareille 2010). The dotted, solid and dashed lines indicate the empirical dividing line between star-forming galaxies and AGN identified by Lamareille et al. (2004), while the dash-dotted line identifies the empirical locus of LI(N)ER and composite galaxies, found by Lamareille (2010). The advantage of this diagram is that it can be used to explore JWST targets at redshifts up to $z \sim 8.5$ in the observed NIR (with NIRISS or NIRspec), for which redder wavelengths are unavailable (e.g., Curti et al. 2022). However, this diagram should be taken with caution since, as shown in Table 2, it does not always disentangle ionizing mechanisms in our sample, with many galaxies (classified as star-forming according to the classical BPT) lying in the boundary region between SF and Seyferts and thus classified as composite. This shows the limit of $[\text{O II}]/\text{H}\beta$ in distinguishing among ionization mechanisms.

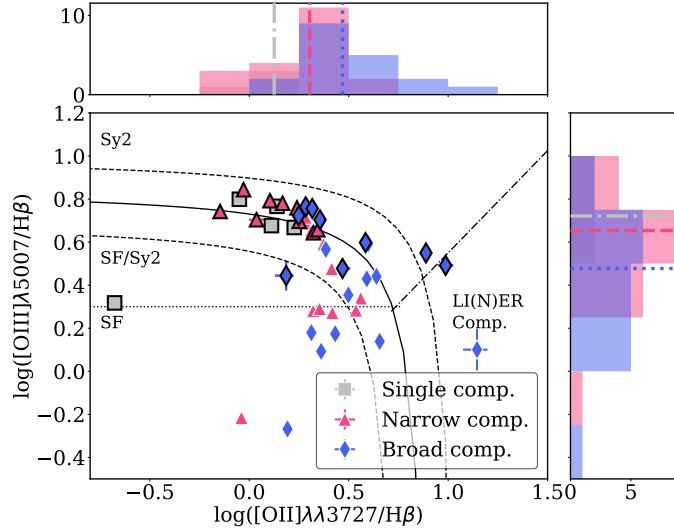


Figure 12. Analogously to Fig. 2, $[\text{O II}] \lambda\lambda 3727/\text{H}\beta$ versus $[\text{O III}] \lambda 5007/\text{H}\beta$ diagnostic diagram for the narrow and broad components of the CLASSY galaxies, shown as red dots and blue diamonds, respectively. Only the measurements with $S/N > 3$ for all the lines involved are reported. The dotted and solid lines indicate the empirical dividing line between star-forming galaxies and AGN identified by Lamareille et al. (2004), the dashed ones show the uncertainty region, while the dash-dotted line identifies the empirical locus of LI(N)ER and Seyfert galaxies, found by Lamareille (2010). Unfortunately, this diagnostic plot does not represent a good tool to discriminate among the different ionizing mechanisms of our systems.

C. OTHER UV DIAGNOSTIC DIAGRAMS

C.1. The effect of stellar rotation and multiplicity on UV line ratios

In this section, we compare G16, B17 and X18 bursty models presented in Tab. 1. B17 models take into account only stellar rotation and X18 models only stellar multiplicity, while G16 models neither of the two. The differences in how G16 and B17 grids differ with respect to X18 models in the UV diagnostic diagrams discussed in Fig. 5, 6 and 7 are shown in Fig. 13.

In particular, in Fig. 13 we show G16 and B17 grids at 3, 5 and 10 Myr. The bursty G16 grids seem unable to reproduce the lowest C IV/He II, C III]/He II and (C IV+C III])/He II line ratios. This is because, for clarity reasons, we have only shown a subset of G16 model parameter space, considering only $(C/O)/(C/O)_{\odot} = 0.72$ and the IMF cut at $M_{up} = 100 M_{\odot}$. Considering either a lower C/O or a higher IMF cut, the 3 Myr grid can reproduce the line ratios observed for the CLASSY galaxies, as shown for the constant SF grids in Fig. 5, 6 and 7. However, at higher ages the ionizing photons drop with a subsequent reduction of He II (but also C III] and C IV), inducing a shift of the grids to higher C III]/He II and C IV/He II than the range shown in Fig. 5 (see e.g., Jaskot & Ravindranath 2016 Sec. 3.1 for a detailed comparison between different model prescriptions). On the other hand, B17 models at 3 and 5 Myr behave similarly to X18 grids at 3 and 10 Myr¹⁸, with the one at 5 Myr going beyond the SF locus defined by the CLASSY galaxies, partly covering the shock/AGN regions. The B17 grid at 10 Myr, instead, is unable to reproduce the observed line ratios, being shifted to higher C III]/He II and (C IV+C III])/He II (in the opposite direction with respect to the AGN/shock regions) because of the reduced ionizing radiation, unable to enhance He II emission. The main take-away from Fig. 13 is that, as discussed in Sec. 3, stellar rotation and multiplicity have the effect of amplifying the stellar ionizing radiation for several Myr after a star formation burst. Overall, the different grids at 3 Myr can reproduce the observed line ratios of star-forming galaxies.

C.2. Other UV diagnostic diagrams

Fig. 14 and 15 show the C3He2-C3O3 and C3He2-C4C3 diagrams, respectively, proposed together with the C3He2-O3He2 diagram (Fig. 6) by F16. C3He2-C3O3 behaves similarly to C3He2-O3He2 (Fig. 6), and thus, at sub-solar metallicities, it can clearly distinguish among SF, AGN and shocks, as shown by the Shock-SF separator

$$y = 2.1x + 0.6 \quad (C1)$$

and the AGN-SF separator lines

$$y = 0.1 \quad \text{and} \quad x < -0.25 \quad (C2)$$

with $x = \log([\text{O III}]\lambda 1666/\text{C III}]\lambda\lambda 1907,9)$ and $y = \log(\text{C III}]\lambda\lambda 1907,9/\text{He II}\lambda 1640)$. At sub-solar metallicities (i.e., excluding the dark-green shock grid), shocks can reach higher [O III]/C III] line ratios than AGN models, while SF grids are located at higher C III]/He II values.

C3He2-C4C3 instead behaves similarly to C3He2-C4He2 diagram (Fig. 5) and are a very similar version of the C4C3He2-C4C3 diagram (Fig. 7). There is not a clear difference in C IV/C III] line ratios between the different models, and thus the difference between SF and other mechanisms is mainly traced by the different C III]/He II (higher for SF grids, lower for AGN/shocks), as indicated by the Shock-SF separator

$$y \geq 0.1 \quad \text{and} \quad x \geq 0.1 \quad (C3)$$

and the AGN-SF separator lines

$$y = 0.1 \quad \text{and} \quad x < -0.25 \quad (C4)$$

with $x = \log(\text{C IV}\lambda\lambda 1548,51/\text{C III}]\lambda\lambda 1907,9)$ and $y = \log(\text{C III}]\lambda\lambda 1907,9/\text{He II}\lambda 1640)$ Also, AGN and shocks show similar C IV/C III], and thus this diagnostic diagram cannot distinguish them.

¹⁸ X18 grids at 5 Myr are not shown in this paper, but are consistent with those at 10 Myr

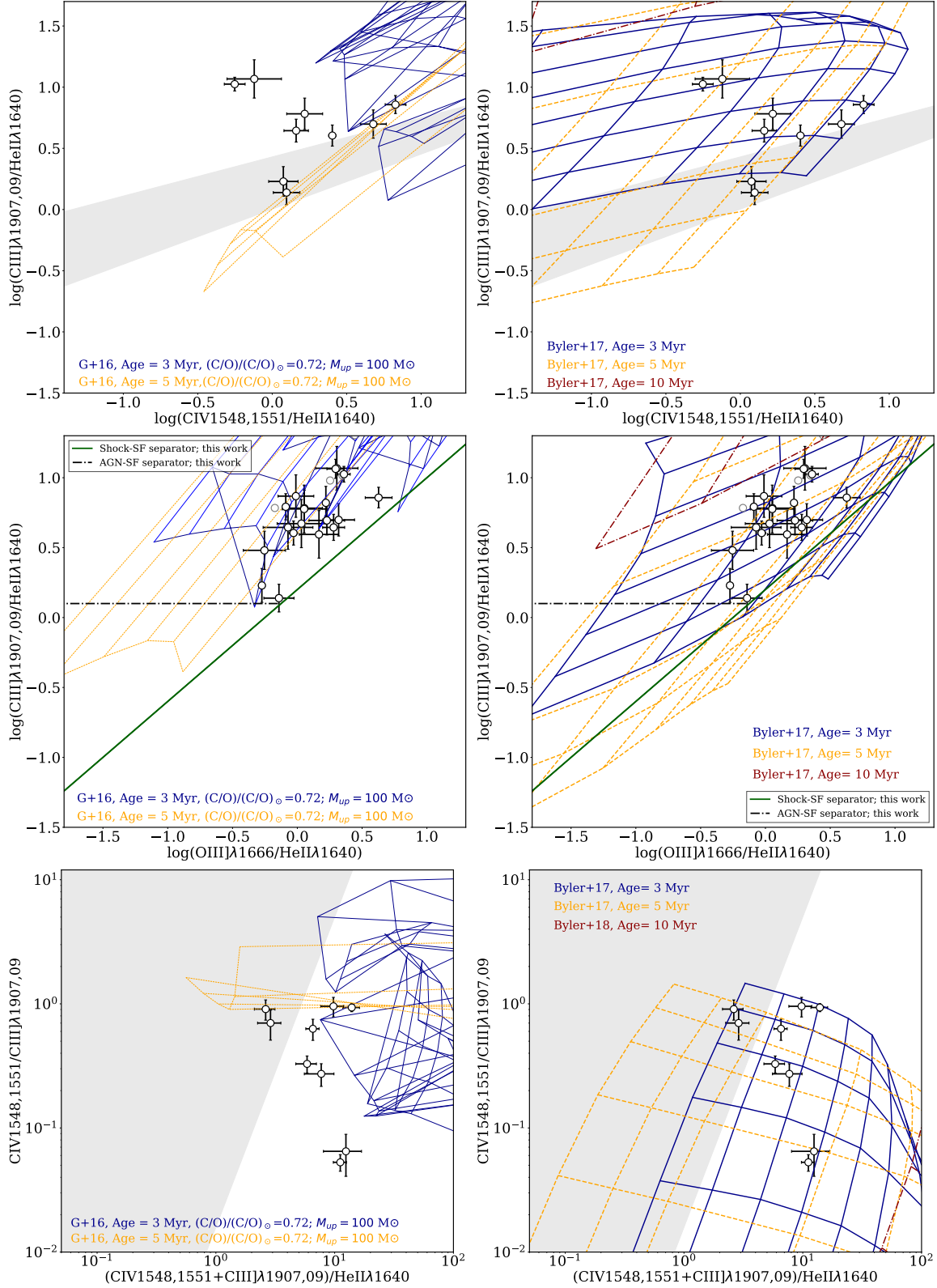


Figure 13. C3He2-C4He2, C3He2-C4C3 and C3He2-O3He2 diagrams as shown in Fig. 5, 6 and 7 with overplotted G16 single-burst SF grids (left panels) at 3 Myr and 5 Myr in blue and orange, respectively, and B17 bursty models (right panels) including stellar rotation at 3, 5 10 Myr in blue, orange and red, respectively, as indicated in the legend. Lower C/O or higher IMF cut (not shown in the plot) has the effect of moving the 3 Myr G16 grids to lower C III]/He II and (C IV+C III)]/He II line ratios, reproducing the observations, while at larger ages the stellar ionizing radiation is not enough. Indeed, stellar rotation and multiplicity (both not considered in G16) have the effect of amplifying the stellar ionizing radiation for several Myr after a star formation burst.

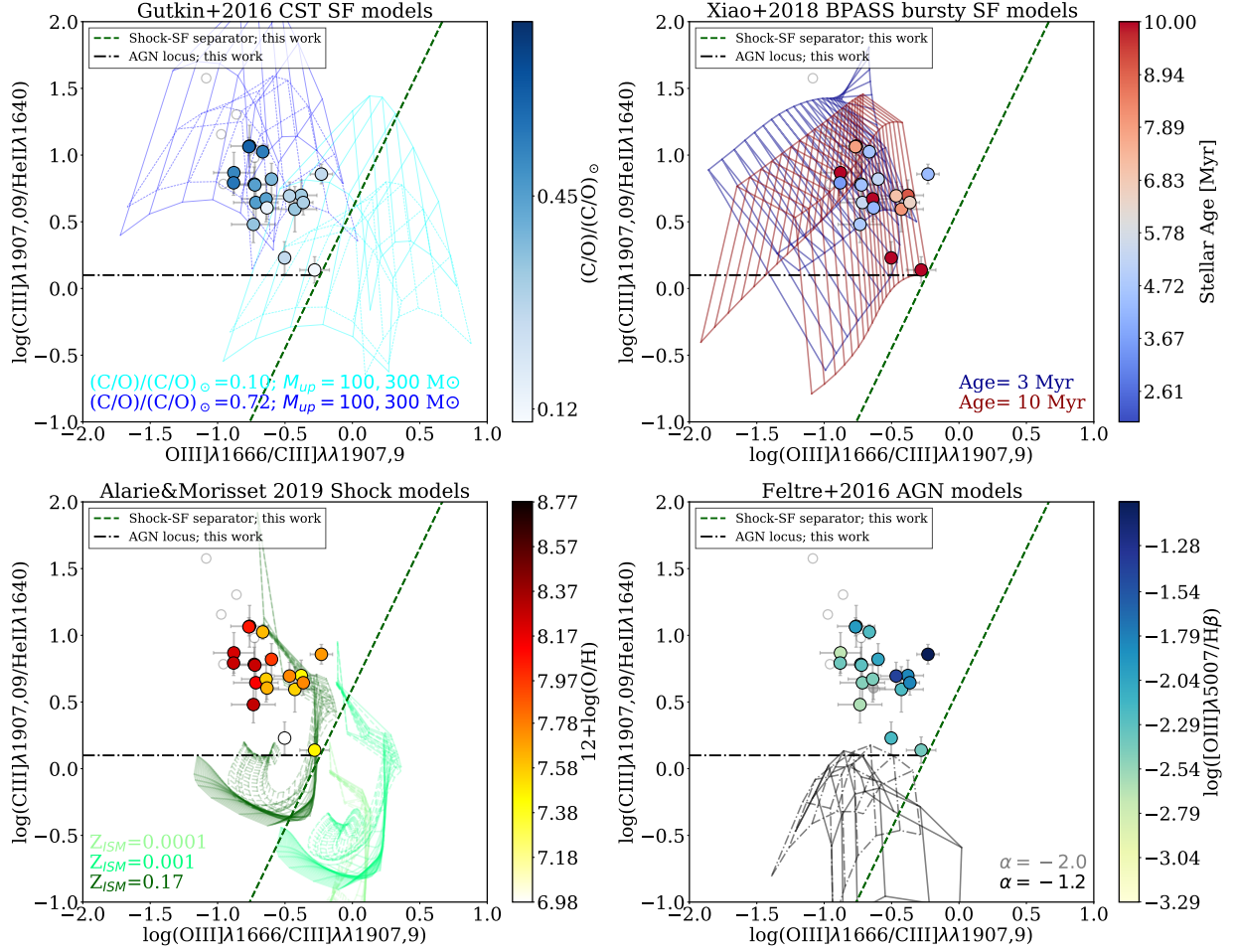


Figure 14. C3He2-O3C3 diagram: C III] $\lambda\lambda 1907,9$ /He II $\lambda 1640$ vs O III] $\lambda 1666$ /C III] diagnostic plot proposed by F16 to separate SF and AGN activities. The filled and open dots show $S/N > 3$ and $S/N < 3$ fluxes for all the emission lines taken into account, respectively. The models superimposed are as explained in Fig. 5. This diagram clearly distinguishes among SF, AGN and shocks at sub-solar metallicities (i.e., excluding the dark-green shock grid), as C3He2-O3He2 (Fig. 6), as indicated by the dashed dark green and dash-dotted black lines.

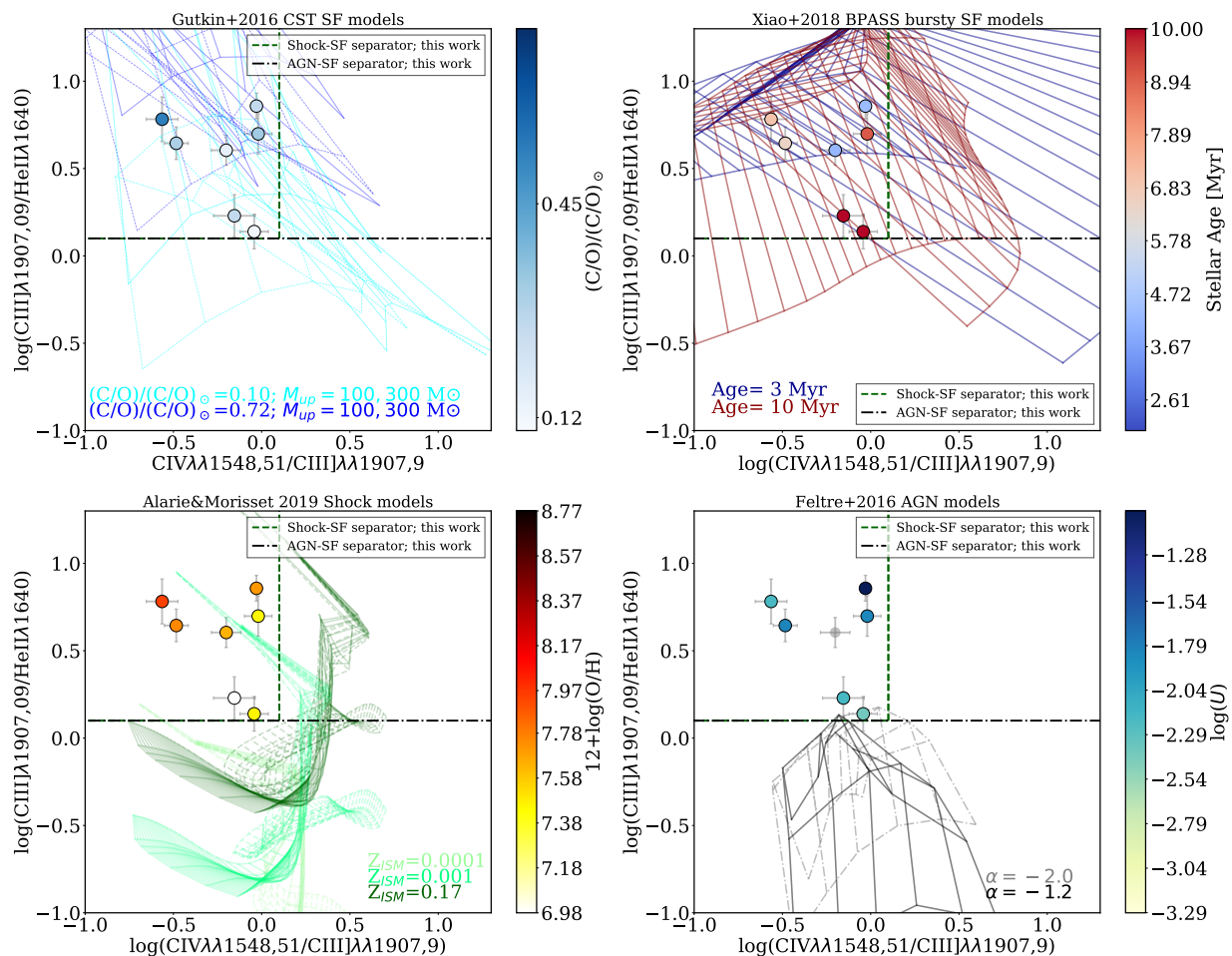


Figure 15. C3He2-C4C3 diagram: C III] $\lambda 1907,9/\text{He II } \lambda 1640$ vs C IV $\lambda 1548,51/\text{C III] } \lambda 1907,9$ diagnostic plot proposed by F16 to separate SF and AGN activities. Here we show only the CLASSY galaxies with C IV detected in pure emission. The models superimposed are as explained in Fig. 5. There is not a clear difference in C IV/C III] line ratios between the different models, and thus the difference between SF and other mechanisms is mainly traced by the different C III]/He II (higher for SF grids, lower for AGN/shocks), as indicated by the dashed dark green and dash-dotted black lines.